BIOACTIVE NANOSILICATES FOR ORTHOPEDIC TISSUE REGENERATION

A Dissertation

by

LAUREN M. CROSS

Submitted to the Office of Graduate and Professional Studies of
Texas A&M University
in partial fulfillment of the requirements for the degree of

DOCTOR OF PHILOSOPHY

Chair of Committee,	Akhilesh K. Gaharwar
Committee Members,	Elizabeth Cosgriff-Hernandez
	Daniel Alge
	Ashlee Watts
Head of Department,	Michael J. McShane

December 2018

Major Subject: Biomedical Engineering

Copyright 2018 Lauren M. Cross

ABSTRACT

Tissue engineering strategies incorporate cells and bioactive cues within a synthetic scaffold to mimic the biophysical and biochemical properties of native tissue to regenerate or repair damaged tissues and organs. A major challenge within tissue engineering is the use of supraphysiological doses of growth factors as bioactive cues to direct regeneration. The high concentrations of growth factors are often necessary for successful tissue regeneration due to short half-lives and protease degradation of growth factors; however, supraphysiological doses of growth factors have resulted in negative complications such as uncontrolled tissue growth, or cancer. To overcome this challenge, we have integrated cell biology, materials science, and bioengineering to develop a nanosilicate-based platform which can significantly reduce and potentially eliminate growth factor incorporation. Nanosilicates ($[Na^{+}_{0.7}[(Mg_{5.5}Li_{0.3})Si_8O_{20}(OH)_4]^{-0.7}$, Laponite XLG) are two-dimensional, charged particles with unique biochemical and biophysical properties. Here, we develop and utilize this platform for orthopedic tissue regeneration, establishing the unique properties of nanosilicates including their inherent bioactivity, ability to sequester and sustain release of therapeutic proteins, and incorporation into bioactive hydrogel scaffolds. Specifically, we utilize whole-transcriptome sequencing (RNA-seq) to holistically view human mesenchymal stem cell (hMSC) responses after treatment with nanosilicates to evaluate potential for stimulating both osteogenic and chondrogenic differentiation of hMSCs. We further investigated the mechanisms behind the innate bioactivity and reveal ionic dissolution products of nanosilicates (Li^{+}, Mg^{2+}, $Si(OH)_4$) stimulate osteogenesis in hMSCs. In addition to their inherent osteoinductivity, we utilize the surface charge of nanosilicate to sequester and locally delivery growth factors for prolonged duration to demonstrate enhanced osteogenic differentiation in hMSCs. Finally, as we assess the potential of nanosilicate-based scaffolds for regeneration of interface osteochondral tissues by fabricating a gradient hydrogel. We show that cell morphology can be modulated along the gradient without the use of external growth factors. From these studies, we establish that this nanosilicate-based platform holds strong potential to engineer orthopedic tissues.

ACKNOWLEDGEMENTS

I would like to thank my dissertation advisor, Dr. Akhilesh Gaharwar, and my committee members, Dr. Elizabeth Cosgriff-Hernandez, Dr. Daniel Alge, and Dr. Ashlee Watts, for their guidance and support throughout the course of this research. I would also like to thank Dr. Melissa Grunlan for standing in as a substitute for the final defense.

In addition, thank you to my lab mates/friends who have helped me over the years, I would not have made it this point without them. Thank you for listening to me, helping me, and your continued support through this process.

Finally, thanks to my parents for their encouragement and to my fiancé for his patience through this process.

CONTRIBUTORS AND FUNDING SOURCES

Contributors

This work was supervised by a dissertation committee consisting of Professor Akhilesh K. Gaharwar and Professors Elizabeth Cosgriff-Hernandez and Danial Alge of the Department of Biomedical Engineering and Professor Ashlee Watts of the Department of Veterinary Medicine.

The data analyzed for Chapter 2 was conducted in part by James K. Carrow, as we share co-first authorship in the published paper. In addition, Dr. Charlie Johnson, Director of Genomics and Bioinformatics at Texas A&M AgriLife, provided us with RNA-sequencing data and Dr. Irtisha Singh performed RNA-sequencing alignment and differential gene expression presented in Chapter 2.

All other work conducted for the dissertation was completed by the student independently.

Funding Sources

Graduate study was supported by the Doctoral Diversity Fellowship from Texas A&M University along with NIH Grant Number (DP2 EB026265, R03 EB023454) and NSF Grant Number (CBET 1705852). Its contents are solely the responsibility of the authors and do not necessarily represent the official views of the NIH or NSF.

NOMENCLATURE

hMSCs	Human Mesenchymal Stem Cells
nSi	Nanosilicates
GelMA	Gelatin Methacrylate
MκCA	Methacrylated Kappa Carrageenan
ALP	Alkaline Phosphatase
rhBMP2	Recombinant Human Bone Morphogenetic Protein 2

TABLE OF CONTENTS

Page

LIST OF FIGURES

LIST OF TABLES

1. INTRODUCTION[*]

1.1 Introduction to Nanoengineered Biomaterials for Repair or Regeneration of Orthopedic Tissue Interfaces

The musculoskeletal system, also known as the locomotive system, confers the ability to move through muscular and skeletal attachments. Major components of this system include connective tissues such as bone, tendon, ligament and cartilage. The orthopedic tissue interfaces are classified into i) bone-cartilage ii) bone-tendon and iii) bone-ligament, representing a transition from hard to soft tissues (Figure 1-1). These interfaces are responsible for the functional interactions between the adjoining tissues and reduce the formation of stress epicenters, which result in the load bearing flexibility. Most musculoskeletal injuries are associated with these interface regions and are common among individuals performing strenuous activities (athletes and military personnel) and also result due to ageing. Typical interventions to heal interfacial tissue injuries involve surgical procedures, suturing the injured tissues and stabilizing via braces, preventing further movement to avoid tearing.(1) However, open surgical interventions suffer major disadvantages such as post-suture scarring, tumor formation, and limited recovery.(2) To overcome these barriers, a range of tissue-engineered approaches have been proposed.

---

[*] Reprinted with permission from “Cross L.M.; Thakur A.; Jalili N.A.; Detamore M.; Gaharwar A.K. Nanoengineered Biomaterials for Repair and Regeneration of Orthopedic Tissue Interfaces. Acta Biomaterialia, vol. 42, pp. 2-17, September 2016.” Copyright 2016 Elsevier.

A major challenge in engineering interfaces is to control the physical characteristics of an artificial environment in terms of structure and mechanical differences: hard and soft regions. The hard regions usually represent bone tissues, primarily cortical or cancellous bone. Cortical bone is a dense and compact osseous tissue, with a modulus in the range of 16-23 GPa, and forms the outer covering of the bone.(3) Its primary function is to provide stability and protect the internal porous structures. Cancellous bone, however, is relatively soft due to a higher surface area/mass ratio and therefore less dense, with a modulus in the range of 1-2 GPa.(4) Cancellous bone is highly vascularized and metabolically active, and also harbors the bone marrow, which forms the site of hematopoiesis.(5) The soft regions of the interface are formed from connective tissues such as tendon, ligament, and cartilage. Tendons are fibrous tissues that attach skeletal muscles to bones (Bone-Tendon-Muscle-Tendon-Bone),(6) whereas ligaments link one bone to another and are crucial for joint formation.(7) Both tendon and ligament have a modulus ranging between 0.3-0.8 GPa. On the contrary, cartilage is the softest among the three, with a modulus of 0.5-2 MPa, and is primarily responsible for mitigating friction, compressive, and shear forces between bones.(8, 9)

Engineering tissue interfaces using biomaterials is a challenge due to complex architecture, cell heterogeneity, spatiotemporal distribution of extracellular proteins, and biochemical signals in the native tissue interface.(10-12) For example, tendon is a collagenous tissue connecting bone and muscles. It is made of parallel running collagen fibers and elongated tenocytes, embedded in extrafibrillar matrix.(9) Ligaments are also composed of collagenous fibers loaded with spindle shaped fibroblast cells. The ligament can be distinguished into white and yellow ligament based on the elasticity, the former being inelastic. Apart from connecting bones to bones, ligaments also serve to facilitate the joint movements, protect bone ends, and restrict incompatible movements.(13) For cartilage, the matrix is produced by chondrocytes and is not permeated with blood vessels or nerves, as the nutrient exchange occurs through simple diffusion.(14) Due to an absence of nerves and blood vessels, regeneration of damaged cartilage tissue is severely hampered in ageing and musculoskeletal disorders. In addition, dissimilar properties of bone and other soft tissues make it challenging to mimic the native interface tissue using monolithic biomaterials or conventional fabrication technologies. A range of comprehensive reviews are available that summarize various approaches to engineer interface tissues.(15-23)

Here, we focus on nanoengineered biomaterials and nanofabrication technologies used to mimic interface tissue structures and properties (Figure 1-1). Specifically, we critically evaluated various nanomaterials that have been employed to engineer bone-cartilage interfaces. We have also discussed some of the advanced micro- and nanofabrication tools currently used to engineer layered and gradient structures. Here, we capture the current state of nanomaterial research for orthopedic interface tissue engineering and identify promising new research directions in the field. Specifically, recent developments that are shaping this emerging field of interface tissue engineering are highlighted, and some of the newly developed nanomaterials that can be used in this area are discussed.

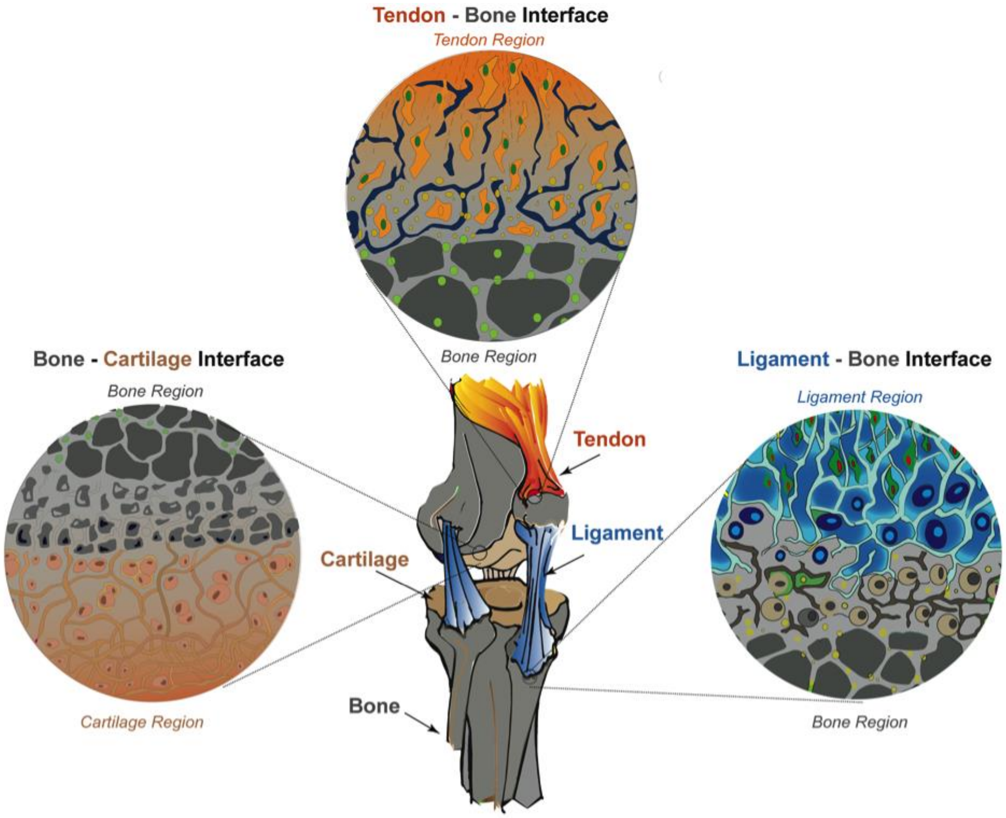

Figure 1-1. Orthopedic interface tissues include bone-cartilage, tendon-bone, and ligament-bone interfaces. In all these interfaces, a gradual transition in structure, chemical composition, and cell types between the two tissues are observed. The cartilage, tendon, and ligament are collagenous soft tissues, whereas bone consists of mineralized collagen.

1.2 Nanoengineered Biomaterials for Orthopedic Tissue Applications

Nanoengineered biomaterials and nanofabrication technologies have emerged as an alternative to conventional approaches to mimic biological tissues.(24-27) Due to enhanced control over structural, mechanical and chemical properties of nanoengineered materials, cells seeded on or within these 3D scaffold can help in mimicking some of the biological characteristics of native tissue interfaces. For example, various nanofabrication techniques such as electrospinning, and phase separation can provide control over the spatial geometry and biological complexity of the scaffold.(28-30) These nanofabricated scaffolds can control the release of therapeutics to guide cellular behavior.(31, 32) Complex geometries such as fibers, spheres, sheets, hollow tubes and nets can be fabricated to mimic some of the biological structures. In this review, we only focus on nanomaterials with one of their dimensions less than 500 nm. Specifically, we critically evaluate different types of nanomaterials currently used for orthopedic interface regeneration.

A range of ceramic and polymeric nanomaterials has been used for engineering orthopedic tissues including bone, cartilage, tendon, and ligaments.(20, 27, 29) Ceramic-based nanomaterials including hydroxyapatite, calcium phosphate, nanosilicates, and bioactive glasses have been used for hard tissues such as bone due to their high bioactive ability.(25-27) The most commonly explored nanoparticle for bone regeneration is hydroxyapatite (HAp), which has been extensively investigated for orthopedic implants.(33-36) HAp closely resembles biological apatite found in bone tissue, and therefore is a desirable biomaterial for bone regeneration. Other bioactive materials include use of calcium phosphate, bioactive glasses and silicates. Silicate nanoparticles are two-dimensional (2D) nanoparticles that have shown to induce osteogenic differentiation.(37, 38) When incorporated into hydrogels, the nanosilicates also increased mechanical properties, which would allow for the material to be applied to bone scaffolds.(39-41) Although not as extensively explored as nHAp, nanosilicates are emerging as a promising material for bone regeneration. These ceramic nanoparticles are complex mineral structure that have shown to bind to surrounding bone and stimulate bone formation. More recently, a range of carbon-based nanomaterials such as carbon nanotubes (CNTs), graphene (G), and nanodiamonds (NDs) have also been explored for bone tissue engineering.(42) Graphene has induced osteogenic differentiation in stem cells,(43) and its derivative graphene oxide has also exhibited a similar ability.(44)

For soft orthopedic tissues such as cartilage, tendons, and ligaments, only a few types of nanomaterials have been investigated. For cartilage tissue, titanium dioxide (TiO_2) nanosheets were explored.(45) These nanosheets were incorporated into an acrylamide hydrogel and the resulting nanocomposite mimicked chemical and physical properties of native articular cartilage. For tendon and ligament tissues, nanofibers are most often used because of the fibrous structure of native tissues. Nanofibers have been fabricated from various polymeric biomaterials including poly (lactic-co-glycolic acid) (PLGA), poly (L-lactic acid) (PLLA), poly (caprolactone) (PCL), and collagen.(46-50)

Specifically, for interface tissue engineering, many of the aforementioned nanomaterials have not been investigated and only a few of the conventional nanomaterials are engineered for interface tissue engineering. For example, a range of nanofabrication techniques are used to obtain nanoengineered scaffolds from synthetic and natural polymers including PLGA, PLLA, PCL, collagen, hyaluronic acid, silk, alginate and fibrin. These biomaterials are usually modified for use; in some cases blended with other polymers and nanoparticles (hydroxyapatites, calcium phosphate etc.) to enhance the mechanical properties and bioactive characteristics.(25-27) Specifically, nanoscale topographies obtained by incorporating nanoparticles in the polymeric structure have shown to direct cell fate.(51) In the past couple of decades, the application of nanocomposite materials has progressively surfaced since they can stimulate morphological changes, gene expression, proliferation and differentiation, and mimic the native tissue composition.(52)

1.3 Nanoscale Technologies to Engineer Layered and Gradient Structures

Several fabrication strategies are currently used to engineer orthopedic interface tissues (Figure 1-2). The most basic approach involves monolithic scaffolds loaded with growth factors and/or cells.(53) This strategy was commonly used when modeling one tissue type such as bone or cartilage; however when it comes to interface tissues, this strategy cannot represent multiple tissue types. Recently, bi-layered scaffolds have been investigated, where each layer of the scaffold represents a different tissue.(54-56) Although a better representation of the complex interface tissue, this strategy does not account for the interface region.(19)

More recently, multi-layered scaffolds consisting of three or more layers have been designed. In this strategy, the middle layer(s) represents the interface region and the outer layers mimic the soft or hard tissue.(57-59) With these layered designs, multiple materials and cell types can be incorporated to mimic the complex architectures of the interface tissues; however, there is not necessarily a smooth transition between the two represented tissues as there is the body. One of the emerging strategies to mimic interface tissues involves developing a gradient scaffold.(19, 21, 22) In this approach, a gradual change in the material or the chemical composition is engineered to better recapitulate the native tissue transition. The gradual change can lead to differential expression of cultured cells and give rise to a multifarious environment. Many of the reviewed techniques utilized this gradient approach, and the formation of the chemical or material gradient can be formed through several methods including capillary action, microfluidics, tilt angle, and centrifugation.(22, 23) Here, we highlight the gradient and layered nanofabrication techniques that have been employed for orthopedic interface tissues.

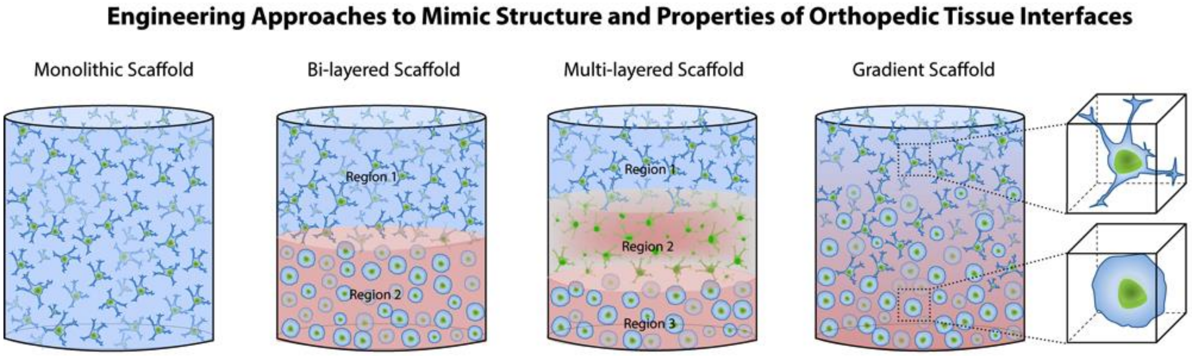

Figure 1-2. Engineering approaches for interface tissue engineering. Several strategies including use of monolithic, layered and gradient scaffolds are investigated to mimic the native tissue interfaces. Monolithic scaffolds comprise of one type of biomaterial loaded with cells, whereas layered scaffolds comprise different layers, each representing a single tissue type. Multi-layered scaffolds employ the middle layer, which represents the interface region. The gradient scaffold accounts for the interface region and the smooth transition between two regions.

1.4 Bone-Cartilage Interface

The aim of interface tissue engineering is to regenerate, augment or repair the damaged interface between the bone and its surrounding tissue. Cartilage injuries are often difficult to treat because damage can occur in both the articular cartilage and the underlying subchondral bone or more specifically the osteochondral interface. Some of the clinically relevant techniques for cartilage regeneration involve osteochondral approaches and include chondrocyte and osteochondral transplantation, as well as debridement of damaged tissues (through arthroscopy). Often, surgical procedures require the removal of the injured bone-cartilage region through the creation of an osteochondral defect. Another common surgical procedure for these injures involves microfracture, in which a defect is created by removing calcified cartilage and puncturing the underlying subchondral bone. Small holes are created for bone marrow components including stem cells to fill the defects. Although this procedure often results in less durable and unorganized tissue, it is one of the most common techniques to treat cartilage injuries.(60) Unfortunately, most of these clinical approaches are non-ideal and result in undesired complications to the patient.(12, 61) Therefore, recent advancements are focused on minimally invasive approaches to facilitate cartilage regeneration using various polymeric scaffolds such as Hyalograft© (1999),(62) Bioseed© (2001),(63) CaReS® (2006),(64) Atelocollagen gel (2007),(65) Cartipatch® (2008),(66) Neocart® (2009),(67) Chondron™ (2010),(68) and Novocart® (2012)(69) to facilitate cartilage regeneration. Additionally, Tutobone®, a bovine-origin bone substitute, and Chondro-Gide® have claimed to aid in osteogenic repair.(70) However, Tutobone® causes xenogenic reactions, and due to limited clinical data, this product is not a preferred choice by the clinicians.(71)

Most of these approaches involve use of a monolithic structure that fails to mimic the anatomical structure or properties. To address this need, various approaches such as multiphasic scaffolds and gradient structures have been investigated to mimic the native architecture.(72, 73) For example, bilayered scaffolds have been sought as a key design for regeneration of osteochondral tissues. Some of the commonly employed bilayered structures can be categorized as “independently assembled structures” and “integrated bilayered structures”. In independently assembled structures, two discrete scaffolds of bone and cartilage are made individually and then connected before or during implantation.(74) On the contrary, integrated bilayered structures are synthesized as a composite of two different materials.(54)

Although the aforementioned strategies are promising, they lack the micro- and nanostructural resemblance to native interface tissues and selection of biomaterials play an active role in determining the healing outcome.(75) To overcome these problems a range of nanomaterials have been investigated to mimic the structure and mechanical properties of osteochondral interfaces (Table 1). Some of the common nanomaterials that have been exploited for osteochondral interface engineering are nanocomposites composed of PCL, poly (L-glycolic acid) (PGA), or PLGA with hydroxyapatite or calcium phosphate nanoparticles. In addition, some natural materials have also been investigated to mimic the structure of native interface tissue including agarose and collagen.(76, 77) In one study, a binary process of extrusion and electrospinning was used to fabricate a graded, non-woven network of PCL and tricalcium phosphate nanoparticles (β-TCP).(46) β-TCP nanoparticles were injected at varying flow rates, which allowed the formation of a continuous, linear concentration gradient throughout the electrospun PCL matrix. Mouse preosteoblasts were seeded on these scaffolds, and it was observed that the initial rate of cell proliferation decreased in comparison to cells seeded on control tissue culture polystyrene.(46) This decrease was supported by previously documented results suggesting that the decrease in the proliferation was attributed to the onset of differentiation.(78) Four weeks post seeding, a considerable amount of calcium deposit, collagen fiber production, and multilayered cells were observed.(46) Here, the addition of β-TCP nanoparticles aided in directing preosteoblast differentiation.

Table 1-1. Nanoengineered biomaterials for bone-cartilage tissue engineering.

Interface Region	**Material for Bone**	**Material for Cartilage**	**Significance**	**Limitations**
Bone-Cartilage	Randomly oriented PCL nanofibers and β-TCP nanoparticles	PCL nanofibers	Graded scaffold mimicking structural and compositional properties of natural interface (46)	Only bone specific markers were explored, the cartilage region of the scaffold was not investigated (46)
	Collagen with nHAp	Collagen with nHAp	Compositional and structural gradient created by controlling porosity and calcium phosphate ion concentration (34)	Cellular response to graded scaffold was not explored (34)
	Polyamide 6 and nHAp	Poly vinyl alcohol	Bilayered scaffold supported bone and cartilage regeneration *in vitro* and *in vivo,* as well as exhibited sufficient mechanical stability (55)	Each layer was fabricated separately and bone marrow stem cells were differentiated on either region prior to implantation (55)
	PLGA and nHAp	PLGA and nHAp	nHAp enhanced hMSC proliferation and mechanical properties (33)	Scaffolds were investigated individually for bone and cartilage regeneration, not as assembled unit (33)
	Alginate or Agarose with nHAp	Alginate or Agarose	Incorporation of deep zone chondrocytes and nHAp enhanced collagen production and scaffold mechanical strength (79)	Alginate gels did not allow for uniform distribution of nHAp (79) HA particle size did not significantly affect deep zone chondrocyte response (79)
	Agar	PEGDA and nHAp	Injectable and photopolymerizable composite enhancing cartilage anchorage to bone ECM (80)	Limited characterization of the bone region (80)
	Silk Fibroin and nCaP or nHAp	Silk Fibroin	Bilayered scaffolds exhibited increased stability and promoted bone growth and formation of blood vessels (56, 81, 82) Trilayered scaffolds demonstrated potential for promoting cell differentiation (83)	Long-term *in vivo* stability remains to be evaluated (56, 83)
	Chitosan and nHAp	Chitosan and Silk Fibroin	Four layered, gradient scaffold exhibited range of mechanical properties and initial biocompatibility (84)	Long-term biocompatibility and matrix production remain to be assessed (84)

In addition to β-TCP, hydroxyapatite nanoparticles (nHAp) have also been a popular choice for osteogenic and osteochondral repair strategies. In another study, collagen scaffolds consisting of nHAp crystals were fabricated *via* a chemical reaction gradient of disodium hydrogen phosphate and calcium chloride.(34) This study, however, did not feature any *in vitro* validation of cellular response to this graded scaffold. Alginate and agarose gels combined with nHAp were also investigated for osteochondral interface regeneration.(79) The alginate scaffolds did not allow for a uniform distribution of hydroxyapatite; whereas, the agarose gels allowed for uniform distribution of micro- and nano-sized hydroxyapatite (Figure 1-3a). Both the micro- and nano-sized hydroxyapatite loaded scaffolds were investigated with interface relevant cells such as deep zone chondrocytes (DZC) and hypertrophic chondrocytes induced by thyroid hormone (DZC +T3). When the agarose/nHAp composite was seeded with the DZC+T3 cells, there was a significant increase in alkaline phosphatase (ALP) activity after 14 days in comparison with the control agarose scaffold. Also, on day 14, the addition of nHAp significantly augmented collagen X production and Indian Hedgehog (Ihh) expression (Figure 1-3b). The addition of nHAp to the agarose gels, resulted in increased compressive modulus (Figure 1-3c). Additionally, there was a positive correlation between collagen content and the compressive modulus in the nHAp scaffold compared to the microHAp and control scaffolds (Figure 1-3c). However, no significant effect of the particle size was observed on the DZC response.(79) In the future, both particle sizes could be incorporated into the scaffold since both micro aggregates and nano crystals are found in the native interface tissue.(85)

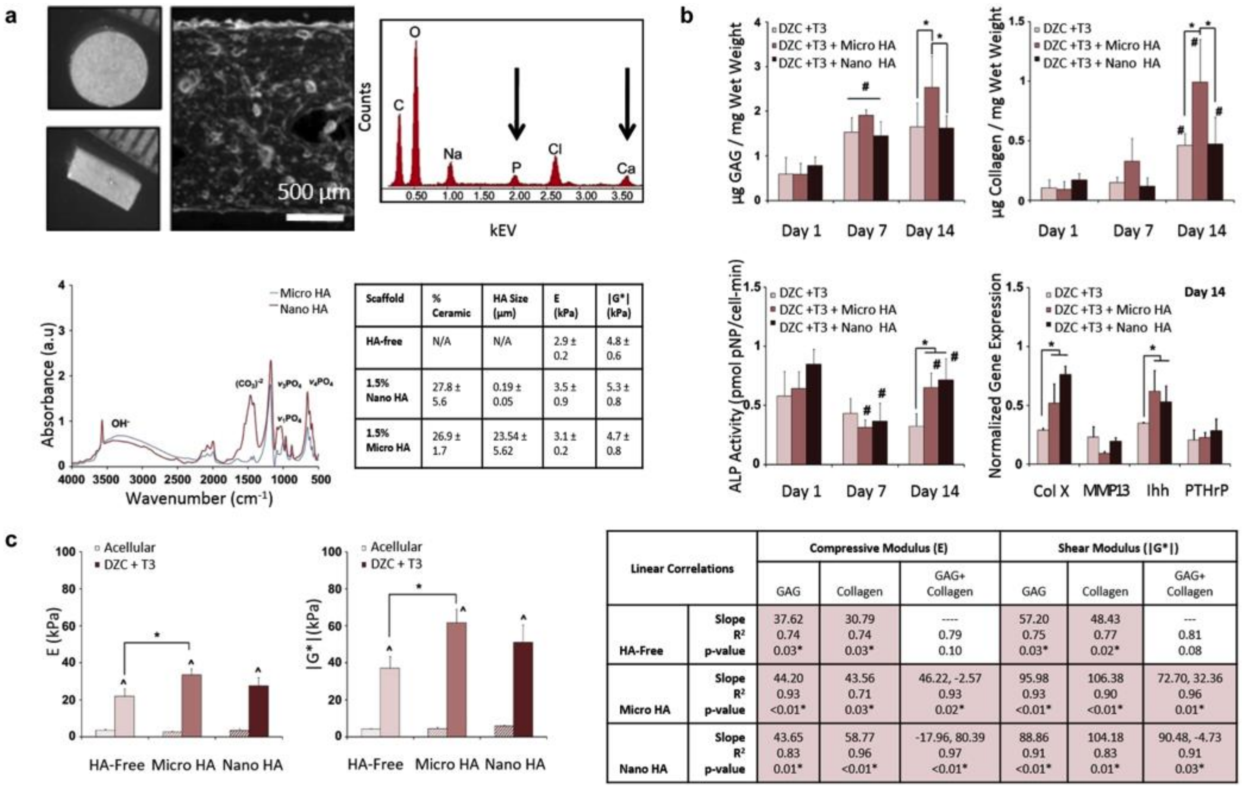

Scaffold	% Ceramic	HA Size (μm)	E (kPa)	|G*| (kPa)
HA-free	N/A	N/A	2.9 ± 0.2	4.8 ± 0.6
1.5% Nano HA	27.8 ± 5.6	0.19 ± 0.05	3.5 ± 0.9	5.3 ± 0.8
1.5% Micro HA	26.9 ± 1.7	23.54 ± 5.62	3.1 ± 0.2	4.7 ± 0.8

Linear Correlations		Compressive Modulus (E)			Shear Modulus (|G*|)		
		GAG	Collagen	GAG+ Collagen	GAG	Collagen	GAG+ Collagen
HA-Free	Slope R² p-value	37.62 0.74 0.03*	30.79 0.74 0.03*	---- 0.79 0.10	57.20 0.75 0.03*	48.43 0.77 0.02*	--- 0.81 0.08
Micro HA	Slope R² p-value	44.20 0.93 <0.01*	43.56 0.71 0.03*	46.22, -2.57 0.93 0.02*	95.98 0.93 <0.01*	106.38 0.90 <0.01*	72.70, 32.36 0.96 0.01*
Nano HA	Slope R² p-value	43.65 0.83 0.01*	58.77 0.96 <0.01*	-17.96, 80.39 0.97 <0.01*	88.86 0.91 <0.01*	104.18 0.83 0.01*	90.48, -4.73 0.91 0.03*

Figure 1-3. Nanocomposite scaffolds for osteochondral regeneration. (a) SEM show uniform distribution of nHAp in agarose gel and presence of calcium (Ca) and phosphorous (P) is confirmed by EDS and FTIR analysis. No significant effect of nHAp on elastic modulus and shear modulus is observed. (b) The effect of micro and nano HA particles on GAG and collagen show a significant increase on day 14. Also, the addition of particles leads to a significant increase in ALP activity, production of type X collagen and Ihh expression on day 14. (c) The cell-loaded scaffolds have significantly higher mechanical stiffness compared to the acellular scaffolds. Linear correlation analysis shows a positive relationship between GAG content and compressive modulus and shear modulus for all scaffolds. Finally, to determine synergistic affects, a significant correlation of GAG + collagen with the nano and micro HA groups is observed. Reproduced with permission.(79) Copyright © 2012, Elsevier B.V. and Copyright © 2012, Mary Ann Liebert, Inc.

In another study, an unconventional approach was taken by combining nHAp and polyamide 6 (nHAp/PA6) with polyvinyl alcohol/gelatin scaffolds to yield a biphasic scaffold.(55) The polyamide amalgamation aided in an increased stiffness and mimicked mineral structures of native bone tissue, thereby integrating with the osteochondral structure following implantation. A common issue associated with most of the autologous implantation protocols is the chondrocyte extraction from the donor, which can lead to donor-site morbidity and cellular dedifferentiation and accrued damage. The group instead acquired bone marrow stem cells, differentiated them *in vitro* into chondrogenic/osteogenic lineage, and seeded them onto the scaffolds. *In vivo* implantation of these biphasic scaffolds yielded regeneration of the osteochondral region. In addition, the mechanical and structural properties of the scaffold resembled native cartilage and subchondral regions, further warranting its use as an implant material.(55)

Recently, an osteochondral scaffold using agar and poly (ethylene glycol) diacrylate (PEGDA) reinforced with nHAp was fabricated.(80) For the bone region, 2% agar loaded with osteoblasts was selected and the cartilaginous phase was fabricated from 15% PEGDA and 0.5% nHAp (pretreated with growth factors) loaded with mesenchymal stem cells. Finally, a thin stainless-steel pin was inserted through the center of scaffold in order to assemble the regions as an osteochondral plug. In this study, nHAp was selected to allow for integration between the engineered bone and cartilage regions. Also, nHAp aided in stem cell chondrogenic differentiation within the cartilaginous region. When tested *in vivo*, the scaffold integrated well with the host bone tissue and demonstrated superior strength, attributed to the addition of hydroxyapatite.(80) In a similar approach, nHAp was incorporated in PLGA scaffolds using thermal phase separation.(33) The introduction of nHAp to the PLGA scaffold increased the compressive modulus from 400 kPa to 600 kPa. The efficacy of the nanocomposites was evaluated *in vivo* using rat models with osteochondral defects, by delivering mesenchymal stem cells within the scaffold. After four weeks of implantation, the rats showed recovery as highlighted by increased mineralized content, collagen production, and hyaline cartilage formation. The study, however, investigated these scaffolds as individual units for bone-cartilage engineering and not as assembled unit. Further studies on assembled PLGA and PLGA-nHAp should be conducted in order to substantiate these findings.(33)

Silk fibroin has also been investigated for various tissue engineering approaches.(56, 81-84, 86, 87) Specifically for cartilage repair, silk fibroin has been explored because it is a natural material which has shown to support cell adhesion as well as only stimulate a low inflammatory response.(88, 89) In several studies, silk fibroin and silk-nano calcium phosphate (silk-nCaP) were utilized for osteochondral treatment.(56, 81, 82) On study fabricated a bilayered scaffold in which a porous silk-nCaP layer was prepared by salt leaching using sodium chloride, and was then layered with a porous silk fibroin scaffold (Figure 1-4a,b).(56) SEM and micro-CT were performed to characterize the scaffold and confirm the distribution of CaP in the silk matrix (Figure 1-4b-d). Although this was a bilayered design, an interface region joined the two distinct layers. The osteochondral regeneration potential of the material was evaluated in a rabbit osteochondral defect model. The subcutaneous implantation of the scaffold resulted in formation of blood vessels and within four-weeks post-implantation, connective tissue was found to adhere to the scaffold surface, which support the *in vivo* biocompatibility of the scaffold. Formation of the interfacial region was observed: the silk-nCaP layer induced bone formation and silk promoted type II collagen and glycosaminoglycan production (Figure 1-4e). Moreover, the stability of the scaffold addressed the problems of long-term *in vivo* efficacy.(56) In another study, silk fibroin was incorporated into a trilayered scaffold for osteochondral tissue regeneration.(83) This 3D scaffold was fabricated via a paraffin microsphere leaching process which allowed for control of the pore size and interconnectivity. The bone and intermediate layer consisted of silk fibroin and nHAp while the top cartilage layer consisted of just silk fibroin that was oriented longitudinally. Adipose-derived stem cells (ADSCs) were seeded onto the bone and cartilage layers of the scaffold and cultured separately in osteoinductive or chondroinductive media. In these *in vitro* microenvironments, ADSCs produced bone and cartilage extracellular matrix proteins in the prospective regions. The intermediate region remained cell-free and prevented the ADSCs within the bone and cartilage regions from mixing with one another. Further studies, specifically *in vivo* models, need to be investigated to observe cellular differentiation capabilities within the scaffold; however, this technique provided a promising trilayered scaffold for osteochondral tissue engineering.(83) Silk fibroin has also been paired with chitosan and nHAp and in one study, the materials were combined to form a four layered porous scaffold in which the top three layers contained a gradient in chitosan and silk fibroin and the bottom layer contained chitosan and nHAp.(84) In addition, the scaffold contained a gradient in porosity and pore size to represent the natural gradient from calcified layer to superficial layer in native articular cartilage. Mechanical properties of the scaffold were assessed and an increasing trend in compressive modulus and strength were observed from the first layer containing 25wt% chitosan and 75wt% silk fibroin to the bottom layer containing 50wt% chitosan and 50wt% nHAp. Finally chondrocytes were seeded on the scaffold to assess biocompatibility, and at 14 days cells were viable in all four regions of the scaffold.(84) Although the short-term studies proved initial cell adherence and viability, further studies such as investigating extracellular matrix production long-term are necessary to evaluate scaffold integration and efficacy.

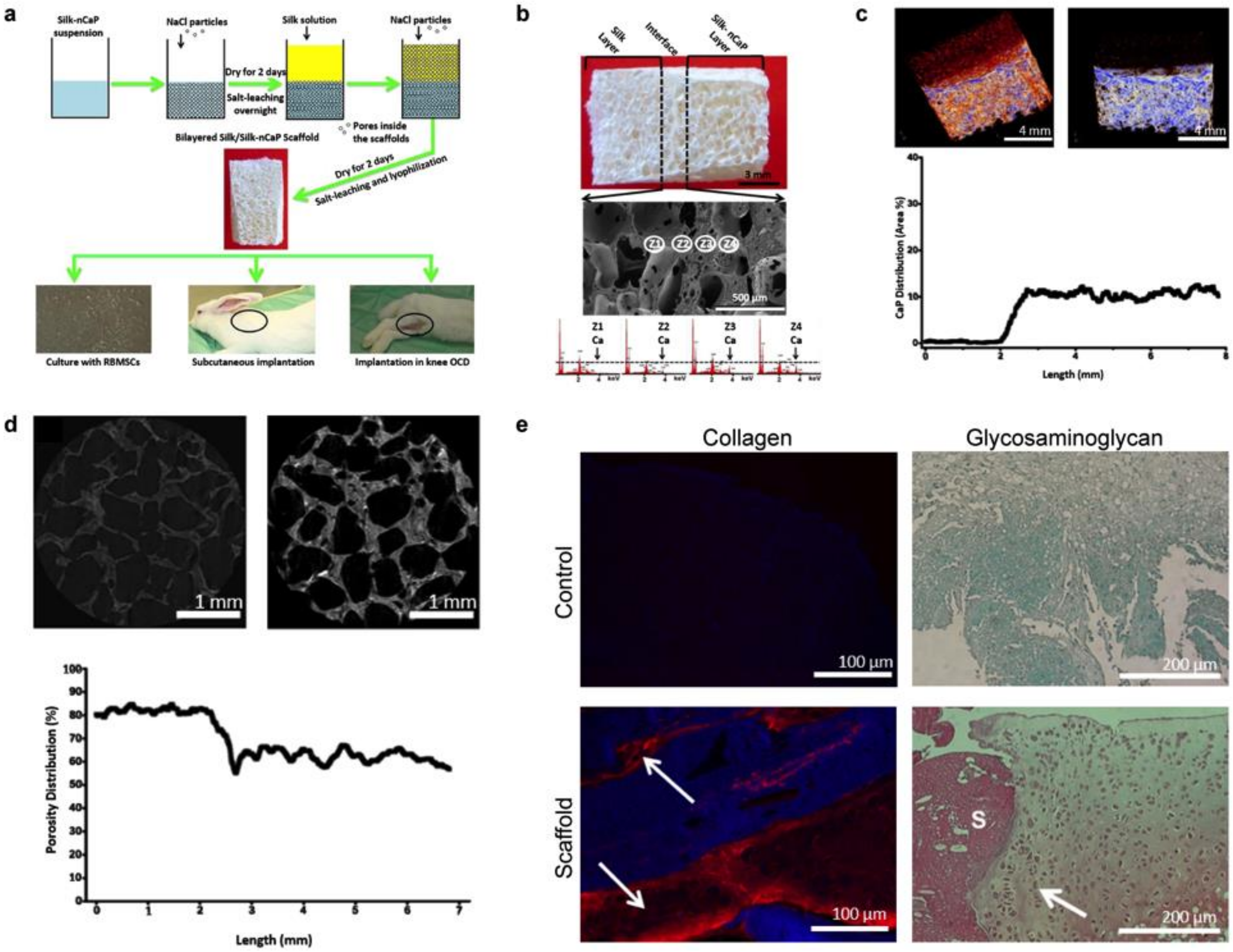

Figure 1-4 Bilayered nanocomposite scaffolds for osteochondral regeneration. (a) Synthesis of bilayered silk/silk-nCaP scaffold (top) and subsequent implantation in rabbit model (bottom). (b) SEM and EDS analysis of the layered scaffold investigates presence of calcium in different zones (Z1-4). (c) CaP distribution investigated using micro-CT, showing two distinct layers - silk layer (brown) and composite layer (blue). (d) Quantitative analysis of porosity distribution shows homogeneous and interconnected porous network in each layer. (e) *In vivo* studies reveal type II collagen (red) production in the silk layer of the scaffold (bottom left), while the control defect does not exhibit any production (top left). Using Safranin O, glycosaminoglycan (GAG) formation is present at the edge of the top silk layer (bottom right) but is not present in the control defect (top right); the S refers the scaffold and the arrow points to newly formed tissue. Reproduced with permission.(56) Copyright © 2012, Elsevier B.V.

Although the aforementioned scaffolds have shown potential for bone-cartilage regeneration, most of them involve addition of cells, which could lead to complications in clinical setting. More recently, cell-free scaffolds have gained popularity. These scaffolds stimulate the host environment to differentiate and produce all the necessary components required for regeneration, by the virtue of mechanical and chemical properties of the scaffold.(90) MaioRegen^{TM} (Fin-Ceramica S.p.A., Faenza, Italy**)**, a cell-free 3D biomimetic graded scaffold for osteochondral tissue engineering, has been investigated in clinical studies.(83, 90, 91) The tri-layered scaffold fundamentally mimics the cartilage, interface, and subchondral surface of the bone-cartilage region.(92) It is composed of equine-origin type I collagen for the cartilage stimulation, magnesium-enriched nHAp and collagen for the intermediate region, and magnesium supplemented with nHAp for the subchondral bone regeneration. These layers of the scaffold are deantigenated, preventing any immunogenic responses upon engrafting. Furthermore, the scaffold is designed to promote chemotaxis and remodeling and the controlled porosity allows for nutrient exchange.(92) These scaffolds are usually employed for larger osteochondral defects. Also, the simplicity of the one-step surgical procedure involved has been reported to generate favorable outcomes involving minimal follow up and complications.(93) However, a recent study reported inconsequential osteochondral recovery using this biomimetic scaffold.(90) Additionally, a major ambiguity in these studies is the absence of gold standards, therefore, no comparisons are made through controls. More recently, another approach for cartilage regeneration was explored using a decellularized cartilage-based scaffold.(94) Preliminary results with bone marrow derived mesenchymal stem cells indicated increased expression of osteogenic and chondrogenic markers without any external growth factors. In the future, this scaffold could be used in an osteochondral defect *in vivo* and in the complex environment regional differentiation may be possible.(94) Although the presented nanomaterial approaches for treating bone-cartilage injuries are promising, further studies must be done to evaluate these scaffolds as true candidates to replace the clinical standard treatments. In addition, many of the approaches only incorporate nanomaterials into the bone region of the scaffold to improve the mechanical properties of the material while only a few explored the bioactivity of nanomaterials. Future studies could study the effect of incorporating nanomaterials into both regions of the scaffold for both structural stability and bioactivity.

1.5 Emerging Trends and Techniques

A recent surge in the development of new bioactive nanomaterials and our understanding of the complex relationships between nanomaterial structure and properties have resulted in the expansion of smart and functional biomaterials.(29) The uses of nanomaterials for biomedical applications are rapidly expanding and promising new improvements in the area of tissue engineering have been demonstrated.(25-27) For example, a range of new bioactive nanomaterials such as 2D nanomaterials, metal oxides, and ceramic nanoparticles have been developed to control and trigger stem cell differentiation into different lineages (Figure 1-5a**)**. Some of the new categories of nanomaterials that have shown promise in the area of orthopedic tissue engineering include use of graphene oxides,(43, 44) synthetic silicates,(37, 41) and titanium dioxide (TiO_2).(45) Due to the exponential growth in nanomaterial development in recent years, it is expected to provide a wider selection of nanomaterials with custom physical, chemical, and biological characteristics that can be tailored for various biomedical and biotechnological applications. Most of these new nanomaterials have not been investigated yet for interface tissue engineering and there is tremendous potential to design and develop smart nanomaterials for engineering orthopedic tissue interfaces.

A potential avenue for evaluating various nanomaterials for interface tissue engineering is use of high-throughput screening (Figure 1-5b**)**. 3D biomaterial microarrays hold enormous promise for regenerative medicine because of their ability to quickly optimize the right combination of biomaterials, cells, and the ECM environment for certain applications.(95, 96) The use of 3D microarrays can, if optimized correctly, result in more than 1000-fold reduction in biomaterials and cells consumption when engineering optimal nanomaterials combinations, which makes these miniaturized systems very attractive for interface tissue engineering.

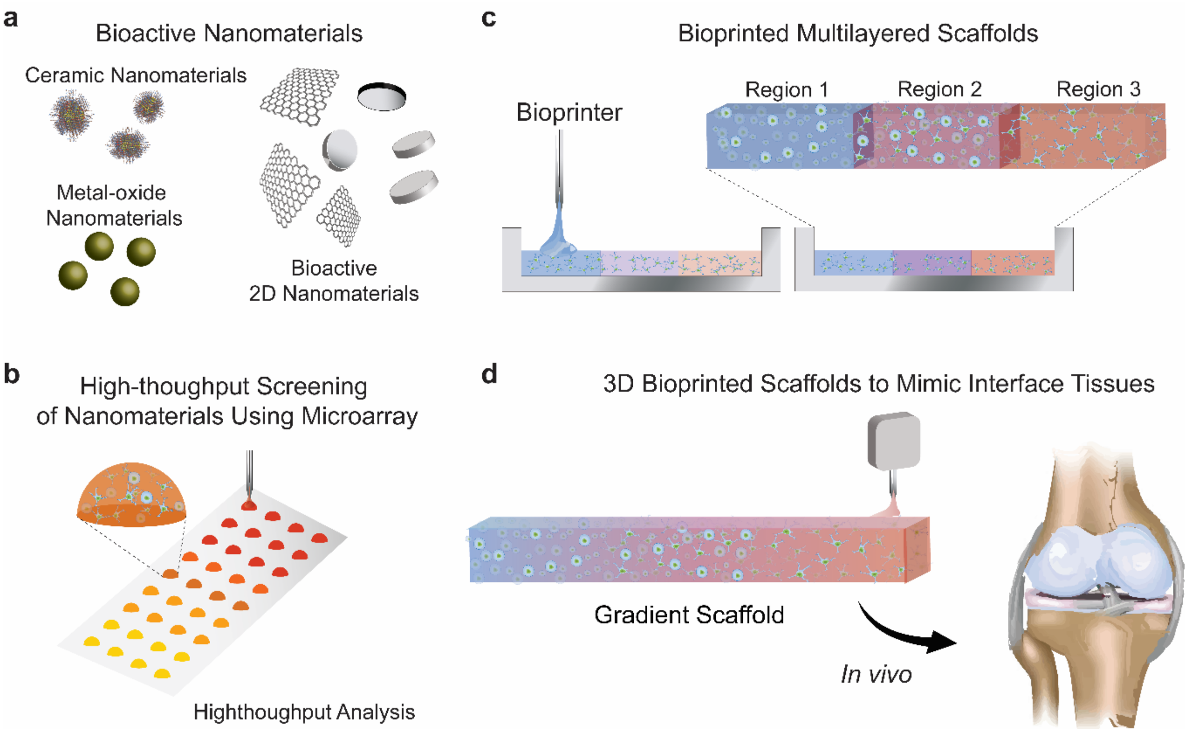

Figure 1-5. Emerging trends in interface tissue engineering. (a) Bioactive nanomaterials such as ceramic, metal oxides and 2D nanomaterials have potential to control and trigger cellular process. (b) Microarray printing technology can be used to screen nanomaterials library in a high-throughput manner. (c) Bioprinting techniques can be used to engineering layered scaffold for orthopedic tissue interfaces. (d) The use of a 3D bioprinter can mimic native tissue architecture with high spatiotemporal control of cells and physical/chemical clues.

In addition, recent efforts on designing functional biomaterials also focus on developing multicomponent system consisting of two or more nanomaterials.(26, 27) These multicomponent systems have the ability to exhibit distinct characteristics. For example, magnesium oxide (MgO) nanoparticles coupled with nHAp and PLLA, have shown to increase osteoblast adhesion and proliferation and also provide antimicrobial properties.(97, 98) Although these multicomponent nanomaterials have shown increased osteoblast proliferation and promise for bone tissue applications, future studies need to be conducted in order for these materials to be applied to interface tissue engineering. Additionally, most of these new developed strategies are evaluated for bone-related applications and very limited studies focus on evaluating these new nanomaterials for other orthopedic tissues including cartilage, tendon, and ligament.(99-101) Thus there is a need to investigate these next generation of biomaterials for interface tissue engineering.

Another emerging approach in tissue engineering is additive manufacturing.(102-106) Conventional techniques used to fabricate scaffolds for interface tissues include salt leaching, electrospinning, phase separation (thermally induced), freeze drying, gas foaming, emulsification, and solvent casting and particulate leaching (SCPL). Many of these techniques use salts, porogens, and organic solvents, which result in limited cellular infiltration and encapsulation. To overcome these limitations, recent approaches have shifted towards additive manufacturing. Some of the additive manufacturing approaches that can be used to engineer interface tissues include 3D printing,(107-109) stereolithography, air pressure aided deposition,(110, 111) and robotic dispensing(112-114). These free-form prototyping techniques face problems of bio-printability, which limit the use of printing cells with the scaffolds.

Recently developed bioprinting techniques can be used to engineer orthopedic tissue interfaces (Figure 1-5c**)**. So far, bioprinting has only been used to print one or two types of tissue; however with the emergence of new and improved bioinks, there is a possibility to print layered and/or gradient tissues.(115) 3D microarray systems can be used to generate layered/gradient-like tissue interfaces and such multilayered microgel arrays can be used for high-throughput screening.(95) We believe that the development of new high-throughput technologies for studying stem cell behavior within multilayered materials would significantly advance the field of interface tissue engineering.

Recently, 3D bioprinting can be used to print three different cell types using layer-by-layer deposition of custom bioinks (Figure 1-5d). For example, an alginate-collagen bioink revealed that cells could be localized in predetermined positions without compromising cell viability.(116) Although the cells were not printed with a bioink, this study proves the viability of printing cells to control cell placement in a 3D tissue construct. Another aspect of 3D printing that makes it appealing for engineering interface tissues is that its resolution would allow for gradients to be fabricated not only in the x- and y- directions, but also in the z- direction.(117, 118) In addition, a dual nozzle syringe on the printer would make it possible to print multiple biomaterials at the same time. Previously, gradients have been fabricated using a gradient maker and mixing chamber in which the volume of different materials are controlled and added at different rates to create zones.(119) A 3D bioprinter can mimic native tissue architecture with high spatiotemporal control. Overall, 3D bioprinting will provide an improved strategy for engineering interface tissues and advance the field of tissue engineering.

1.6 Conclusion and Future Directions

Interface tissue engineering has seen remarkable progress in the past decade with continued improvements from autologous transplantation to rapid prototyping of different biomaterials.

Nanomaterials such as nanofibrous and nanocomposite scaffolds loaded with hydroxyapatite, calcium phosphate, or aragonite are attractive scaffolding materials, since they can control and direct cell fate and tune the formation of ECM. Additionally, nanomaterials can be customized to control the degradation profile to facilitate tissue regeneration. These nanoengineered scaffolds and nanofabrication techniques have the potential to minimize surgical interventions and overcome the complexities associated with donor site morbidity. Additionally, nanomaterials can be tuned to contain binding sites, growth factors, and signaling proteins, which are important for chemical transductions. As new bioactive materials and fabrication technologies are developing, it is possible to mimic some of the physical, and chemical properties of native tissues interfaces. Specifically, the emergence of bioactive nanomaterials offers promise for directing cell behavior. Although, these nanofabricated constructs mimic the interfacial regions efficiently, their clinical translation has not been achieved due to lack of strong clinical data. In addition, in order to create less invasive surgical procedures to treat injuries at interface tissues, these nanomaterial strategies need a minimally invasive delivery method such as an injection. Some nanomaterials strategies have emerged that allow for injection and can provide a facile and simple approach for clinical applications.(41, 120) However, the effect of shear stress on cell viability and cellular processes need detailed investigation using small and large animal models. Another challenge with nanomaterials is assessing their short-term and long-term toxicity, especially with the newly developed nanomaterials. Long-term accumulation of nanomaterials in body as well as inflammatory reaction due to degradation products of nanomaterials need more critical evaluation. Overall, nanoengineered scaffolds have become important components in interface tissue engineering since they offer an improvement in terms of design and control at the molecular level, although further studies must be conducted to evaluate their clinical relevance. The fieldwork has led to exciting advancements, and there is potential for nanomaterial-based scaffolds to emerge as new treatment methods for orthopedic interface tissue injuries.

In the following work, a nanosilicate-platform technology is presented to improve current interface tissue or regenerative engineering strategies. Specifically, we investigate nanosilicates, novel two-dimensional, bioactive nanomaterials which have the potential to replace traditional bioactive cues such as growth factors due to their unique biochemical and biophysical properties. We demonstrate the innate bioactivity of nanosilicates and their ability to direct human mesenchymal stem cell responses including osteogenic and chondrogenic differentiation. We further explore the biochemical property of nanosilicates, namely their ionic makeup ($Na^{+}_{0.7}[(Mg_{5.5}Li_{0.3}Si_{8}O_{20}(OH)_{4}]^{-}_{0.7}$) and subsequent dissociation in physiological environments, leading to their innate bioactivity. In addition, we utilize the biophysical property, or dual charged surface of nanosilicates to prolong and localize delivery of safe, therapeutic concentrations of growth factors to aid in osteogenic and chondrogenic differentiation of human mesenchymal stem cells. Finally, we demonstrate incorporation of nanosilicates into two natural polymers (gelatin methacrylate and methacrylated kappa carrageenan) allows for formation of gradient nanocomposite hydrogels in which cell morphology can be controlled. This gradient nanocomposite hydrogel could be used for future bone-cartilage interface tissue engineering. Importantly, this work provides a foundation for future tissue engineering strategies with the introduction of this nanosilicate-based platform as it can easily be modified for different tissue applications.

2. TWO DIMENSIONAL NANOSILICATES STIMULATE AND MODULATE HUMAN MESENCHYMAL STEM CELLS*

2.1 Introduction

2D nanomaterials have gained unprecedented attention due to their unique atomically thin, layered, and well-defined structure that provides distinctive physical and chemical properties compared to bulk 3D counterparts.(38, 121, 122) As the dimensions of 2D nanomaterials are only a few nanometers thick, they interact with biological moieties in a unique way and have raised exciting questions about their interactions with cellular components. In addition, different physical (*e.g.* size, shape, and charge) and chemical characteristics of 2D nanoparticles have a multitude of effects on cells including toxicity, bioactivity, or therapeutic capabilities, which are not well understood.(27, 123)

Understanding cellular responses following treatment with nanomaterials will aid in evaluating their application for a range of biomedical and biotechnology applications. Recent emergence in "omics" techniques providing readouts of different biological processes, have allowed us to understand complex biological interactions of synthetic nanoparticles and their toxicity.(124-127) Specifically, transcriptomics and proteomics have laid down the necessary foundation to provide

---

* Reprinted with permission from "Carrow J.K.; Cross L.M.; Reese R.W.; Jaiswal M.K.; Gregory C.A.; Kaunas R.; Singh I.; Gaharwar A.K. Widespread Changes in Transcriptome Profile of Human Mesenchymal Stem Cells Induced by Two-Dimensional (2D) Nanosilicates. PNAS, vol. 115, pp. E3095-E3913, April 2018." Copyright 2018 National Academy of Sciences.

an unbiased global view of the cellular activity with pivotal insights about the affected cellular pathways. Based on these results, a range of nanotechnology-based platforms have been developed for molecular diagnostics and genome-wide analysis.(128) We propose to utilize transcriptomics, high throughput sequencing of expressed transcripts (RNA-seq), to provide a holistic view of nanomaterial interactions with the cellular machinery. RNA-seq is a powerful tool for an accurate quantification of expressed transcripts that largely overcomes limitations and biases of microarrays.(129-131) In this study, we will evaluate the potential of bioactive 2D nanomaterials for regenerative medicine by uncovering molecular targets and affected signaling pathways at the whole transcriptome level.

Synthetic 2D nanoclays have been recently evaluated for regenerative medicine applications, due to their biocompatible characteristics, high surface-to-volume ratio, and uniform shape compared to other types of 2D nanomaterials.(38, 132-134) Synthetic clays such as nanosilicates ($Na^{+}_{0.7}[(Mg_{5.5}Li_{0.3}Si_{8}O_{20}(OH)_{4}]^{-}_{0.7}$, Laponite XLG®) have disc-shaped morphology and exhibit a dual charged surface.(135-137) Nanosilicates dissociate into nontoxic products (Na^{+}, Mg^{2+}, $Si(OH)_4$, Li^{+}) in physiological conditions and show one tenth of the cytotoxicity (LD_{50}~4 mg/mL)(138, 139) compared to other 2D nanomaterials such as graphene (LD_{50}~100 μg/mL).(140) These 2D nanosilicates are investigated for a range of biomedical applications including, tissue engineering, drug and therapeutic delivery, and bioprinting.(141-144) While these studies have generated encouraging results for 2D nanosilicates, their interactions affecting the transcriptome profiles remain unknown.

Here, we investigate the interactions of 2D nanosilicates with hMSCs by employing transcriptome dynamics to uncover triggered biophysical and biochemical cellular pathways. In doing so, we observed widespread changes in gene expression profile (> 4,000 genes) following nanosilicate exposure, which has not been reported previously. In addition, transcriptomic dynamics of nanosilicate treated-hMSCs identifies key genes and enriched gene ontology (GO) pathways and categories related to stem cell differentiation, specifically towards osteochondral lineages, which has not been previously reported. We validated the RNA-seq findings using *in vitro* studies which support the ability of nanosilicates to direct hMSC differentiation towards bone and cartilage lineages. Our study also investigated surface-mediated kinase signaling triggered by 2D nanosilicates. This work enables further development of nanomaterial-based therapeutics for regenerative medicine. More generally, transcriptomic analysis by next-generation sequencing provides a comprehensive and objective snapshot of cellular behavior following nanomaterial exposure/attachment. Furthermore, this study demonstrates the utility of next generation sequencing for the study of cellular interactions on nanoengineered substrates and the role this approach is likely to play in this rapidly expanding field of regenerative medicine.

2.2 Materials and Methods

2.2.1 Nanosilicate Characterization

Synthetic clay nanosilicates (Laponite XLG®, $Na^{+}_{0.7}[(Mg_{5.5}Li_{0.3}Si_{8}O_{20}(OH)_{4}]^{-}_{0.7}$), was obtained BYK Additives (Gonzales, TX). Authentication was performed by determining chemical composites, crystal structure, size and shape of nanosilicates. Specifically, inductively coupled plasma mass spectrometry (ICP-MS, Elemental Analysis (PerkinElmer NexION 300D) and X-ray photoelectron spectroscopy (XPS, Omicron XPS system with Argus detector) was used to determine chemical composition of nanosilicates. For ICP-MS, nanosilicates was dissolved in 0.5% hydrogen peroxide solution for 24 hours. ICP-MS analysis was performed to determine the concentrations of Si, Li, and Mg. Dried nanosilicates was used for XPS analysis, where binding energies for magnesium (Mg *2s*, *2p*), sodium (Na *1s*), oxygen (O *1s*), lithium (Li *1s*), and silicon (Si *2p*) were determined. The raw values were deconvoluted *via* Lorentzian function using GraphPad Prism. X-ray diffraction (XRD, Bruker D8 Advanced) was used to determine crystalline structure of nanosilicates. XRD was performed with a copper source on both powdered nanosilicates and exfoliated nanosilicates (in water) that were then flash-frozen in liquid nitrogen and lyophilized. Atomic force microscopy (AFM, Bruker Dimension Icon Nanoscope) and transmission electron microscopy (TEM) was performed to determine the size and shape of the nanosilicates. For both AFM and TEM, a dilute solution of exfoliated nanosilicates was placed on silicon substrate or carbon grid. For AFM, nanosilicate thickness was observed via tapping mode and the data was analysis using Nanoscope Analysis software. For TEM, an accelerating voltage of 200 kV using a JEOL-JEM 2010 (Japan) was used to determine the morphology of nanosilicates. The zeta potential and hydrodynamic size of nanosilicate-FBS solutions were measured with a Zetasizer Nano ZS (Malvern Instrument, U.K.) furnished with a He−Ne laser at 25°C. Filtered particles were achieved through utilization of a 0.2 µm filter.

2.2.2 *In vitro* Studies-Cytocompatibility, Cell Uptake, and Retention

Human mesenchymal stem cells (hMSCs) were acquired from the Texas A&M Institute for Regenerative Medicine (College Station, TX, USA) previously isolated and subsequently expanded from voluntary donors under an institutionally approved tissue recovery protocol. hMSCs were cultured under normal media conditions consisting of α-minimal essential media (alpha-MEM, Hyclone, GE Sciences) with 16.5% fetal bovine serum (Atlanta Biologicals, USA) and 1% penicillin/streptomycin (100 U/100 µg/mL, Gibco). After every 2-3 days, half of culture media was exchanged for fresh media. Cells were passaged with 0.5% trypsin-EDTA upon reaching confluency of ~70% and seeded at ~2500 cells/cm^2. All experiments were completed with cell populations under P5. Seeded cells were treated with and without nanosilicates (Laponite XLG®, $Na^+_{0.7}[(Mg_{5.5}Li_{0.3}Si_8O_{20}(OH)_4]^-_{0.7})$ solution (50 µg/mL) and cultured for 7 days.

Metabolic activity was monitored *via* MTT (3-(4, 5-dimethylthiazolyl-2)-2, 5-diphenyltetrazolium bromide) (ATCC) and Alamar Blue (Thermo Scientific) assays, per manufacture protocols. The BD Accuri C6 Flow Cytometer and a propidium iodide (PI, 40 µg/mL) stain with RNase (100 µg/mL) were used to perform cell cycle analysis following earlier protocol.(145) Prior to seeding, hMSCs were serum starved (only 1% FBS in media) for 24 hours to synchronize cell populations and then treated with nanosilicates. After 48 hours of exposure, cells treated with various concentrations of nanosilicates were trypsinized and fixed in ice cold 70% ethanol. Formed cell pellets were washed in PBS, followed by incubation in a PI staining solution at 37 °C for 30 minutes. Cells were stored at 4°C until flow cytometer analysis. For endocytosis inhibition analysis by flow cytometry, cells were cultured under normal conditions in 6-well plates. Cells were washed three times with PBS and then treated with inhibitors of clathrin-mediated, calveolar-mediated, or macropinocytosis (35 µM chlorpromazine hydrochloride, 10 µM nystatin or 400 nM wortmannin, respectively) (Sigma–Aldrich) at 37 ˚C for 30 minutes. After this pretreatment, silicate nanoparticles fluorescently tagged with Rhodamine B were added to the culture (final concentration 100 µg/ml) and incubated for a further 60 minutes. Subsequently, the cells were washed with PBS, trypsinized, and then suspended in cell culture medium. Particle uptake was then analyzed via flow cytometry. Hyperspectral images and data were captured using an Olympus research grade optical microscope equipped with CytoViva (Auburn, AL) patented enhanced darkfield illumination optics and full spectrum aluminum halogen source illumination. The system was also equipped with the CytoViva hyperspectral imaging system, producing spectral image files from 400nm-1,000nm at 2nm spectral resolution. CytoViva's customized version of ENVI hyperspectral image analysis software was used to quantify the sample's spectral response and conduct any spectral mapping of the sample elements.

For evaluation of reactive oxygen species (ROS) production, the BD Accuri C6 Flow Cytometer was used. hMSCs were cultured in a 12 well-plate to ~70% confluency then treated with an ERK inhibitor (PD184352, 5 µM) for 2 hours at 37 °C. Cells were then incubated with dihydroethidium (DHE, 25 µM) for 10 minutes 37 °C. Then, cells were washed with PBS and treated with 50 µg/mL nanosilicates in phenol-red free and serum free media for 2 hours at 37 °C. After 2 hours, cells were washed with PBS, trypsinized, spun down, and then re-suspended in PBS for flow cytometer analysis.

For lysosomal staining and actin staining, hMSCs were cultured in a 12-well plate to ~70% confluency. hMSCs were treated with 1 µL of CellLight® Lysosomes-GFP and incubated overnight at 37 °C for lysosomal staining. Then, hMSCs were treated with rhodamine-labelled nanosilicates for 3 hours at 37 °C and later fixed with 2.5% glutaraldehyde. Similarly, for actin staining, hMSCs were treated with nanosilicates for 24 hours, then fixed with 2.5% glutaraldehyde and permeabilized with 0.1% TritonX-100. Phalloidin stain was then added and samples were incubated for 1 hour at 37 °C. The stain was removed, washed with 1X PBS, and then samples were treated with propidium iodide/RNAase for 30 minutes at 37 °C. Both lysosomal stained and actin stained samples were imaged via a confocal microscope (Nikon). Further tracking of nanosilicates and lysosomal activity was done using the BD Accuri C6 Flow Cytometer. hMSCs were treated with rhodamine-labelled nanosilicates for 1, 3, and 7 days and then treated with CellLight® Lysosome-GFP overnight. Cells were then washed with PBS, trypsinized, spun down, and resuspended in PBS for analysis.

For investigating nanosilicate dissociation within hMSC culture, inductively coupled plasma mass spectrometry (ICP-MS, Elemental Analysis (PerkinElmer NexION 300D)) was performed. hMSCs were cultured with nanosilicates for 1, 3, and 7 days and then cells were washed with PBS, trypsinized, spun down and then resuspended in deionized water. After re-centrifugation, the pellet was digested in a 1% nitric acid, 0.5% hydrogen peroxide solution for ICP-MS analysis in which the concentrations of Si, Li, and Mg were determined. This digestion protocol was modified from earlier study.(146)

2.2.3 Whole-transcriptome Sequencing and Analysis

For total mRNA extraction, cells were cultured until 65% confluent and were subjected to two different media compositions for one week. One subset of cells maintained normal media conditions as a negative control (2 replicates); another group was treated with nanosilicates (Laponite XLG®, $Na^{+}_{0.7}[(Mg_{5.5}Li_{0.3}Si_{8}O_{20}(OH)_{4}]^{-}_{0.7})$ (50 µg/mL) for 48 hours (2 replicates), after which the media was replaced with normal media for the remaining five days. Excess nanosilicates were removed as they are expected to be cleared within 48 hours. Upon completion of the week, cells were washed with PBS and pelleted. RNA was isolated and collected via a Roche, High Purity

RNA Isolation kit following the manufacturer's protocol. Initial quality of nucleic material (~1.5-2.0 µg) was evaluated using spectrometer absorbance ratios between 280/260 nm around 2.0. Samples were analyzed *via* a high-output HiSeq platform with TruSeqRNA sample preparation and single-end read length of 125 bases (Genomics and Bioinformatics Service, Texas A&M AgriLife Research, Dr. Charlie Johnson). The sequenced reads were trimmed and aligned to the human genome (hg19) using a RNA-seq aligner, Spliced Transcripts Alignment to a Reference (STAR).(147) STAR is a RNA-seq alignment algorithm specifically designed for alignment of reads generated from spliced RNAs. For the control group, 21,563,695 (uniquely mapped 20,153,164) and 24,531,989 (uniquely mapped 22,900,448) sequenced reads successfully aligned to the genome for the two replicates. Similarly, 22,266,394 (uniquely mapped 20,623,575) and 15,769,384 (uniquely mapped 14,633,793) reads aligned to the genome for the nanosilicate treated group for both the replicates. For further analysis, only uniquely mapping reads were utilized. The Reference Sequence (RefSeq) genome annotation the human genome (hg19, GRCh37 Genome Reference Consortium Human Reference 37) obtained from UCSC genome browser was utilized for obtaining the gene definition. The gene models can also be obtained by using the Bioconductor package GenomicFeatures in R environment.(148) Expression of a gene was determined by counting the number of uniquely mapped reads overlapping the coding exons normalized by gene length in RPKM (reads per kilobase per million). We utilized RPKM to filter the expressed genes in the samples and not for comparison between samples. The distribution of expression of genes in each sample shows that 1 RPKM is a reasonable cutoff to remove the genes with no or minimal expression (Figure S4). Genes >1 RPKM were considered to be expressed in any condition if they were expressed in both the replicates. Genes expressed in at least one of the condition were then tested for differential expression. Generalized linear models (GLM) were used to identify the differentially expressed genes where the expression counts were modelled as negative binomial distribution.(149) The bioconductor package DESeq was used for this purpose. Prior to performing differential analysis DESeq estimates size factors for each sample for normalizing the samples. All analyses were done in R. The GO enrichment analysis was done using GOStats bioconductor package. For GO enrichment analysis, the background was only considered to be the expressed genes. REVIGO(150) was used to refine the extensive list of significant CC GO-terms. It reduces the functional redundancies and clusters the terms based on semantic similarity measures. Visualization of gene networks was accomplished through Cytoscape(151) and GeneMANIA(152) and ClueGO(153) by direct comparisons to a *Homo sapiens* reference genome. DAVID Bioinformatics Resources were also utilized for genetic network analysis.(154) Only genes with a p adjusted-value (Benjamini-Hochberg false discovery rate) less than 0.05 were included within the network and subsequent GO term network formation.

2.2.4 RNA-seq Validation Using qRT-PCR and Western Blot

For quantitative Reverse Transcription polymerase chain reaction (qRT-PCR), cells were cultured under similar conditions as RNA-seq. Following RNA isolation, cDNA was synthesized from 1 µg of RNA for each sample via SuperScript III Reverse Transcriptase (Thermo Fisher, United States) following manufacturer's protocol. Primers were designed via NCBI/Primer-BLAST and quality checked via Integrated DNA Technologies' OligoAnalyzer. Table 2-1 shows the primers designed and used. SYBR Green reagent was then used for amplification quantification. Expression and fold change values were calculated from fluorescence using the program DART-PCR.(155) For Western Blot analysis, cells were cultured under similar conditions as qRT-PCR and RNA-seq. Protein samples were isolated via a Laemmli Buffer (4% SDS, 20% glycerol, 10%

2-mercaptoethanol, 100 mM Tris HCl, and 0.2% bromophenol blue). Gel electrophoresis (Invitrogen, Mini Gel Tank) was performed on protein samples and subsequent gels were transferred (Invitrogen, iBlot 2) to a nitrocellulose membrane according to manufacture protocol. The membranes were blocked with 5% BSA in PBST (PBS + 0.1% Tween 20) for 30 minutes then western processed (Invitrogen, iBind). β-actin, COMP, p-MEK1/2, and COL1A1 primary antibodies and HRP conjugated secondary antibodies were purchased from Boster Bio and incubation was performed per manufacture protocols. Blots were developed (SuperSignalTM West Pico PLUS Chemiluminescent Substrate, ThermoFisher) and imaged via LI-COR® 3600 C-Digit Blot Scanner. Protein bands were quantified with LI-COR software. The blots were then restored and re-blocked with 5% BSA in PBST for further protein analysis.

Table 2-1. Primer Design for qRT-PCR

Gene	Forward Primer	Reverse Primer
GAPDH	5’-CCTTCATTGACCTCAACTACATGG-3’	5’-TGGAAGATGGTGATGGGATTTCC-3’
COMP	5’-AACAGTGCCCAGGAGGAC-3’	5’-TTGTCTACCACCTTGTCTGC-3’
ACAN	5’-AAGGGCGAGTGGAATGATGT-3’	5’-CGTTTGTAGGTGGTGGCTGTG-3’
CLTCL1	5’-TTTTGGCAGGTCAGGCATCC-3’	5’-ACCTGTGCTTTCCCAAGACT-3’
COL11A1	5’-GACTATCCCCTCTTCAGAACTGTTAAC-3’	5’-CTTCTATCAAGTGGTTTCGTGGTTT-3’
TXNIP	5’-ACACATGGTGCTCTTCAGGG-3’	5’-AGTTGGTATATGCAACAAGCCA-3’

2.2.5 *In vitro* Functional Study

For differentiation studies, hMSCs were treated with either osteogenic (normal media supplemented with 10 mM β-glycerphosphate and 50 μM ascorbic acid) or chondrogenic media

(DMEM supplemented with 1% ITS+, 10^{-7}M dexamethasone, and 1 mM sodium pyruvate) with and without nanosilicates. For osteogenic differentiation samples were fixed with 2.5% glutaraldehyde at 14 and 21 days and stained for alkaline phosphatase (1-Step NBT (nitro-blue tetrazolium chloride)/BCIP (5-bromo-4-chloro-3'-indolyphosphate p-toluidine salt) substrate solution, ThermoFisher Scientific) and mineralization (Alizarin Red S stain, Electron Microscopy Sciences), respectively. Alizarin Red was quantified via acetic acid extraction and subsequent colorimetric detection.(156) For chondrogenic differentiation, samples were fixed with 2.5% glutaraldehyde at various time points, washed with PBS, 1% acetic acid, and then quickly stained with 0.1% Safranin O for 5 minutes. Samples were washed again with PBS twice and then imaged. For immunostaining, fixed cells were incubated with a 1% BSA in PBST (PBS + 0.1% Tween 20) for 30 minutes to block nonspecific binding. Cells were then incubated with a mouse anti-human aggrecan primary antibody (Abcam, MA, USA) within a 1% BSA solution overnight at 4°C. The primary antibody was then removed and cells were washed with PBS multiple times. Subsequently, cells were incubated for 1 hour at room temperature with a goat anti-mouse IgG with conjugated Alexa Fluor® 647 (Abcam, MA, USA) in a 1% BSA solution. The secondary antibody was then decanted and cells were washed multiple times with PBS. Samples were stored in PBS in the dark at 4°C until imaging.

2.2.6 Statistical Analysis

Statistical analysis was performed via GraphPad Prism software. One-way ANOVA with post hoc Tuckey tests were performed. Significant significance values were determined as P values less than 0.5.

2.3 Results and Discussion

2.3.1 Biophysical and Biochemical Characterization of Nanosilicates

Chemical and structural characteristics of 2D nanomaterials will dictate their interactions with cells.(27) A range of material characterization techniques were used to establish the chemical composition, crystalline nature, shape, and size of nanomaterials.(157) Transmission electron microscopy (TEM) showed that nanosilicates were 20-50 nm in diameter (Figure 2-1a). X-ray photoelectron spectroscopy (XPS) revealed the presence of oxygen (54.68%), silicon (28.99%), magnesium (15.27%), sodium (0.84%), and lithium (trace), which is similar to expected stoichiometry ($Na^{+}_{0.7}[(Mg_{5.5}Li_{0.3}Si_{8}O_{20}(OH)_{4}]^{-}_{0.7}$) (Figure 2-1b). The thickness of nanosilicates was determined to be around 1-2 nm using atomic force microscopy (AFM) (Figure 2-1c). The crystalline structure of nanosilicates was corroborated by observing characteristics diffraction plan (001), (100), (005), (110), (200), and (300) using x-ray diffraction (XRD) (Figure 2-1d). After exfoliation, a decrease in 2θ (20.1° to 16.8°) for diffraction plane (100), indicates an increase in *d*-spacing between nanosilicates.

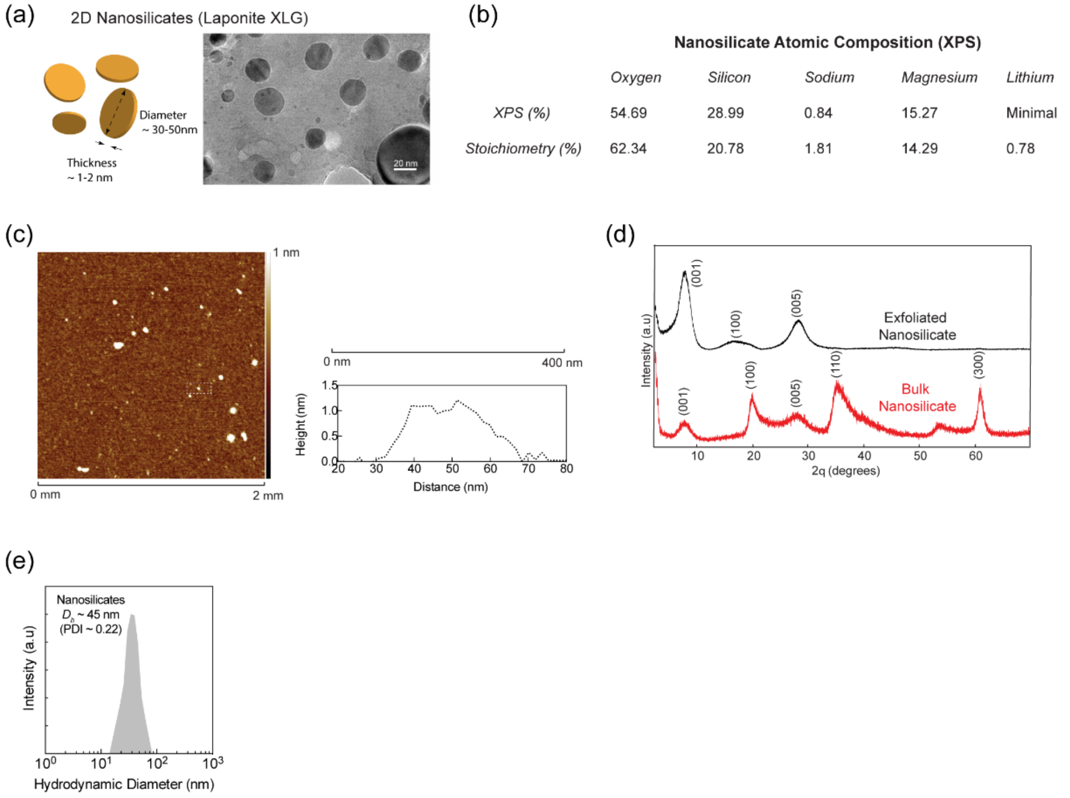

Nanosilicate Atomic Composition (XPS)

	Oxygen	Silicon	Sodium	Magnesium	Lithium
XPS (%)	54.69	28.99	0.84	15.27	Minimal
Stoichiometry (%)	62.34	20.78	1.81	14.29	0.78

Figure 2-1 Physical characterization of nanosilicates was completed to evaluate particles before introducing to hMSCs. (A) TEM of nanosilicates demonstrated disk morphology and nanoscale size. (B) XPS analysis revealed an elemental composition similar to that of the idealized stoichiometric ratio found within a unit cell of the nanosilicates. (C) AFM corroborated the nanoscale diameter (25-50 nm) and thickness (1-1.5 nm) of the nanosilicate. (D) XRD of both bulk and exfoliated (flash frozen with subsequent lyophilization) nanosilicates generated peaks at diffraction planes (001), (100), and (005) for both, with (110) and (300) present in bulk sample. (E) DLS measurements quantified variability of nanosilicates hydrodynamic size in particles and displayed a narrow range of diameters (polydispersity index, 0.22) around 45 nm.

In biological media, such as blood plasma, synovial fluid or even culture media, the surface of nanoparticles become coated with various biomolecules forming a protein corona. Oftentimes, this initiates internalization of nanoparticles *via* receptor-mediated endocytosis. The binding of proteins to the nanosilicate surface was evaluated by monitoring hydrodynamic diameter (D_H) and zeta potential (ζ). After mixing nanosilicates with media (containing fetal bovine serum), zeta potential of the nanoparticles shifted from -40 mV to -25 mV, indicating that the negatively charged surface of the nanosilicates was coated with biomolecules. Similarly, an increase in hydrodynamic diameter was observed from ~45 nm to ~90 nm after placement in biological media. These results indicated that nanosilicate surfaces strongly interacted with biomolecules *via* electrostatic interactions to result in physical adsorption thereby enhancing interactions at the nano-bio interface.

The effect of nanosilicates on cell health was evaluated by monitoring cytoskeletal organization, metabolic activity and cell cycle (Figure 2-2). An investigation into cell health *via* metabolic and viability assays (Alamar Blue and MTT) confirmed cytocompatibility of nanosilicates until the concentration of nanosilicates reached 100 µg/mL. In addition, hMSCs treated with nanosilicates showed similar cytoskeletal organization to untreated hMSCs. Cell cycle analysis also supported that the majority of cells were in G1 and G2 phases when treated with <100 µg/mL nanosilicates. These studies highlight that nanosilicates are cytocompatible.

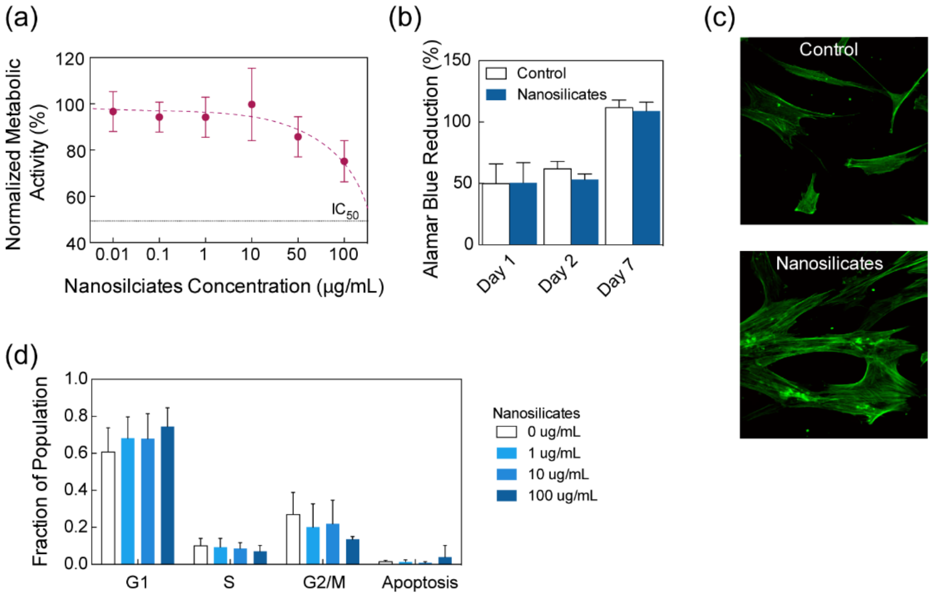

Figure 2-2 Nanosilicates effect on cellular processes. (A) Metabolic activity, assessed via MTT assay, remained unaffected by nanosilicate introduction at bioactive concentrations. Minimal effect of nanosilicates was observed on cell health monitored via (B) Alamar blue assay, (C) cytoskeletal organization, and (D) cell cycle analysis.

2.3.2 Receptor-Mediated Endocytosis of Nanosilicates

The absorbed proteins on the nanomaterial surface are predicted to influence cell surface receptor-mediated cellular uptake (Figure 2-3a). We used hyperspectral imaging(158) to visualize internalized nanosilicates (Figure 2-3b) without requiring chemical modifications that could have impacted uptake dynamics. Flow cytometry also demonstrated uptake of fluorescently labeled nanosilicates in a concentration-dependent manner (Figure 2-3c and Figure 2-4a, $R^2 = 0.996$).

The mechanism behind nanosilicate (50 µg/mL) internalization was evaluated using chemical inhibitors to block specific endocytic pathways. We observed a significant decrease in cellular uptake of nanosilicates (79.5% reduction) when treated with a clathrin inhibitor (chlorpromazine hydrochloride) (Figure 2-3d). Alternatively, other endocytic mechanisms such as caveolar-mediated (nystatin) and micropinocytosis (wortmannin) played a less prominent role in nanosilicate uptake. Furthermore, nanosilicate binding to the cell membrane and subsequent rapid internalization within 5 min (Figure 2-4b) are consistent with clathrin vesicle dynamics.(159) Colocalization of nanosilicates near or within lysosomal vesicles further confirmed nanosilicate trafficking (Figure 2-3d). These results indicated that nanosilicates are readily internalized by cells via clathrin-mediated endocytosis and transported to degradative cell machinery.

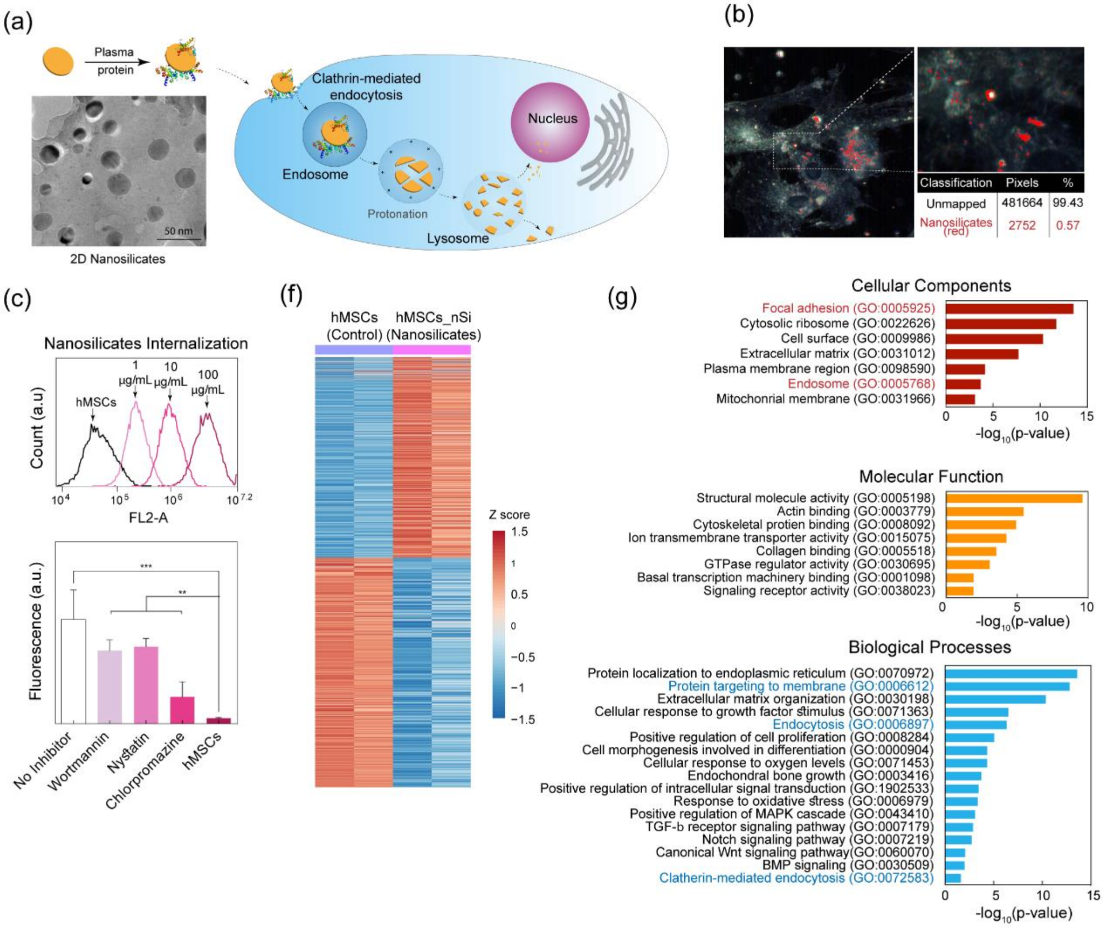

Figure 2-3 Biophysical interaction of nanosilicates and hMSCs. (A) Two-dimensional nanosilicates electrostatically bind to proteins from biological fluids and are subsequently internalized by cells via surface-mediated endocytosis. (B) Hyperspectral imaging indicating distribution of nanosilicates throughout the cell body following endocytosis. The image was captured from transverse section of cell body. (C) Flow cytometry analysis of rhodamine-tagged nanosilicates demonstrate dose-dependent cellular uptake. The nanosilicates were primarily internalized via clathrin-mediated process (chlorpromazine) as opposed to micropinocytosis (wortmannin) or caveolar-mediated (nystatin). ***P*-value < 0.01; ****P*-value < 0.001. (D) LAMP1 staining (green) for lysosomal membranes further tracks nanosilicates (red) following endocytosis. (F) Row-scaled z-scores of quantile normalized gene expression [in log2(RPKM)] of >4000genes following treatment with nanosilicates (padjust < 0.5, red, up-regulated: 1,897 genes; blue, down-regulated: 2,171 genes). (G) Significant gene ontology (GO) terms of associated biological processes, cellular components, and molecular functions from differentially regulated genes ($P < 0.5$). Terms related to biological process and cellular components indicate strong biophysical interactions between cells and nanosilicates. (E) Clustering of significant 244 cellular component GO terms into broader cellular component categories. (H) Gene network displaying interconnected genetic targets after nanosilicate treatment with high degrees of expression and statistical significance (red, up-regulated; blue, down-regulated; size increases with significance).

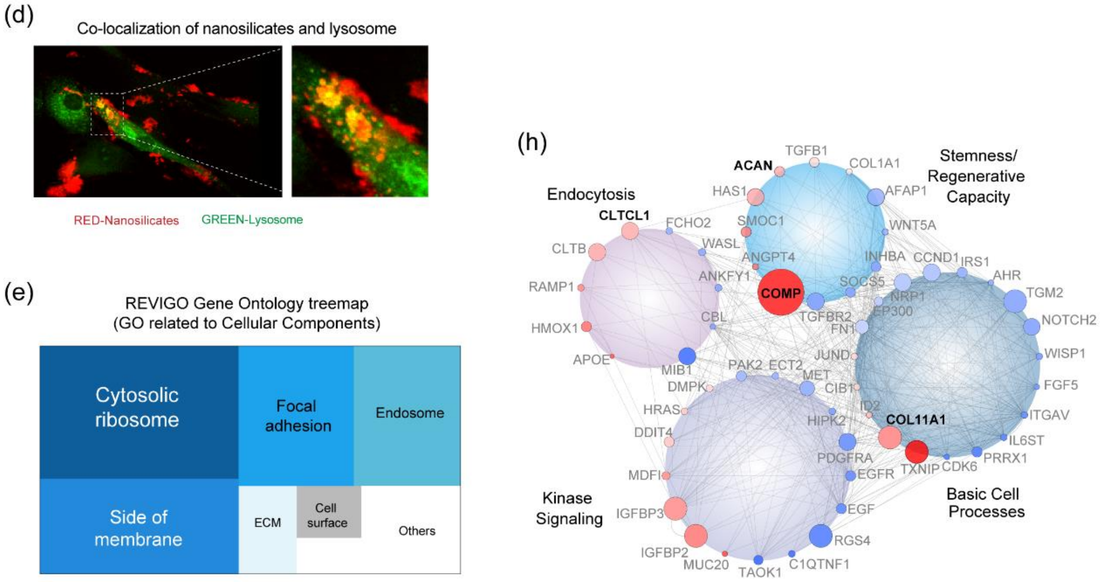

Figure 2-3 Continued.

Following uptake, nanosilicates remained within the cell for more than 7 days and were not exocytosed or dissociated immediately. The retention of nanosilicates by cells was determined using flow cytometry. A steady decrease was observed over a course of 7 days in cells staining positive for nanosilicates, that is, day 1 (96.3 ± 4.8%), day 3 (69.0 ± 10.6%), and day 7 (32.8 ± 19.5%) (Figure 2-4c). To further confirm this, we monitored nanosilicate retention by cells over a week with inductively coupled plasma mass spectrometry (ICP-MS) (Figure 2-4d). The nanosilicate content was decreased by 31% on day 7, compared with day 1. Over the course of 7 days, cells also maintained an enhanced lysosomal vesicle response (Figure 2-4c). The stability of nanosilicates in physiological microenvironment was evaluated at pH 7.4 (mimicking cell body) and pH 5.5 (mimicking intracellular compartment such as lysosome). A significantly higher release of minerals at pH 5.5 was observed compared with 7.4, indicated the predicted *in vitro* dissociation of nanosilicates. After 7 days, release of silicon (~10%), magnesium (~6%), and lithium (~16%) was observed at pH 5.5. These results indicate that nanosilicates were retained by hMSCs and possibly dissociate within lysosomes over a course of 7 days.

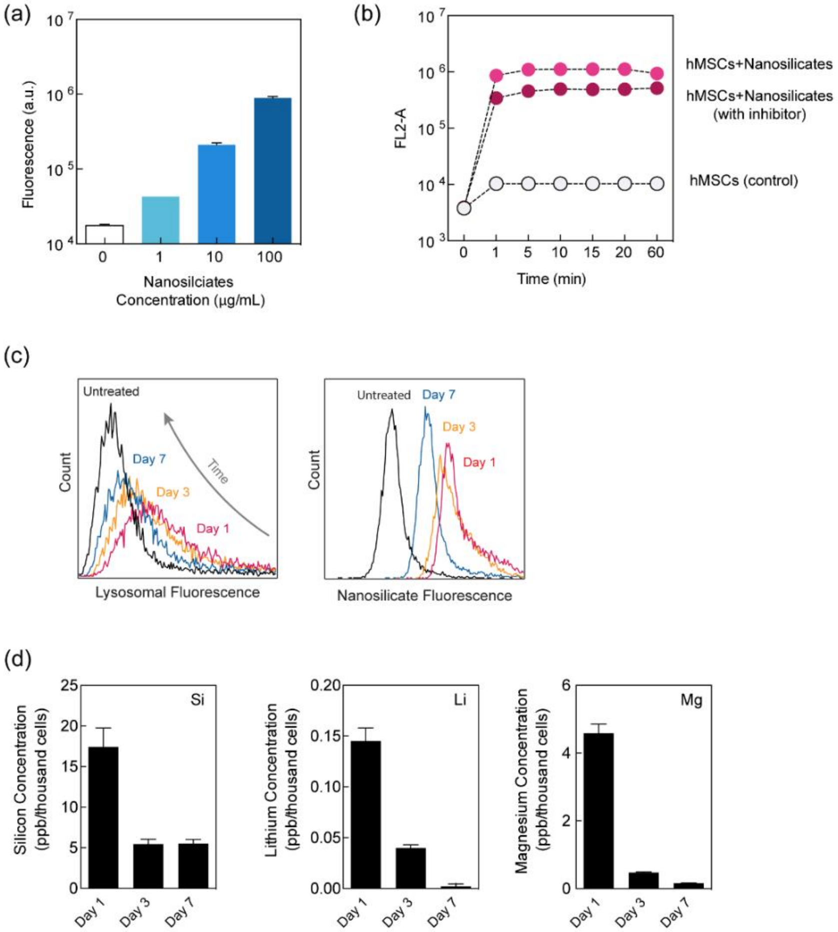

Figure 2-4 Nanosilicates interactions with hMSCs were monitored using flow cytometry and ICP-MS. (A) Uptake of fluorescently tagged nanosilicates displayed concentration-dependent internalization. (B) Endocytosis of particles occurred rapidly with chemical inhibition of a clathrin-mediated process reducing uptake. (C) Following internalization, tagged particles were trafficked to lysosomal bodies with an increase in these vesicles observed after 24 hours and returning to basal levels over the course of a week. (D) Introduction of nanosilicates to low-pH environments of late endosome/lysosome vesicles initiated dissolution of the particles over a week. Ion products were greatest at 24 hours and decreased over time as nanosilicates continued to be trafficked in and out of the cell in addition to particle dissociation.

Dissolution of nanosilicates inside cells can trigger biochemical signaling via release of minerals in cytosol. Earlier studies have shown that mineral ions can significantly influence cell functions. For example, silicon ions have been shown to direct stem cell differentiation by triggering cWnt signaling pathways and are critical for cartilage development.(160, 161) Likewise, magnesium ions have been shown to up-regulate production of COL10A1 and VEGF in hMSCs.(162) Lithium, an inhibitor of glycogen synthetase kinase-3β (GSK-3β), activates Wnt-responsive genes by elevating cytoplasmic β-catenin.(163, 164) These studies suggest that intracellular release of ionic dissolution products of nanosilicates ($Si(OH)_4$, Mg^{2+}, Li^{+},) could stimulate hMSC differentiation.

2.3.3 Widespread Transcriptomic Changes Triggered by Nanosilicates

Sequencing of expressed mRNAs by RNA-Seq can be used to determine genome-wide changes in gene expression resulting from cellular response to external stimuli.(165) hMSCs (2,500 cells per cm^2) were exposed to nanosilicates (50 µg/mL), and whole-transcriptome sequencing (RNA-seq) was performed after 7 days. (Materials and Methods). The 7-day time point was chosen to provide a broad overview of cell processes, ranging from endocytosis and proliferation to early differentiation. Two replicates of untreated and treated hMSCs were sequenced. The sequenced reads were aligned to reference genome (*hg19*) using RNA-seq aligner. The normalized gene expression levels were determined by calculating reads per kilobase of transcript per million (RPKM) (Figure A-1a,b). The replicates for both the conditions showed high concordance ($r = 0.99$, Figure A-1c). We used generalized linear models (GLMs) to identify differential gene expression (DGE) between nanosilicate treated hMSCs and untreated hMSCs (Materials and Methods). This comparison revealed significant changes in the expression level of 4,068 genes

(Figure 2-3e; 1,897 up-regulated genes, 2,171 down-regulated genes, false discovery rate-adjusted $P < 0.5$). Such widespread changes in gene expression profile have not been reported earlier. For example, human dermal fibroblast cells treated with gold nanoparticles were shown to differentially regulate 1,439 genes,(166) while another study demonstrated that human immune cells treated with graphene oxide experienced differential regulation of 1,147 genes.(167) It is important to note that these previously reported studies were performed using microarrays (166, 167) and the widespread effect of nanoparticles on whole transcriptome was not investigated. Thus, our result strongly suggests that nanoparticle treatment leads to a widespread cellular response that is reflected by the change in transcriptome profile of hMSCs treated with nanosilicates, requiring further exploration into prominent cellular pathways.

DGE following nanosilicate introduction spanned a host of cellular processes and functions. To identify the key biological processes and pathways that are affected when the cells interact with nanosilicates, we performed GO enrichment analysis of the three GO categories [biological processes (BP), cellular components (CC), and molecular functions (MF)]. Nanosilicate treatment showed significant enrichment for 1,132 GO terms ($P < 0.05$), including 884 for BP, 134 for CC, and 114 for MF (Figure A-1d). We then narrowed down key GO terms based on high significance (*P* value) in each category to highlight the widespread effect of nanosilicates on hMSCs (Figure 2-3f). The key GO terms significantly enriched in BP were endocytosis (GO: 0006897) and endochondral growth (GO: 0003416). The analysis also indicated positive regulation of mitogen-activated protein kinase (MAPK) cascade (GO:0043410), transforming growth factor-β (TGF-β) receptor signaling pathway (GO:0007179), notch signaling pathway (GO:0007219), canonical *Wingless* (cWnt) signaling pathway (GO:0060070), and bone morphogenic protein (BMP) signaling (GO:0030509). GO analysis also supported our observation that nanosilicates are internalized via clathrin-mediated endocytosis (GO:0072583). Overall, the GO enrichment analysis indicated that the predominant downstream effect of nanosilicates was on kinase activity, cell differentiation, and extracellular matrix (ECM) reorganization.

Functional annotation clustering performed using Database for Annotation Visualization and Integrated Discovery (DAVID)(168) highlights the role of cell membrane-mediated signaling due to nanosilicate treatment. We then use REVIGO(169) to refine the extensive list of significant CC GO terms by reducing functional redundancies and clustering the terms based on semantic similarity measures. GO for CC was enriched for cytosolic, ribosome, focal adhesion, and endosomal processes (Figure 2-3g and Figure A-1e). These results further suggested a sequence of events initiated at the cell membrane through protein localization to membrane (GO:0072657) and endocytic vesicle formation (GO:0006897, GO:0006898) accompanied by protein targeting to membrane (GO:0006612), and trafficking by lysosome (GO:0043202, GO:0005764). Specifically, genes involved in clathrin-mediated endocytosis (GO:0072583) like *CLTCL1*, which encodes a major protein of the polyhedral pit and vesicle coat, were significantly affected. To validate the clathrin-mediated endocytosis, change in expression level of *CLTCL1* was confirmed using quantitative reverse transcription-PCR (qRT-PCR) (Figure A-1f). We then clustered differentially expressed genes ($P < 0.5$) using Cytoscape(170) into different cellular processes such as basic cell processes, kinase signaling, endocytosis, and stemness/regenerative capacity (Materials and Methods). Networks between genes from same pathways were generated to illustrate connected and interdependent genes regulated by nanosilicate treatment (Figure 2-3h and Figure A-2).

Overall, these results demonstrate that nanosilicates significantly affect the transcriptomic profile of hMSCs, which can translate to measurable changes in behavior.

2.3.4 Nanosilicates Activate Surface-Mediated Signaling

The high surface-to-volume ratio and dual charged surface of nanosilicates are expected to facilitate strong interactions with the cell membrane. The physical interactions between cells and nanoparticles are expected to stimulate a variety of intracellular signaling events including proliferation and differentiation.(27, 171, 172) Accordingly, a significant change in expression of upstream regulators of *Ras* (e.g., *RalB*, *DDIT4*, and *HRAS*) and *Rho* (e.g., *DMPK*, *PAK2*, and *ECT2*) subfamilies of GTPases was observed upon nanosilicate treatment. These *Ras* and *Rho* genes are associated with peptidyl-serine phosphorylation (GO:0033135) and protein serine/threonine kinase activity (GO:0071900). Both Ras and Rho GTPase subfamilies affect cell behaviors such as cytoskeletal arrangement, cell migration, and stem cell fate.(173, 174) From analyzing enriched GO pathways related to stress, two prominent membrane-activated cascades emerged: the MAPK cascade and Janus kinase/signal transducers and activators of transcription (JAK/STAT) pathway (Figure 2-5a). Genetic markers specific to extracellular signal-regulated kinases (ERKs) ERK1/ERK2 regulation (GO:0070374, GO:0071363), stress-activated MAPK (GO:0032872, GO:0031098) cascades, and JAK/STAT cascade (GO:0007259) were also significantly altered following nanosilicate treatment. Among these enriched GO terms, multiple genes displayed notable log2fold changes in expression such as *IGFBP2* (insulin-like growth factor binding protein 2) (log2fold: 1.358), *IGFBP3* (1.149), *TAOK1* (-1.864), *PDGFRA* (-1.394), and *HIPK2* (-1.237). A significant change in gene expression of key MAPK signaling regulators was observed (Figure A-3b).

We also observed that a large number of genes (76 out of 170 genes) related to stress-activated protein kinase signaling (GO:0031098) were differentially expressed due to nanosilicate treatment (Figure 2-5b). Specifically, *TAOK1*, *TXNIP*, and *MAP4K4* exhibited a distinct difference in expression between nanosilicate-treated hMSCs compared with control hMSCs (Figure 2-5c and Figure A-3c). *TAOK1* is an activator or the p38/MAPK14 stress-activated cascade.(175) The change in mRNA expression levels of *TAOK1* via RNA-seq was further validated using qRT-PCR (Figure 2-5d). These data strongly support the ability of nanosilicates to stimulate MAPK cascade, specifically that of the ERK and p38 pathways (Figure 2-5e).

To experimentally validate the cross talk between MAPK signaling pathways following nanosilicate treatment, flow-cytometric analysis was performed. Reactive oxygen species (ROS) produced by cells treated with and without nanosilicates in presence of ERK inhibitor [PD184352, mitogen-activated protein kinase 1/2 (MEK1/2) inhibitor] were monitored using ROS-sensitive reporter fluorophore (Figure 2-5f). ROS play a role in the ERK pathway via cross talk from mitogen-activated protein kinase kinase kinases.(176) For nanosilicate-treated hMSCs, a significant reduction in ROS production was observed due to the presence of ERK inhibitor as seen by reduced fluorescence signal (~32% reduction, $P < 0.05$). This reduction in ROS production via the ERK inhibitor indicates the stimulation of MAPK signaling, specifically that of ERK, by the nanosilicates. The mechanism of this activation may stem from the biophysical cell-nanoparticle interaction, biochemical dissolution, or both in conjunction. This study validates that hMSCs recognize and respond to nanosilicates by engaging intracellular programs such as MAPK cascade (ERK1/2 and p38 kinases).

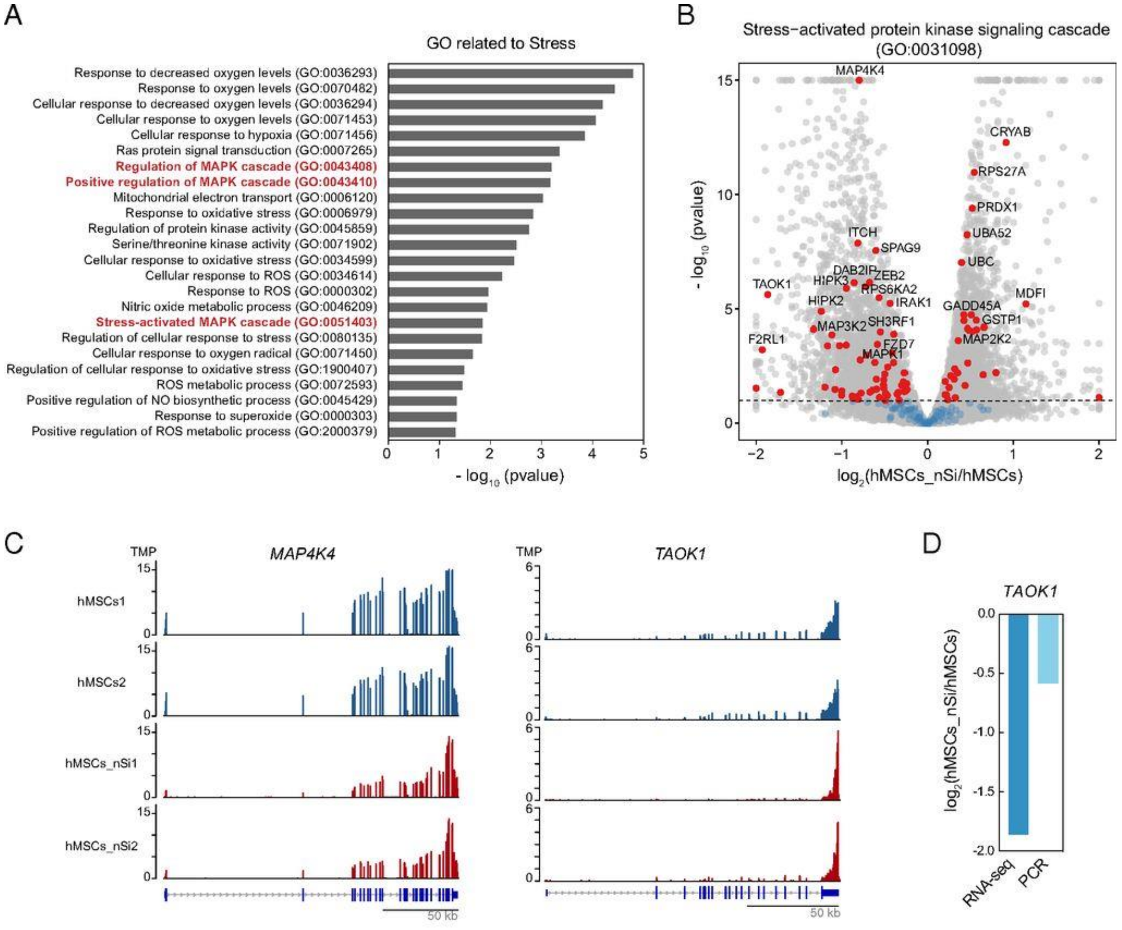

Figure 2-5 Nanosilicates lead to stress-induced MAPK signaling. (A) Nanosilicate treatment results in activation of stress-related response. A list of significant GO terms related to stress after nanosilicate treatment indicate signal propagation via MAPK/ERK signaling pathways. (B) The majority of genes involved in stress-activated kinase signaling cascade (GO:0031098) undergo a significant differential expression. (C) The change in gene expression profile of *MAP4K4* and *TAOK1* (aligned reads normalized by total library size). (D) Comparison of *TAOK1* gene expression obtained from RNA-seq was validated using qRT-PCR. (E) Nanosilicates trigger a stress-responsive kinase cascade (Ras-Raf-MEK-ERK pathways), leading to changes in reactive oxygen species (ROS) production and subsequent RNA transcription and protein synthesis. (F) Flow-cytometric analysis was performed to measure the stress-responsive kinase cascade, by measuring ROS production with ROS-sensitive fluorescent reporter dye. Experiments were performed in the presence or absence of a MAPK inhibitor. A significant increase in ROS-mediated fluorescent signal is observed upon exposure to nanosilicates, and this is abrogated after treatment with the MAPK inhibitor. $^{*}P < 0.05$; $^{**}P < 0.01$; $^{***}P < 0.001$; $^{****}P < 0.0001$. (G) Production of p-MEK1/2 was determined using Western blot in presence of nanosilicates and MEK inhibitor, establishing the role of nanosilicates in MAPK/ERK signaling. $^{*}P < 0.05$. ns, not significant.

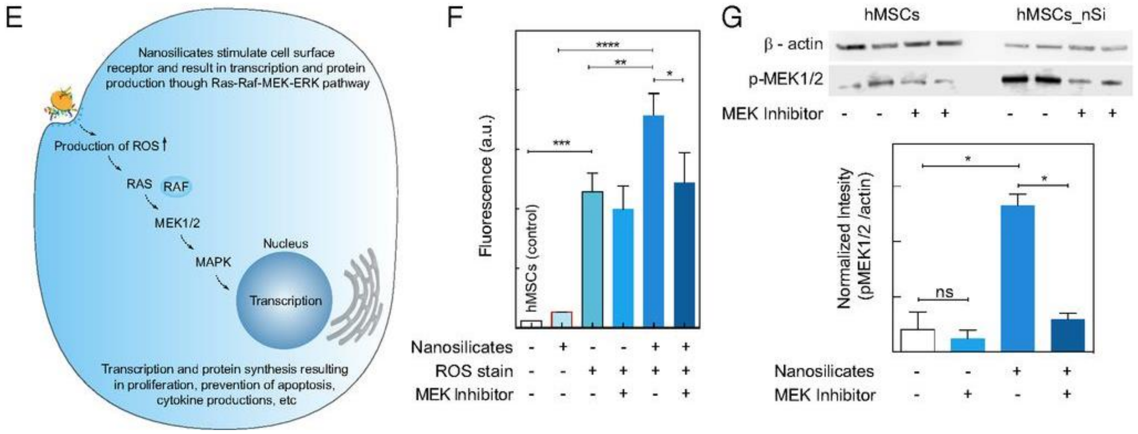

Figure 2-5 Continued.

While RNA-seq analysis provided insight about the role of nanosilicates in stimulating MAPK-related pathways, including those typically stimulated by growth factors in addition to stress-responsive kinases, monitoring protein levels can further provide functional evidence. Differential expression was observed in both upstream (e.g., *RAS*, *PRKCA*, and *BRAF*) and downstream (e.g., *ELK1*, *MKNK2*) genes of MEK1/2. In the MAPK/ERK cascade, MEK1 and MEK2 control cell growth and differentiation.(177) Activation of MEK1 and MEK2 occurs through phosphorylation by Raf. MEK1.2 inhibitors have been used extensively to implicate ERK1/2 in a wide array of biological events. To validate MAPK/ERK pathways, we monitored synthesis and phosphorylation of MEK1/2 (p-MEK1/2) with and without a MEK1/2 inhibitor (Figure 2-5g) via Western blot. hMSCs had relatively low production of p-MEK1/2, while nanosilicate treatment results in more than six-fold increase in p-MEK1/2. In the presence of MEK1/2 inhibitor, production of p-MEK1/2 in the presence of nanosilicates was suppressed, demonstrating the role of nanosilicates in activating the MAPK/ERK pathway.

Beyond intracellular phosphorylation events within MAPK cascades, we also observed genes that play a role in controlling background processes of hMSCs, like multipotency and motility, that have been identified in literature.(178) RNA-seq analysis revealed a significant change in gene expression: *AFAP1* ($\log_2$foldΔ: -1.152), *SOCS5* (-1.192), *WNT5A* (-1.162), *INHBA* (-1.179) from a variety of pathways including TGF-β, JAK/STAT, Wnt/ β -catenin, and phosphatidylinositol-3-kinase (PI3K) signaling. As this subset of genes is involved in cell proliferation, stromal cell multipotency, and extracellular matrix production,(179-181) nanosilicates may therefore improve functional tissue regeneration. Therefore, we were prompted to investigate these downstream pathways using molecular analysis techniques.

2.3.5 Nanosilicates Direct Stem Cell Differentiation

Following nanosilicate treatment, activation of the membrane can lead to differentiation and extracellular matrix deposition, following an ERK-based cascade. The kinase signaling follows similar progressions in hMSCs after growth factor simulation to promote osteochondral differentiation.(182-186) Evidence of hMSC inclination toward bone and cartilage lineages following nanosilicate treatment was observed with GO term enrichment (Figure 2-6a and Figure A-4). GO pathways and biological processes related to osteogenesis, such as bone development (GO:0060348), endochondral bone growth (GO:0003416), biomineral tissue development (GO:0031214), and canonical Wnt signaling pathway (GO:0060070) were favored toward osteogenesis. For chondrogenesis, cellular response to transforming growth factor-β stimulus (GO:0071560), cartilage development involved in endochondral bone morphogenesis (GO:0060351), and hyaluronan metabolic process (GO:0030212) were significantly altered. We observed a large fraction of genes with differential expression due to nanosilicate treatment. For example, 49 out of 92 genes were differentially expressed for bone development (GO:0060348), while 10 out of 14 genes were differentially expressed for cartilage development (GO:0060351) (Figure 2-6b). Genes from these GO categories including cartilage oligomeric matrix protein (*COMP*), collagen type I α1 chain (*COL1A1*), collagen type XI α1 chain (*COL11A1*), and aggrecan (*ACAN*), were significantly up-regulated due to nanosilicate treatment (Figure 2-6c and Figure A-5a) We further validated these genes using qRT-PCR and observed comparable gene expression to that of RNA-seq (Figure 2-6d).

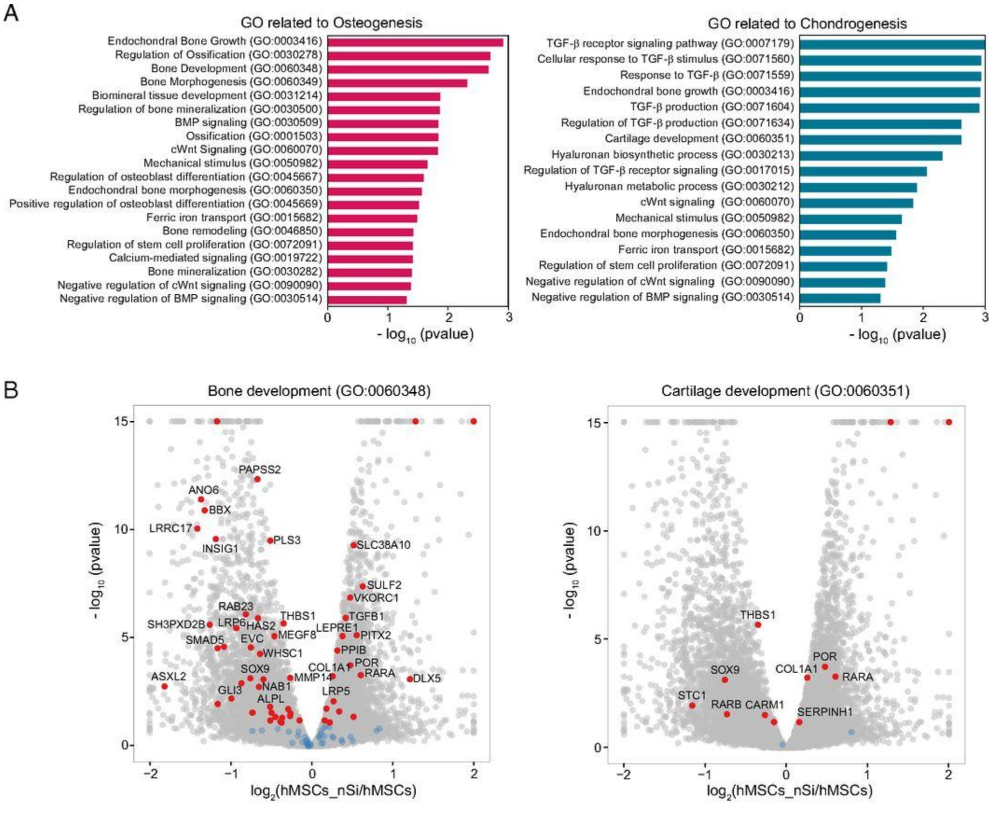

Figure 2-6 Transcriptomic analysis elucidates nanosilicate-induced bioactivity. (A) GO terms related to osteogenesis and chondrogenesis indicate nanosilicate-induced hMSC differentiation. (B) Significant gene expression changes in genes involved in bone development (GO:0060348) and cartilage development (GO:0060351). (C) Gene expression profile of *COMP*, *COL11A1*, and *ACAN*, demonstrating up-regulation due to nanosilicate treatment (aligned reads normalized by library size). (D) Differential gene expression from RNA-seq was validated using qRT-PCR, indicating similar trend.

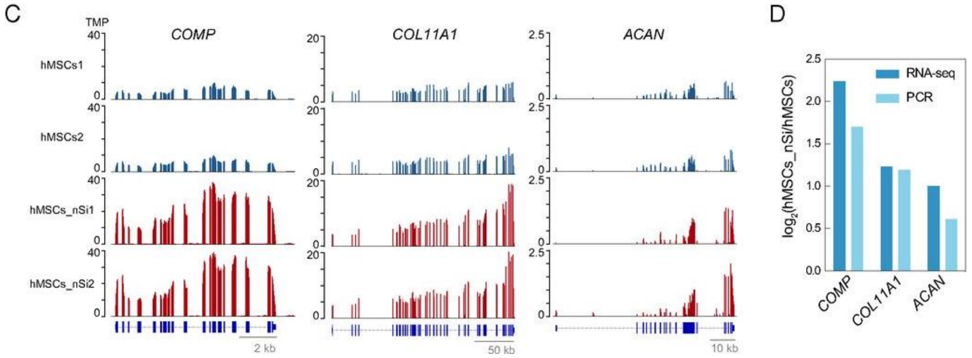

Figure 2-6 Continued.

To ensure that the mRNA detected represented up-regulated protein levels, a Western blot for COMP and COL1A1 was performed on day 7. Both COMP and COL1A1 protein showed a significant increase in expression due to nanosilicate treatment, indicating their role in hMSC differentiation (Figure 2-7a). Based on the changes in transcriptomic profile and *in vitro* validation, we hypothesize that the activation of MAPK/ERK pathways by nanosilicates may lead to differentiation into osteochondral lineages. To confirm the role of nanosilicates in stimulating MAPK/ERK signaling for hMSC differentiation, a MEK1/2 inhibitor was utilized and resulted in a significant decrease in COMP protein synthesis (Figure A-5b). This indicated the role of nanosilicates in the activation of MAPK/ERK signaling to direct the differentiation of hMSCs.

Finally, to further substantiate the ability of nanosilicates to drive hMSC differentiation toward bone and cartilage lineages, staining of lineage-specific proteins and matrix mineralization was performed. The effect of nanosilicates on chondrogenic and osteogenic differentiation was monitored by subjecting nanosilicate-treated hMSCs to chondro-conductive (lacking TGF-β) and osteo-conductive (lacking bone morphogenetic protein 2 (BMP2) or dexamethasone) media. After 21 days, production of chondro- and osteo-related ECM was observed even in the absence of inductive supplements. An increase in both glycosaminoglycan (GAGs) and aggrecan production were observed in nanosilicate-treated hMSCs indicating chondrogenic differentiation (Figure 2-7b), while for osteogenic differentiation, an increase in alkaline phosphatase (ALP) production as well as matrix mineralization (calcium phosphate) were observed (Figure 2-7c). These results validated the ability of nanosilicates to induce hMSC differentiation into bone and cartilage lineages without the use of inductive agents and growth factors.

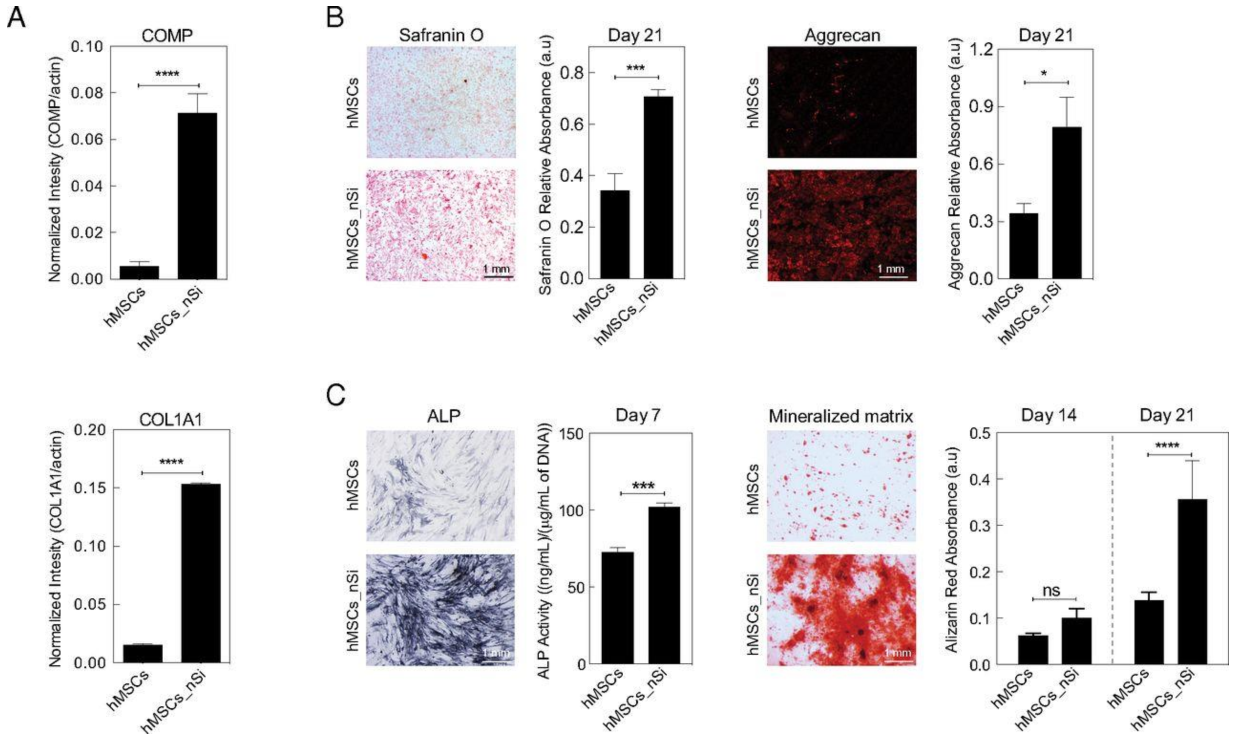

Figure 2-7 Nanosilicate-induced hMSC differentiation. (A) Western blot showing production of COL1A1 and COMP after exposure to nanosilicates for 7 days in normal media. (B) The effect of nanosilicates on production of GAGs was determined by safranin O and aggrecan staining after culturing hMSCs in chondro-conductive media for 21 days. (C) The effect of nanosilicates on osteogenic differentiation was determined by ALP activity and formation of mineralized matrix after culturing hMSCs in osteo-conductive media for 21 days. *$P < 0.05$; ***$P < 0.001$; ****$P < 0.0001$; n, not significant.

The broader relevance of our study is that “omics” techniques can be used to determine the effect of nanomaterials on cells in a nontargeted and nonbiased approach. The physiochemical properties of engineered nanomaterials such as size, shape, surface charge, and chemical composition will have profound effects on cellular behavior.(27, 171) Therefore, we do not speculate that the transcriptomic changes observed in this study will be universal to all types of nanomaterials or even single-cell analyses. Recent studies have used bulk population “omics” approaches to understand nanotoxicology and mechanism-based risk assessment of nanomaterials.(187, 188) The current study demonstrates the capabilities of next generation sequencing to monitor mRNA expression levels in the cell after nanomaterial treatment. Our approach overcomes the limitation of measuring expression levels of preselected genes on microarrays, which can therefore identify previously neglected cellular signaling pathways relevant for regeneration. Additionally, RNA-seq delivers a low background signal and sequenced reads that can be unambiguously mapped to unique regions of the genome, which will help in sensitive and precise identification of the expressed genes. The transcriptomic insight on the role of surface-mediated cellular signaling supports the ability of nanosilicates to induce hMSC differentiation into bone and cartilage linages in the absence of inductive agents. This insight can assist in reducing or eliminating the use of supraphysiological doses of growth factors currently employed in clinical practice for regenerative therapies. These omics techniques can likewise reveal cell-material interactions unique to specific nanoparticles and can contribute directly to the design of bioactive nanomaterials for regenerative medicine.

2.4 Conclusion

Overall, we investigated a transcriptomic snapshot of hMSCs in which a widespread change in transcriptomic profile was observed in response to nanosilicate exposure. The transcriptomic changes observed due to nanosilicate treatment likely originate from both biophysical and biochemical mechanisms. The interaction of nanosilicates with the cell membrane stimulated various surface receptors, including the stress-responsive and surface receptor-mediated MAPK pathways. Similarly, the data indicate that internalization of nanosilicates and subsequent release of mineral ions trigger biochemical signaling that could promote osteochondral differentiation of hMSCs. Accordingly, analysis of the transcriptomic snapshot of hMSCs treated with nanosilicates uncovered families of genes related to osteochondral differentiation. *In vitro* studies validated the RNA-seq findings and further supported the observation that nanosilicates have the capacity to direct hMSC differentiation toward bone and cartilage lineages. Last, RNA-seq emerged as a viable technique to evaluate the regenerative potential of novel nanomaterials.

3. MINERAL NANOPARTICLE DISSOCIATION INFLUENCES HUMAN MESENCHYMAL STEM CELL OSTEOGENIC DIFFERENTIATION

3.1 Introduction

Traditional regenerative medicine strategies adhere to the tissue engineering paradigm in which cells and bioactive cues are incorporated into a scaffold to mimic native tissue.(189, 190) While this approach has been successful, recently, the use of conventional bioactive cues, specifically growth factors, has become unfavorable. Once growth factors are delivered to the physiological space, they are volatile and susceptible to rapid degradation.(191, 192) As a result, clinicians must use large or supraphysiological doses of growth factors, 100-1000-fold higher compared to physiological concentrations, to maintain therapeutic efficacy. However, the use of the high doses has then led to several negative side effects including inflammation and uncontrolled tissue growth.(193-196) Due to the rise in these complications, researchers are investigating strategies to reduce and potentially replace these traditional bioactive proteins while maintaining cellular modulation capabilities.

One such alternative, specifically mineral-based nanoparticles, has gained interest in regenerative engineering. The mineral composition of these particles can be tailored toward specific regenerative applications through the release or dissolution of unique ionic products, which can directly stimulate cellular processes.(197) As a result, these mineral-based particles have the potential to replace conventional bioactive cues. An emergent mineral-based nanomaterial, termed nanosilicates ($Na^{+}_{0.7}[(Mg_{5.5}Li_{0.3})Si_8O_{20}(OH)_4]^{-0.7}$, Laponite XLG), has been investigated for a variety of biomedical applications, including regenerative engineering.(141, 198, 199) Nanosilicates have not only demonstrated high cytocompatibility with human mesenchymal stem cells (hMSCs), but also innate bioactivity.(32, 200, 201) Specifically, a recent study using RNA-sequencing of hMSCs after exposure to nanosilicates, revealed upregulation of osteogenic and chondrogenic differentiation in the absence of growth factors.(201) While these studies have produced encouraging results for nanosilicate innate bioactivity, the use of nanosilicates as an alternative bioactive cue to replace or augment growth factors remains elusive due to the undefined mechanism of action.

Previous investigation into nanosilicate-cell interaction has shown these particles to be internalized via clathrin mediated endocytosis.(139, 201) In addition, previous studies have shown nanosilicate dissolution or dissociation into Li^+, Mg^{2+}, and $Si(OH)_4$ at pH below ~9 and the extracellular and intracellular physiological pH of 7.4 and 5.5, respectively, facilitate this dissociation.(136, 202) We believe the genetic changes observed in the previous RNA-seq study could result from the chemical makeup of the nanosilicates and subsequent ion dissociation following particle uptake. Some earlier studies have investigated specific ions individually and demonstrated their potential to stimulate pathways related to osteogenic differentiation. For example, Li^+ inhibits glycogen synthetase kinas-3β (GSK-3β) which activates Wnt-responsive genes elevating cytosolic β-catenin.(163, 164, 203) Both *ex vivo* and *in vivo* studies have demonstrated Li^+ to initiate Wnt signaling which in turn stimulates osteogenesis.(163) In addition, $Si(OH)_4$ promotes collagen type I synthesis and osteoblast differentiation via Wnt/B-catenin signaling.(160, 161) Finally, Mg^{2+} has been deposited onto biomaterial surfaces to improve cell adhesion since divalent cations affect integrin function.(162, 204) This is important as integrins mediate communication between the extracellular environment and cells and control cellular processes such as proliferation and differentiation.(204-206) While these previous studies have demonstrated the potential for individual ions to induce osteogenic differentiation, the inclusion into a single nanoparticle allows for intracellular delivery and local release of the ions. We aim to investigate the effect of individual ions dissociated from the nanosilicates on osteogenic differentiation of hMSCs.

In this study, we investigate a potential underlying causation of nanosilicate-induced osteogenic differentiation, specifically, the effect of the individual ions contained in nanosilicates. We examine nanosilicate dissociation at physiological pH, as well as the role of these individual degradation products (lithium, magnesium, and silicon) in osteogenic differentiation of hMSCs. These investigations will provide further understanding of nanosilicate-induced osteogenesis as well as further establish this mineral-based material as an alternative bioactive cue for bone regeneration.

3.2 Materials and Methods

3.2.1 Nanosilicate Dissociation in Physiologically Relevant pH

The release of minerals from nanosilicates at physiologically relevant pH was monitored using Inductively-Coupled Plasma Mass Spectrometry (ICP-MS) – Elemental Analysis (PerkinElmer NexION 300D). Nanosilicates (Laponite-XLG, BYK Ind, USA) were dispersed in distilled water of various pH (5.5, 7.4, and 10) and dialyzed against the same water over a period of 30 days at room temperature. At various time points (0.125, 1, 3, 7, 21 days) half of the dialysis water was collected and replaced with fresh water. The collected dialysis water was then diluted into a 1%

nitric acid solution for ICP-MS analysis in which the concentrations of Li, Mg, and Si were determined.

3.2.2 Evaluation of Nanosilicate Dissociation Products on hMSC Metabolic Activity

All experiments were performed with hMSCs passage 5 or lower and cells were cultured in normal media (α-modified minimal essential media (AMEM); Hyclone), 16.5% fetal bovine serum (FBS; Atlanta Biological), and 1% penicillin/streptomycin (Gibco), unless otherwise stated. Mineral solutions of concentrations related to ICP results were prepared using lithium chloride (LiCl), magnesium sulfate ($MgSO_4$), and sodium silicate (Na_2O_3Si). hMSCs were seeded in 96 well-plates at a density of 10,000 cells/cm^2 and after 24 hours, were subjected to various mineral concentrations for an additional 24 hours. Minerals were then removed and an MTT assay (ATCC), was performed according to manufacture protocol. In addition, once desired concentrations were determined, an Alamar Blue assay (ThermoFisher) was performed at 1, 3, 7, and 14 days to quantify metabolic activity. For both MTT and Alamar Blue control groups consisted of untreated cells (negative) and cells treated with nanosilicates (positive).

3.2.3 Evaluation of Nanosilicate Dissociation Products on hMSC Osteogenic Differentiation

For osteogenic differentiation studies, hMSCs were similarly seeded in 96 well-plates at a density of 4,000 cells/cm^2. After 24 hours, cells were treated with osteoconductive media (normal growth media supplemented with 10 mM β-glycerophosphate (Sigma-Aldrich) and 50 μM ascorbic acid (BDH Chemicals)) and the various mineral concentrations (4.49 μg/mL silicon, 0.067 μg/mL lithium, and 1.59 μg/mL magnesium) for an additional 48 hours; similar controls were used. After 48 hours, minerals and nanosilicates were removed and cells were continuously treated with osteoconductive media and minerals for the remainder of the differentiation study. To analyze osteogenic differentiation, alkaline phosphatase (ALP) staining and kinetic activity were monitored along with matrix mineralization and quantification. First, hMSCs were fixed with 2.5% glutaraldehyde for 15-20 minutes. At 7 and 14 days, ALP staining was done using NBT/BCIP 1-steps solution (Nitroblue tetrazolium/5-Bromo-4-chloro-3-indolyl phosphate; ThermoFisher) for 30-60 minutes at room temperature. For quantification of ALP activity, hMSCs were incubated with alkaline phosphatase yellow (Sensolyte® pNPP ALP assay kit, AnaSpec). Using an automated plate reader (Tecan), ALP activity as a function of pNPP metabolism (ΔOD405) was measured and activity was normalized to DNA (picogreen, ThermoFisher). After 14 and 21 days, Alizarin Red staining (ARS; Electron Microscopy Sciences) was performed. The bound ARS, which is proportional to calcified matrix, and was quantified by dissolution in acetic acid (10%), neutralized by ammonium hydroxide (10%), and then measured in an automated plate reader (ΔOD405; Tecan). Both ALP and mineralized matrix were visualized with a stereomicroscope (Zeiss).

For western blot, proteins were isolated after 14 days with Laemmli Buffer (0.2% bromophenol blue, 20% glycerol, 100 mM Tris HCl, 10% 2-mercaptoethanol, and 4% SDS). Protein samples were separated via gel electrophoresis (Invitrogen, Mini Gel Tank) and gels were then transferred (Invitrogen, iBlot 2) to a nitrocellulose membrane per manufacture protocol. Membranes were blocked with 5% BSA in PBST (1X PBS with 0.1% Tween20) for 30 minutes prior to antibody staining. B-actin, ALPL, osteocalcin (OCN), and osteopontin (OPN) primary antibodies were purchased from ThermoFisher, secondary HRP conjugated antibodies were purchased from Boster Bio, and incubation was performed following manufacture protocols. Membranes were developed

(SuperSignal^{TM} West Pico PLUS Chemiluminescent Substrate, ThermoFisher) and imaged using LI-COR® 3600 C-Digit Blot Scanner. LI-COR software was used to quantify protein bands. Restoration and re-blocking with 5% BSA in PBST of the membranes was then done for further protein analysis.

Gene expression was evaluated via quantitative reverse transcription polymerase chain reaction (qRT-PCR). After 14 days of culture, RNA was isolated with Roche, High Purity RNA Isolation kit following manufacture's protocol. Nucleic material quality was evaluated via spectrometer absorbance ratio between 280/260 nm around 2.0. cDNA synthesis was then performed from 1 µg of RNA using Quanta Bio qScript^{TM} cDNA SuperMix following manufacture's protocol. Primers were either designed via NCBI/Primer-BLAST or taken from previous literature and checked for quality via Integrated DNA Technologies' OligoAnalyzer. Table 3-1 shows the primers designed and used. For qRT-PCR, SYBR Green Reagent (ThermoFisher) was used for amplification and samples were run and gene expression analyzed via QuantStudio 3 Real Time PCR (ThermoFisher) and QuantStudio^{TM} Design and Analysis Software (ThermoFisher), respectively.

Table 3-1. Primer Design for qRT-PCR

Gene	**Forward Primer**	**Reverse Primer**
GAPDH	5'-CCTTCATTGACCTCAACTACATGG-3'	5'-TGGAAGATGGTGATGGGATTTCC-3'
ALPL	5'- ACC ATT CCC ACG TCT TCA CAT TT-3'	5'-AGA CAT TCT CTC GTT CAC CGC C-3'
COL1A1	5'-GTCATCGCACAACACCTTGC-3'	5'-CACTACTGACAACGCCCCTC-3'

3.2.4 Statistical Analysis

Statistical analysis was performed in GraphPad Prism. One-way analysis of variance (ANOVA) coupled with Tukey's post-hoc were performed. Plots were graphed as mean and standard deviation and statistical significance is presented as $^*P$-value < 0.05, $^{**}P$-value < 0.01, $^{***}P$-value < 0.001, and $^{****}P$-value < 0.0001.

3.3 Results and Discussion

3.3.1 Nanosilicate Dissociation Occurs at Physiologically Relevant pH

Nanosilicates ($Na^+_{0.7}[(Mg_{5.5}Li_{0.3})Si_8O_{20}(OH)_4]^{-0.7}$) are composed of layered structures of octahedral magnesium and lithium ions sandwiched between tetrahedral silicon ions. Our central hypothesis is than in aqueous solutions with pH<9, nanosilicates dissociate into their nontoxic products (Li^+, $Si(OH)_4$, and Mg^{2+}). As previously discussed, nanosilicates are internalized by hMSCs predominantly via clathrin-mediated endocytosis and dissociation of nanosilicates likely occurs in the endosome due to the low pH (5.5).(201) In addition, the extracellular environment has pH~7.4 which could facilitate nanosilicate dissociation (Figure 3-1a). Therefore, we investigated nanosilicate dissociation at different relevant pH (5.5, 7.4, and 10) and determined the concentration of the dissociation products (Li^+, Si^{4+}, Mg^{2+}) through Inductively-Coupled Mass Spectrometry (ICP-MS) (Figure 3-1b). Ion dissociation from a nanosilicate solution (50 ug/mL dispersed in 10 mL of deionized water) was monitored for 21 days at pH of 5.5 (mimicking intracellular pH), 7.4 (mimicking extracellular pH), and 10 (isoelectric point of nanosilicates). As expected, at the lower pH (5.5 and 7.4), higher concentrations of ions were present supporting our hypothesis that nanosilicate dissociation occurs at physiological pH. The concentration of lithium was the lowest (0.09 ± 0.042 µg/mL) compared to magnesium (2.19 ± 0.99 µg/mL) and silicon

(5.89 ± 2.65 µg/mL) dissociation over 21 days at pH 5.5. While the concentration of lithium released was the lowest of the three ions across all pH, the percent released of lithium (63.94% at pH 5.5) was the greatest. Lithium ion release may occur more rapidly than magnesium or silicon ion release as lithium ions are bound by a hydroxide (OH^-) as opposed to an oxide. Previous studies have reported that after Laponite is dispersed in water, OH^- ions dissociate from the edge.(202) Specifically, at lower pH, the nanosilicates attempt to re-stabilize a basic pH via release of OH^-. In addition, monovalent lithium is less stable than divalent magnesium or tetravalence silicon, so release of lithium occurs more rapidly. Silicon ion release (40.05% release at pH 5.5) was also observed to be greater than that of magnesium (25.02% release at pH 5.5), as silicon ions are present on the outer layer and are more susceptible to dissociation. After 21 days, the average percent released of individual ions at physiologically relevant pH (7.4 and 5.5) were 30.54% (4.49 ± 1.98 µg/mL) silicon, 49.27% (0.067 ± 0.03 µg/mL) lithium, and 18.17% (1.59 ± 0.85 µg/mL) magnesium. To further investigate the effect of these individual ions on cell behavior and osteogenic differentiation, these average percent released of the ions at physiological pH after 21 days were chosen for subsequent *in vitro* studies.

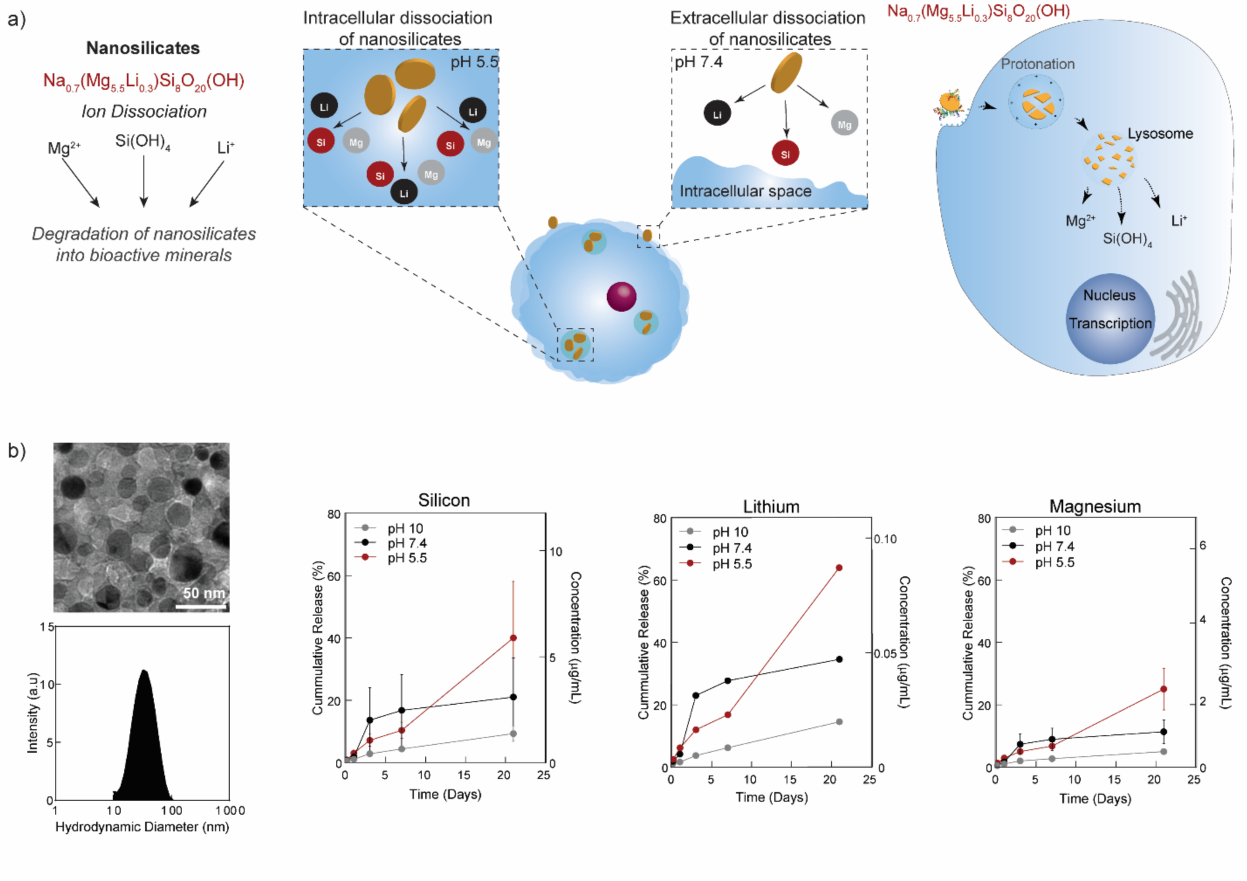

Figure 3-1 Nanosilicate dissociation at physiological pH. (a) Nanosilicates begin to dissociate at pH<9 so once introduced to the extracellular (pH 7.4) and intracellular (pH 5.5) microenvironment, ion dissociation occurs. (b) Silicon, lithium, and magnesium ion release was monitored via ICP-MS, revealing significant dissociation at pH 7.4 and 5.5 compared to pH 10 where nanosilicates remain stable.

3.3.2 Nanosilicate Dissociation Products Maintain hMSC viability

Previous studies investigating hMSC viability after nanosilicate treatment have demonstrated the ability of nanosilicates to sustain viability.(37, 201) however, nanosilicate degradation products (Li^+, Si^{4+}, Mg^{2+}) must also be investigated. Specifically, a broad range of silicon, lithium, and magnesium concentrations (0.001-10 mg/mL) were investigated to determine the effect of ions on cell viability and proliferation. Lithium and magnesium maintained 80% cell viability over a wide concentration range, up to 1 mg/mL, while silicon only maintained 80% cell viability at concentrations below 100 µg/mL (Figure 3-2a). Importantly, these viable concentrations were nearly 100-1000 times greater than those observed due to nanosilicate dissociation (4.49 µg/mL silicon, 0.067 µg/mL lithium, and 1.59 µg/mL magnesium) (Figure 3-1b). To investigate the effect of the individual ions within the nanosilicates on cell health, we treated hMSCs with the average release observed in ICP-MS: 30.54% (4.49 ± 1.98 µg/mL) silicon, 49.27% (0.067 ± 0.03 µg/mL) lithium, and 18.17% (1.59 ± 0.85 µg/mL) magnesium. While cells treated with nanosilicates were only treated once, the cells treated with individual ion solutions were replenished with those ion solutions every 3-4 days. Cell metabolic activity or viability after exposure to nanosilicates, individual ions, and the combination of ions was monitored via an Alamar Blue assay over 14 days (Figure 3-2b). No significant difference in viability was observed over time compared to the untreated control supporting nanosilicates and individual ions did not negatively affect hMSC health. These results support nanosilicate dissociation products can maintain cell viability as well as increase cell metabolic activity or proliferation over time.

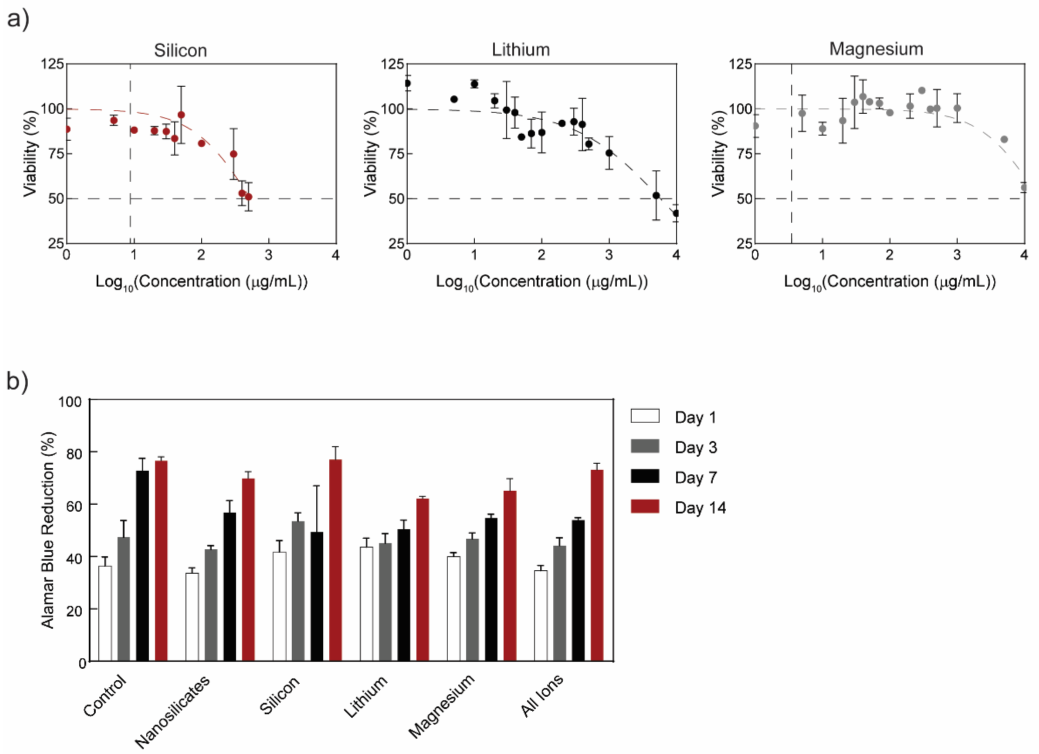

Figure 3-2 (a) hMSC viability at various mineral ion concentrations. Concentrations of released ions fall well below IC50 value. (b) Long-term hMSC viability after ion treatment assessed via Alamar blue assay.

3.3.3 Nanosilicate Dissociation Products Influence hMSC Osteogenic Differentiation

To investigate the effect of individual ions (Li^{+}, Si^{4+}, Mg^{2+}) on osteogenic differentiation of hMSCs, seeded cells were treated with the individual ions over 21 days. Ion concentrations were selected from ICP-MS data, in which 30.54% (3.49 ± 1.98 µg/mL) silicon, 49.27% (0.067 ± 0.03 µg/mL) lithium, and 18.17% (1.59 ± 0.85 µg/mL) magnesium were released after 21 days. Individual ions were replenished every 3-4 days with media changes. After 7 and 14 days, alkaline phosphatase (ALP)—an early marker for osteogenic differentiation—production was evaluated via surface staining and an assay (Figure 3-3a,b). After 7 days, treatment with nanosilicates, silicon, and the combination of ions resulted in nearly a two-fold increase in ALP production compared to the untreated control (***p-value<0.001). After 14 days, treatment with silicon resulted in similar ALP protein production to the nanosilicates. In addition, after 14 days of treatment, individual ions along with the combination ions resulted in significantly greater ALP production compared to the untreated control (****p*-value < 0.001) (Figure 3-3b). Likewise, matrix mineralization or calcium deposit was monitored after 21 days (Figure 3-3a). Quantification of mineralization revealed treatment with silicon (****p*-value < 0.001), the combination of ions (***p*-value < 0.01), and nanosilicates (**p*-value < 0.05) significantly increased matrix mineralization compared to the untreated control (Figure 3-3c). Similarly, silicon treatment resulted in significantly greater production of mineralization compared to lithium and magnesium treatment (****p*-value < 0.001).

In addition, osteo-specific protein production was monitored via western blot. Specifically, ALP, osteocalcin (OCN), and osteopontin (OPN), and collagen type I (COL1A1) expression were evaluated after 14 days (Figure 3-3c). Protein bands were quantified and the addition of silicon significantly increased OCN and OPN production compared to the untreated control nearly three-fold and ALP production nearly two-fold (Figure 3-3d). Similarly, nanosilicate treatment resulted in nearly two-fold protein expression of OPN and ALP and three-fold expression of OCN compared to untreated control. Alternatively, while magnesium increased OCN production nearly two-fold in comparison to the control, lithium and magnesium treatment resulted in limited expression of ALP and OPN. While COL1A1 protein expression after 14 days was not as distinct as other proteins, it is a later marker for osteogenic differentiation. However, treatment with nanosilicates and silicon did result in nearly 15-fold COL1A1 production compared to the untreated control as evidenced by the presence of protein bands and quantification.

While silicon on its own had a significant effect on hMSC differentiation, this could result from the high treatment concentration of silicon in comparison to the lower treatment concentrations of lithium and magnesium. In addition, these ion concentrations were added externally to the hMSCs compared to the release of ions from the nanosilicates that occurs in the endosome. The local concentration of released lithium and magnesium within the cell most likely has a greater effect than the external addition of the low concentration of lithium or magnesium. Overall, treatment with the combination of ions resulted in statistically similar ALP production and matrix mineralization compared to the nanosilicates. While osteo-specific protein production after treatment with the combination of ions has yet to be assessed via western blot, based on ALP production and matrix mineralization, similar protein production to nanosilicates and silicon is expected. Importantly, this evaluation of osteo-specific proteins and matrix production support that the chemical makeup of the nanosilicates and their subsequent release do play a pivotal role in the innate osteoinductivity of nanosilicates.

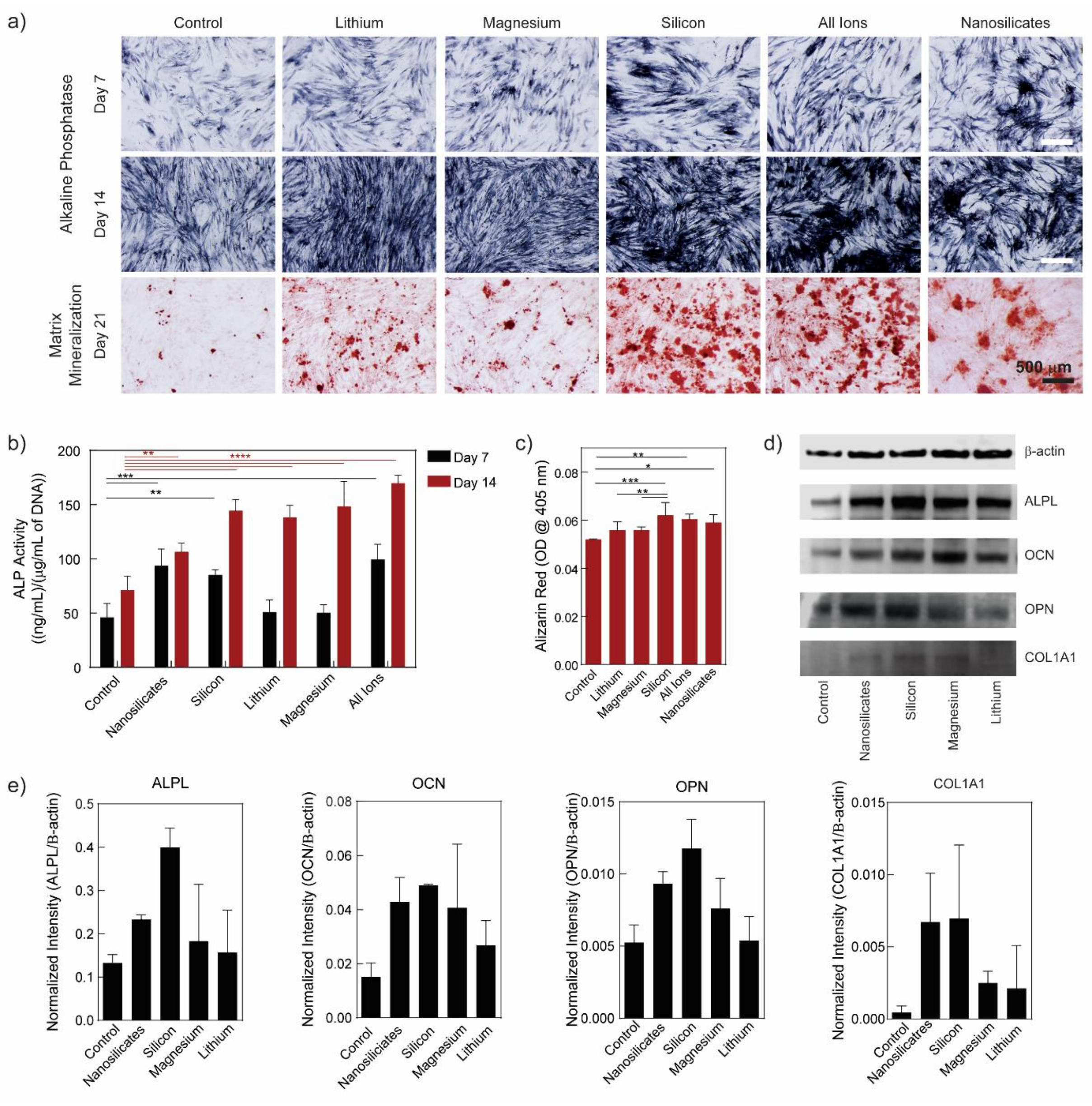

Figure 3-3 hMSC osteogenic differentiation. (a) ALP and matrix mineralization production after treatment with ions for 7, 14 and 21 days (Scale bar 500 μm). (b) ALP activity of individual ions compared to nanosilicates and all ions. (c) Quantification of mineralized matrix after 21 days. (d) Western blot of osteo-specific proteins after 14 days. (e) Quantification of protein expression from western blot normalized to β-actin expression. *P-value < 0.05**P-value < 0.01, ***P-value <0.001, ****P-value <0.0001

In addition, to evaluation of protein production after individual ion treatment, the effects of the individual minerals at the transcriptome level were also evaluated. Initially, gene expression was assessed after 14 days (Figure 3-4a). *ALP* gene expression was evaluated and a similar trend in gene fold change expression to protein expression was observed. Specifically, treatment with nanosilicates and the combination of ions resulted in similar fold changes of 3.12 and 2.82, respectively. Silicon, lithium, and magnesium also increased *ALP* expression 2.51, 2.49, and 1.84, fold-change, respectively. *COL1A1* gene expression was also evaluated, and similar to the observed protein expression, gene expression was low for all treatment groups. Specifically, the fold-change in *COL1A1* expression was ≤ 1.5 for all treatment groups. Although low, the presence of *COL1A1* gene expression is promising as it is the most abundant collagen in bone.

To further evaluate transcriptomic changes to hMSCs after treatment with individual ions and obtain a holistic view of these changes, whole-transcriptome sequencing (RNA-seq) was used. Preliminary evaluation revealed individual ions did not elicit as pronounced changes in gene expression as the nanosilicates, as evidenced by the heat map (Figure 3-4c); however, the genes that are significantly and differentially expressed will be further investigated and will help in pinpointing specific pathways affected. Further investigation of genetic targets of these individual ions will also aid in understanding mechanisms behind the innate osteoinductivity of nanosilicates. For example, from previous studies investigating the effects of lithium and silicon on osteogenic differentiation, activation of Wnt signaling was identified.(160, 163) With RNA-seq we expect to identify genes and subsequent pathways related to Wnt based on these previous studies. Importantly, information gathered from these individual ions can be used in future studies to design specific mineral-based nanomaterials for tissue regeneration strategies.

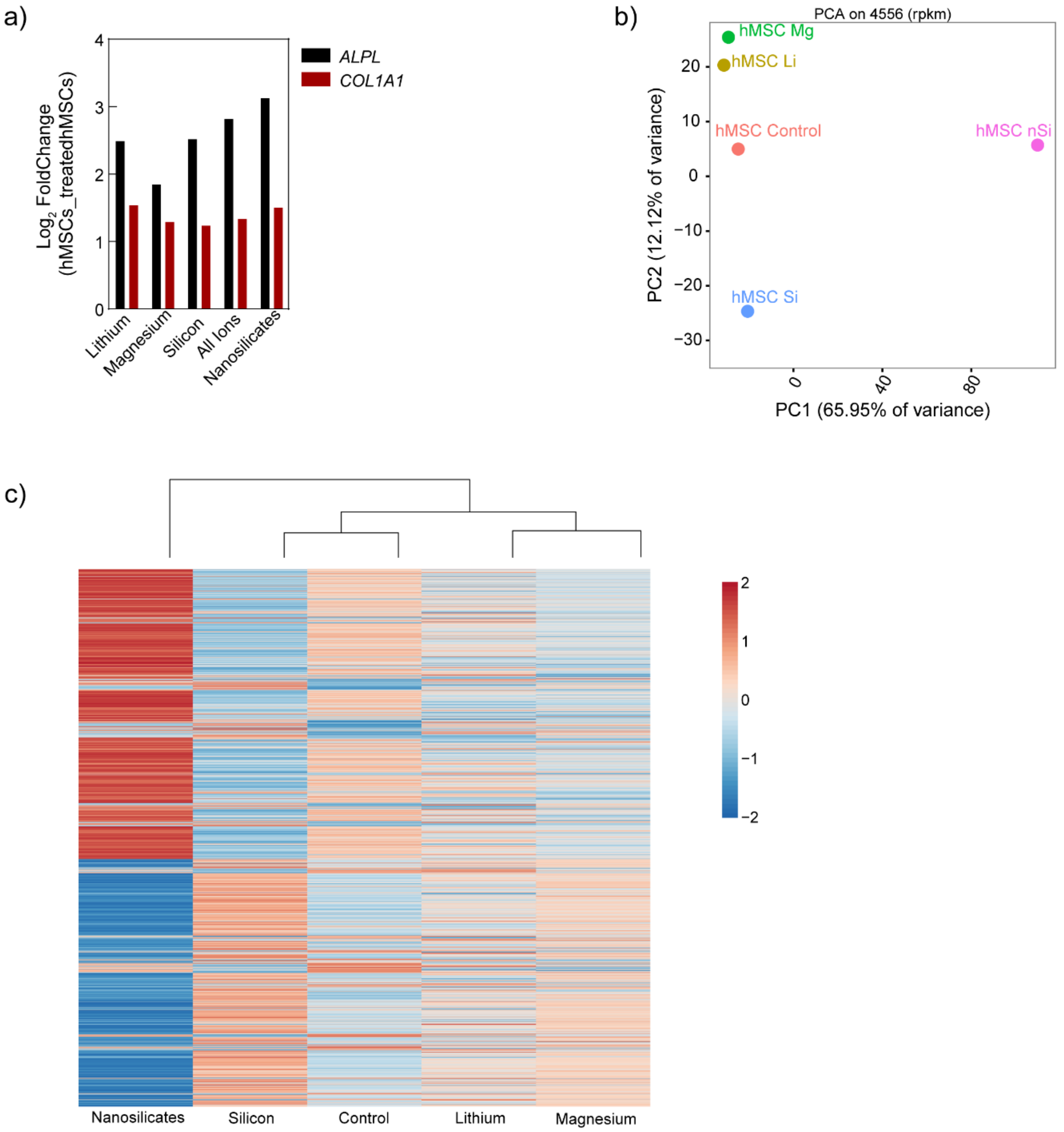

Figure 3-4 Comparison of genetic expression between different hMSC treatment groups. (a) Gene expression evaluated via qRT-PCR after 14 days, fold-change compared to untreated hMSCs. (b) Principal component analysis graph displaying genetic distance/relatedness across different ion and nanosilicate treatments. (c) Heat map visualizing genetic variation between different ion treated hMSCs compared to nanosilicate-treated hMSCs.

3.4 Conclusion

Nanosilicate dissociation into bioactive ions at physiological pH was identified and the treatment of hMSCs with the dissociation products (Li^+, Mg^{2+}, and Si^{4+}) stimulated osteogenic differentiation. While individual ions influenced hMSC osteogenic differentiation, the combination of the three ions elicited the greatest effect compared to the nanosilicates, supporting that the biochemical property of nanosilicates contributes to their innate osteoinductivity. Further investigation of hMSC responses to individual ions at the transcriptome level using RNA-seq will help further elucidate roles of these ions in modulating hMSC behavior and differentiation. Investigation of bioactive nanomaterials holds great promise for future tissue regeneration strategies as these materials have the potential to replace traditional bioactive cues. In addition, these investigations will aid in designing specific mineral-based nanomaterials in the future to target specific tissue regeneration applications.

4. LOCALIZED THERAPEUTIC DELIVERY FROM 2D NANOSILICATES DIRECTS DIFFERENTIATION OF HUMAN MESENCHYMAL STEM CELLS[*]

4.1 Introduction

Clinical strategies involve the administration of inductive molecules such as recombinant human bone morphogenetic protein 2 (rhBMP2) or transforming growth factor-beta3 (TGF-β_3) to enhance tissue formation.(207, 208) While successful regeneration has been observed, this is at the cost of supraphysiological doses of growth factor (1.5 mg/mL)(209), stemming from rapid clearance from the injury site and short half-lives of 7-16 minutes due to proteolysis *in vivo*.(210, 211) Furthermore, growth factors like, endogenous BMPs are typically found in the body at a concentration of less than 2 μg/mg.(212, 213) Recent clinical studies have demonstrated significant adverse effects following use of supraphysiological doses of including heterotopic tissue formation (spatially uncontrolled tissue formation), osteolysis, and inflammation.(214-216) These adverse effects are typically attributed to poor localization and rapid release of large amounts of growth factor.(217) Thus, there is a clinical need to develop an efficient biomolecule delivery vehicle that can result in sustained and prolonged release to reduce the effective dose towards physiological levels.

---

[*] Cross, L.M.; Carrow, J.K., Singh K.A.; Gaharwar A.K. “Sustained and Prolonged Delivery of Protein Therapeutics from 2D Nanosilicates to Direct Differentiation of Human Mesenchymal Stem Cells,” In Advanced Preparation.

Sustained release of low concentrations of growth factor molecules would minimize the side effects of excessive dosages.(217-219) Several strategies have emerged to reduce the dosage of growth factors, while maintaining therapeutic efficacy.(220-222) However, most of these approaches still incorporate relatively high dosages of growth factors (micrograms-milligrams), which can be costly. Here, we describe a nanosilicate-based platform to minimize the concentration of delivered therapeutic, while maintaining bioactivity and effectiveness. Nanosilicates ($Na^{+}_{0.7}[(Mg_{5.5}Li_{0.3})Si_8O_{20}(OH)_4]^{-0.7}$, Laponite® XLG), a two-dimensional (2D) nanomaterial, have been investigated for various biomedical applications including regenerative engineering and drug delivery.(38, 141, 223, 224) Our recent studies have demonstrated high cytocompatibility of nanosilicates with hMSCs.(138, 201) Nanosilicates readily attach to the cell membrane and are internalized by hMSCs *via* clathrin-mediated endocytosis.(184, 185, 225) In addition, nanosilicates have also shown to upregulate osteochondral-related genes and protein such as RUNX2, osteocalcin, aggrecan, and COMP, as well as production of mineralized matrix.(37, 139)

Along with their inherent bioactivity, the disk-shaped nanosilicates particles generate a permanent negative charge on each face (*via* the release of Na^+ in solution) and a positive charge along the edge (*via* the protonation of OH^- groups).(136, 202, 226) The dual charge of nanosilicates facilitates a wide range of possible interactions with proteins and therapeutics; importantly, these particles have previously been investigated for drug delivery applications.(223, 227-230) Specifically, cationic drugs can be immobilized by the exchangeable sodium cations of the nanosilicates.(223, 231) While these previous studies have demonstrated the ability of nanosilicates to electrostatically bind proteins or small molecules, the studies do not utilize or explore the inherent bioactivity of nanosilicates. Similarly, other studies have utilized nanosilicates for growth factor delivery; however, these studies use large concentrations of the nanosilicates and deliver the growth factors *via* a clay gel.(232, 233) No studies have investigated growth factor delivery via individual nanosilicates.

Here we demonstrate the ability of nanosilicates to prolong the release of physiologically relevant concentrations of rhBMP2 and TGF-β_3 and synergistically contribute towards osteogenic and chondrogenic differentiation of hMSCs, respectively. We will investigate the binding efficacy of protein to the nanosilicates, the time-dependent release of model protein from the nanosilicates, and we will also evaluate the osteochondral potential of the nanosilicate-rhBMP2 or TGF-β_3 co-delivery *via* osteochondral-related proteins and ECM production. Utilizing the nanosilicates as a delivery vehicle could be a potential therapy to augment the inherent bioactivity of nanosilicates. In addition, nanosilicate delivery of biomolecules could reduce overall costs by reducing growth factor concentration as well as minimize the negative side effects observed in use of supraphysiological dose of growth factors orthopedic regeneration strategies.

4.2 Materials and Methods

4.2.1 Nanosilicate Characterization

Nanosilicates (Laponite® XLG) were obtained from BYK additives. Atomic force microscopy (AFM), X-ray photoelectron spectroscopy (XPS), and attenuated total reflectance Fourier transform infrared spectroscopy (ATR-FTIR) were performed. Nanosilicate thickness was measured *via* AFM tapping mode (Bruker Dimension Icon Nanoscope), and analyzed with Nanoscope Analysis software. Nanosilicate chemical composition was analyzed via XPS

(Omicron XPS system with Argus detector), specifically analyzing oxygen (O *1s*), silicon (Si *2p*), magnesium (Mg *2s*, *2p*), lithium (Li *1s*), and sodium (Na *1s*) binding energies. ATR-FTIR was performed on nanosilicate powder with a Bruker vector-22 FTIR spectrophotometer (PIKE Technologies).

4.2.2 Protein-Nanosilicate Interactions

The hydrodynamic size and zeta potential of nanosilicate-protein (fetal bovine serum, Atlanta Biologicals) solutions were measured at 25°C using a Zetasizer Nano ZS (Malvern Instrument, U.K.) equipped with a He-Ne laser. Particle size was further investigated with transmission electron microscopy (TEM). The binding efficiency of nanosilicates to protein was determined using a model protein: fluorescein isothicyanate labelled bovine serum albumin (FITC/BSA, Sigma-Aldrich). 100 µg/mL of FITC/BSA was mixed for 1 hour with various concentrations of nanosilicates (0, 1, 10, 50, 100, 500, 1000 µg/mL) and then centrifuged to separate unbound protein. The supernatant was collected and measured using NanoDrop (495 nm excitation, 530 nm emission; NanoDrop 3300 Florospectrometer, Thermo Fisher Scientific) to determine binding efficiency.

4.2.3 *In vitro* Protein Release

The release profile of protein bound to nanosilicates was determined using a model protein bovine serum albumin (BSA, Sigma-Aldrich). Nanosilicate:BSA conjugates were made in phosphate buffered serum (PBS) and mixed for 1 hour to ensure binding. Samples were dialyzed (Float-A-Lyzer 100 kD MW, Spectrum) against PBS and samples were collected at various time points. The amount of released protein was quantified via a MicroBCA assay (Thermo Fisher) using standard protocol. 1-anilinonaphthalene-8-sulfonate (ANS) Assay was performed following previously described protocol.(234) Briefly, an ANS stock solution was prepared and filtered. The stock solution concentration was then determined via an absorbance reading at 350 nm and using an extinction coefficient of 50000 $(M/cm)^{-1}$. Protein samples were diluted and combined with ANS in a buffer of 10 mM Tris HCl, pH 7.4. Fluorescence from ANS was then measured in a plate reader at an excitation wavelength of 370 nm and an emission wavelength scan from 400-620 nm.

4.2.4 *In vitro* Osteogenic Differentiation

All *in vitro* experiments were performed with human mesenchymal stem cells (hMSCs) passage 5 or lower, obtained from Lonza. hMSCs were cultured in osteoconductive media (α-modified minimal essential media (αMEM, Hyclone), 16.5% fetal bovine serum (FBS, Atlanta Biological), and 1% penicillin/streptomycin (Gibco), supplemented with 10 mM β-glycerophosphate (Sigma-Aldrich) and 50 µM ascorbic acid (BDH Chemicals). The osteogenic differentiation potential of nanosilicate-recombinant human bone morphogenetic protein 2 (rhBMP2, EMD-Millipore) complexes was evaluated *in vitro* using hMSC 2D culture. hMSCs were seeded at a density of 4,000 cells/cm^2 in a 96-well plate and cultured in osteoconductive media for 7, 14, and 21 days. A negative control of untreated cells and a positive control of rhBMP2 (10 ng/mL) were used. Sample groups consisted of nanosilicates (100 µg/mL) and nanosilicate-rhBMP2 (100 µg/mL-10ng/mL). hMSCs were treated with nanosilicates and nanosilicate-rhBMP2 for 48 hours; hMSCs treated with exogenous rhBMP2 were treated with additional rhBMP2 every media change (every 3-4 days). To analyze osteogenic differentiation, conventional osteogenic assays were performed. Specifically, alkaline phosphatase (ALP) staining and kinetic assay, alizarin red staining and quantification of matrix mineralization, and immunostaining of osteo-specific protein osteocalcin.

Prior to staining, hMSCs were fixed with 2.5% glutaraldehyde for 15-20 minutes. ALP staining was performed at 7 and 14 days with NBT/BCIP 1-steps solution (Nitroblue tetrazolium/5-Bromo-4-chloro-3-indolyl phosphate, Thermo Fisher) for 30-60 minutes at room temperature. For ALP kinetic assay, cultures were incubated with alkaline phosphatase yellow (Sensolyte® pNPP ALP assay kit, AnaSpec). ALP activity as a function of pNPP metabolism (ΔOD405) was measured using automated plate reader and activity was normalized to DNA (picogreen, Thermo Fisher). Alizarin Red staining (ARS, Electron Microscopy Sciences) was performed after 14 and 21 days which binds to calcium; bound ARS is proportional to calcified matrix and was quantified by elution in acetic acid (10%), neutralized by ammonium hydroxide (10%), and spectrophotometrically measured by absorbance at 405 nm. ALP and ARS staining were visualized with stereomicroscope (Zeiss).

For immunostaining, hMSCs were fixed (10% formalin) then incubated in blocking solution (1% BSA in PBS) for 30 minutes. Samples were incubated with primary antibody for 1 hour at room temperature, then washed and incubated with secondary antibody for 1 hour. Samples were imaged with confocal microscope (Leika TCS SP5).

For Western Blot analysis, hMSC protein samples were isolated via a Laemmli buffer (10% 2-mercaptoethanol, 20% glycerol, 100 mM Tris HCl, 4% SDS, and 0.2% bromophenol blue). Protein samples were separated via gel electrophoresis (Mini Gel Tank; Invitrogen) and the gel was transferred (iBlot2; Invitrogen) to a nitrocellulose membrane. 5% BSA in PBST (0.1% Tween 20 in PBS) was used to block membranes for 30 minutes then processed to investigate specific proteins (iBind; Invitrogen). β-actin, ALP, osteocalcin (OCN), and osteopontin (OPN) primary antibodies (Thermo Fisher) and HRP conjugated secondary antibodies (Boster Bio) were used. After incubation with antibodies according to manufacturer's protocol, membranes were developed (SuperSignal West Pico PLUS Chemiluminescent Substrate; Thermo Fisher) and imaged with LI-COR 3600 CDigit Blot Scanner and bands were quantified via LI-COR software. Restoration and subsequent re-blocking were performed for additional protein analysis.

4.2.5 Spheroid Culture

For spheroid culture, hMSCs were cultured in basal media and collected no later than P4. Spheroids were created through centrifugation of cell suspensions to result in 10^6 cells per spheroid for GAG quantification and 2 x 10^6 cells per spheroid for histology. During centrifugation (500xg, 10 min), various treatments were added to media, specifically nanosilicates (50 µg/mL), (211) TGF-β_3(Boster Bio, 10 ng/mL), or a solution of premixed nanosilicates/TGF-β_3 at equivalent concentrations. Control cells received no external treatment. Media was replaced every 3-4 days. After 21 days of culture, spheroids were washed in PBS and fixed using 10% neutral buffered formalin for 2 hours. To quantify histological stains, images were processed with ImageJ software. Images were modified into an RGB greyscale stack. Color thresholding was applied equally over images within a stain cohort. Areas meeting color threshold were selected, quantified, and subsequently normalized to the total area of the spheroid. For the quantification of sulfated GAGs, a dimethylmethylene blue (DMMB, Sigma Aldrich) assay was utilized. Briefly, samples were collected at Day 3 and Day 21. Following washing with PBS, spheroids were enzymatically digested with papain at 60 °C overnight. The dye solution was created using DMMB (16 µg/mL), glycine (Alfa Aesar, 3.04 mg/mL), and

NaCl (2.37 mg/mL) dissolved in deionized water and maintained at pH 1.5 using 0.1M HCl. A standard curve was generated from chondroitin sulfate (Alfa Aesar).

4.2.6 Statistical Analysis

Plots are represented as mean and standard deviation and statistical analysis was performed using a one-way analysis of variance (ANOVA) with a Tukey's post-hoc with GraphPad Prism software. The statistical significance is presented as $*P\text{-value} < 0.05$, $**P\text{-value} < 0.01$, $***P\text{-value} < 0.001$, and $****P\text{-value} < 0.0001$.

4.3 Results and Discussion

Nanosilicates (Laponite XLG) are two-dimensional charged particles, approximately 1-2 nm thick and 25-30 nm in diameter (Figure 4-1a). The material properties of these nanosilicates have been extensively characterized in our previous papers.(201) Here, we investigated nanosilicate size distribution *via* transmission electron microscopy (TEM) and atomic force microscopy (AFM). TEM revealed uniform disk-shaped particles, and AFM images show that nanoparticle thickness was ~1.5 nm (Figure 4-1a,b). Surface characteristics of nanosilicates were also evaluated *via* ATR-FTIR, confirming the presence of O-Si-O stretching and bending around 1000 and 700 cm^{-1} , respectively (Figure 4-1c).(235, 236) Utilizing x-ray photoelectron spectroscopy (XPS), the presence of sodium, oxygen, silicon, magnesium, and lithium were identified, supporting chemical makeup of the nanosilicates ($Na^{+}_{0.7}[(Mg_{5.5}Li_{0.3})Si_8O_{20}(OH)_4]^{-0.7}$) (Figure 4-1d). In agreement with the empirical formula of nanosilicates, the XPS data supports oxygen as the most prevalent ion followed by silicon. As XPS and ATR-FTIR are surface techniques and the faces of the nanosilicates have larger surface area, this data also supports the presence of silicon and oxygen on the negative face of the nanosilicates. Additionally, the presence of O-Si-O bending and stretching on the surface, exposes the two-lone pair of electrons on each oxygen atom, contributing to the negative surface charge. Similarly, the positive edge of the nanosilicates stems from the protonation of OH^- groups. Importantly, the negatively charged faces and positively charged edges of the nanosilicates allow for a wide range of proteins to electrostatically bind or interact with the nanoparticles.

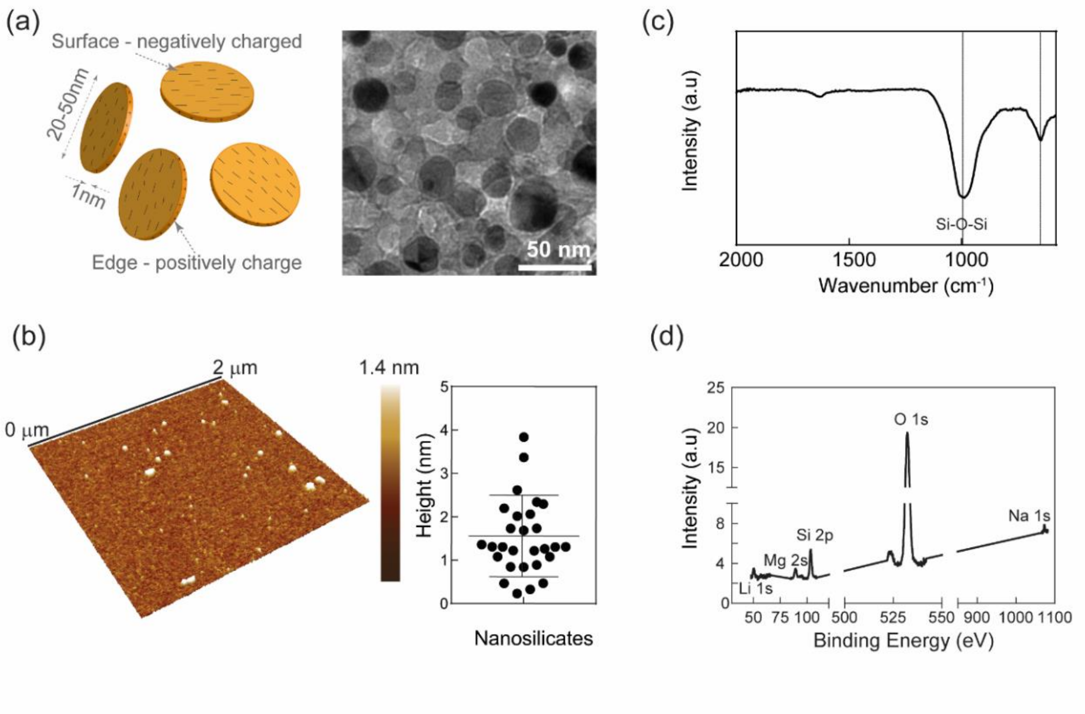

Figure 4-1 Physical characterization of nanosilicates. (a) TEM revealed size of two-dimensional nanosilicates. (b) AFM indicated the thickness of nanosilicates ~1-2 nm. (c) ATR-FTIR showed characteristic peaks at ~1000 and 700 nm representing Si-O bending and stretching, respectively. (d) XPS showed chemical composition of nanosilicates as shown by the binding energies for oxygen, silicon, magnesium, lithium, and sodium.

When nanosilicates are introduced into a physiological environment, their interactions with proteins result in the formation of a protein corona which directs nanoparticle-cell interactions.

The nanoparticle-protein complex can influence cellular transport as well as influence surface receptors and cellular pathways. (165, 237, 238) Therefore, these strong electrostatic interactions can be used to bind therapeutic growth factors and facilitate prolonged delivery. We previously determined (*via* whole-transcriptome sequencing) that nanosilicates trigger membrane targeting and can affect several signaling pathways related to growth factor stimulus and osteochondral-specific pathways.(201) Further gene ontological (GO) analysis has indicated that nanosilicate treatment of hMSCs results in the activation of "cellular response to growth factor stimulus," thereby conditioning the hMSC population for a growth factor treatment.(201) Based on this information, nanosilicates can be used to delivery therapeutics near the cell membrane or in the cytosol. For example, growth factors such as rhBMP2 or TGF-β_3 can be electrostatically bound to nanosilicates to enhance their inductive capability, thereby reducing the overall dose of growth factor. It is expected that the combination of growth factor with bioactive nanosilicates will allow for enhanced and synergistic osteogenic and chondrogenic differentiation in hMSCs.

4.3.1 Nanosilicates Strongly Interact with and Sequester Proteins

We investigated nanosilicate-protein interactions using fetal bovine serum (FBS). The dual charge of nanosilicates allows for a variety of electrostatic interactions or binding with serum proteins (Figure 4-2a). The size and charge of the resulting nanosilicate-FBS complexes were investigated, and TEM images revealed the presence of protein surrounding the nanosilicates in samples where FBS had been introduced. Further investigation with dynamic light scattering (DLS) confirmed this result; a significant increase in particle sized was observed in the nanosilicate-protein complex (~50 nm) compared to nanosilicates along (~28 nm) (Figure 4-2b). Similarly, unaltered nanosilicates exhibited a significant negative zeta potential (-38 ± 2 mV) compared to the nanosilicate-protein complexes formed in FBS (-23 ± 1 mV), indicating regions of the negatively charged faces were indeed coated with protein (Figure 4-2b). Importantly, while the complex's zeta potential shifted significantly compared to the nanosilicates, the value remained within the range of particle stability. A previous study investigated silica nanoparticle interactions with serum proteins and observed a similar shift in resulting particle size and zeta potential.(239) These results demonstrate that nanosilicates can strongly interact with proteins and/or therapeutic molecules.

4.3.2 Nanosilicates Strongly Bind and Release Proteins

Nanosilicate-protein binding efficacy and release kinetics were investigated using model proteins, specifically bovine serum albumin (BSA). Utilizing a fixed concentration of BSA labelled with fluorescein isothiocyanate (FITC/BSA, 100 µg/mL) and various concentrations of nanosilicates (0-1000 µg/mL) binding efficacy of the nanosilicates was examined. Approximately 100% binding was observed for a mass ratio of nanosilicates:FITC/BSA above 5:1 (Figure 4-2c). This indicates that the concentration of nanosilicates must be at least five times greater than the concentration of protein or therapeutic to attain the most efficient binding. Previous studies also support the ability of nanosilicates to bind proteins or small molecules. For example, one study demonstrated doxorubicin simply mixed with a nanosilicate suspension allowed for doxorubicin binding or encapsulation through ion exchange in the interlayered space of the dispersed nanosilicates.(228, 240) Interestingly, even non-ionic drugs such as dexamethasone have also recently been immobilized on nanosilicates.(223)

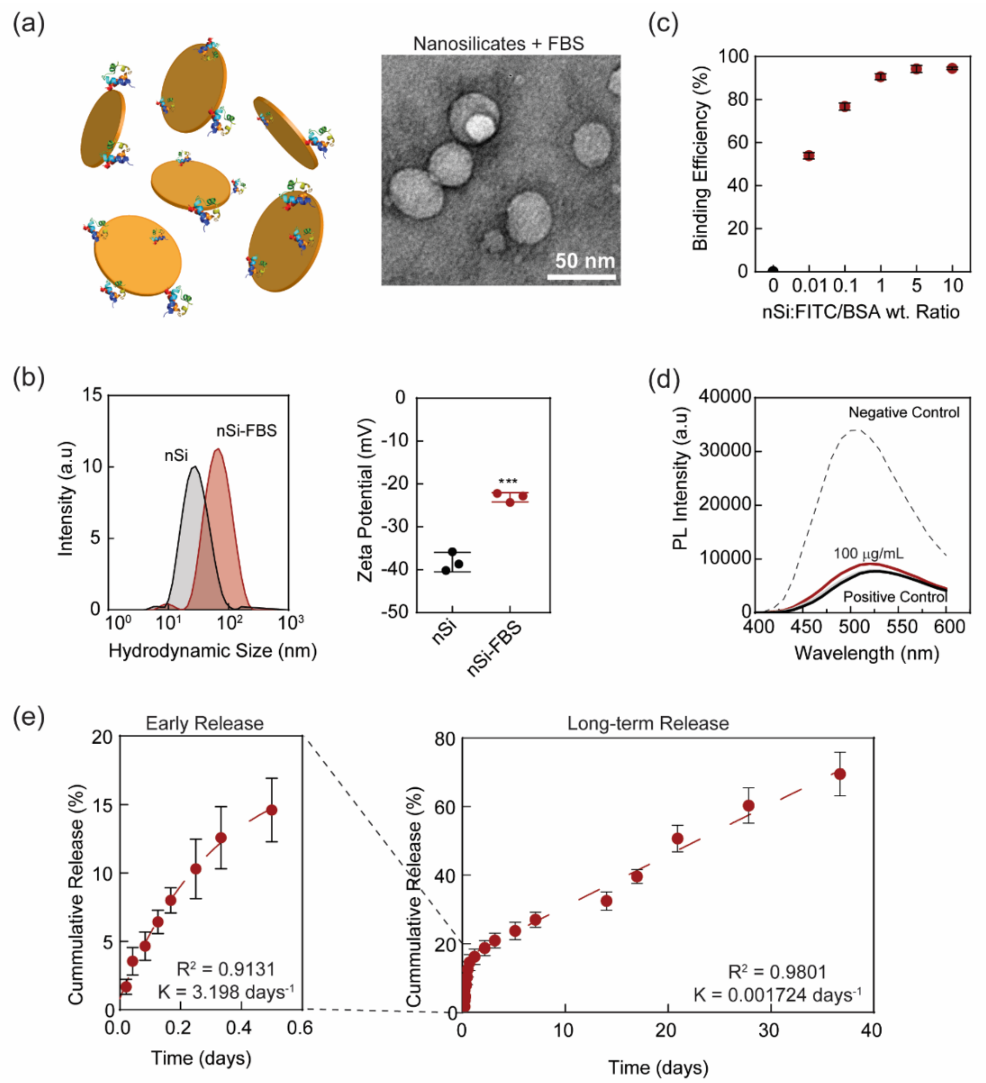

Figure 4-2 Nanosilicates strongly interact with proteins. (a) Schematic of protein interactions with nanosilicates. TEM images of nanosilicates in fetal bovine serum (FBS) solution. (b) DLS of nanosilicates (nSi) and nanosilicates with FBS (nSi-FBS) demonstrating shift in particle size with addition of protein solution. Zeta potential of nanosilicates and nanosilicates with FBS; once in contact with protein, particle charge shifts to be more positive (***P-value < 0.001). (c) Percent binding efficiency of nanosilicates to protein; nearly 100% binding observed at a ratio of nanosilicates to protein of 5:1. (d) ANS assay demonstrating no change in protein's secondary structure when bound to nanosilicates as indicated by minimal shift in fluorescent peak compared to completely denatured protein (positive control). (e) Early and long-term release of protein from nanosilicates. Protein release was monitored for over 30 days.

In addition to binding efficiency, the retained structure of the bound protein or therapeutic is essential as the protein corona of the nanoparticle will direct subsequent uptake or delivery.

Therefore, utilizing 1-anilinonaphthalene-8-sulfonate (ANS), we assessed changes in conformation of the bound protein.(241, 242) In this assay, the fluorescent dye binds to hydrophobic regions of the protein and so changes in fluorescence signal indicate a change in the exposed hydrophobic regions due to protein conformation change. No significant change in fluorescence was observed once protein was bound to nanosilicates compared to isolated protein. This indicated a minimal effect of nanosilicate binding on protein structure, suggesting that protein activity is retained (Figure 4-2d). Importantly, these results support previous studies that report negatively charged nanoparticles do not perturb protein structure.(237)

The release of protein from nanosilicates was monitored over a course of 30 days under physiological conditions. After an initial burst release of loosely bound protein within the first 12 hours, nanosilicates displayed sustained release of bound BSA (Figure 4-2e). The release kinetic was fit to a two-phase association model with an R^2 of 0.98, indicating a good fit for this release profile. The rate constant for long-term release was calculated as 0.001724 days^{-1}. This study supports our hypothesis that nanosilicates can be used as a vehicle for prolonged delivery of therapeutics. As 100% release was not observed, we believe that some protein may remain bound to the nanosilicates. In addition, released protein was analyzed via an ANS assay to investigate retained protein structure. Results indicated similar shifts in fluorescence compared to unmodified protein suggesting that the bioactivity of released protein was retained. These studies support the ability of nanosilicates to bind and release proteins while maintaining the protein structure.

4.3.3 Nanosilicate-rhBMP2 Delivery Promotes Production of Osteo-Related Proteins

The activity of released growth factor (rhBMP2) from nanosilicates was assessed using *in vitro* studies. Nanosilicates/rhBMP2 (100 µg/mL: 10 ng/mL) were subjected to seeded hMSCs and osteogenic differentiation was monitored over four weeks. We used untreated hMSCs, nanosilicates (100 µg/mL) treated hMSCs, and exogenous rhBMP2 treated hMSCs as controls. hMSCs treated with nanosilicate/rhBMP2 were treated for 48 hours, after which media was changed with osteoconductive media every 3-4 days, while exogenous rhBMP2 treated hMSCs were provided with fresh osteoconductive media containing rhBMP2 (10 ng/mL) every 3-4 days. After 7 and 14 days of culture, the production and activity of alkaline phosphatase (ALP, an early marker for osteogenic differentiation) was evaluated. Early on, an increase in alkaline phosphatase staining was observed in hMSCs treated with nanosilicate/rhMBP2 compared to hMSCs treated with exogenous rhBMP2 (Figure4-3a). ALP activity was also quantified and a significant increase in ALP production was observed in the nanosilicate, nanosilicate-rhBMP2, and exogenous rhBMP2 groups compared to untreated controls after 7 and 14 days of culture (Figure 4-3b). Similarly, ALP protein production was monitored via western blot after 14 days and an increase in protein bands were observed in the groups containing exogenous and nanosilicate/rhBMP2 (Figure 4-3c). Notably, the production of ALP in hMSCs treated once with nanosilicate/rhBMP2 (10 ng/mL) was comparable or greater than that of multiple treatments with exogenous rhBMP2 (20-40 ng/mL between 7 and 14 days).

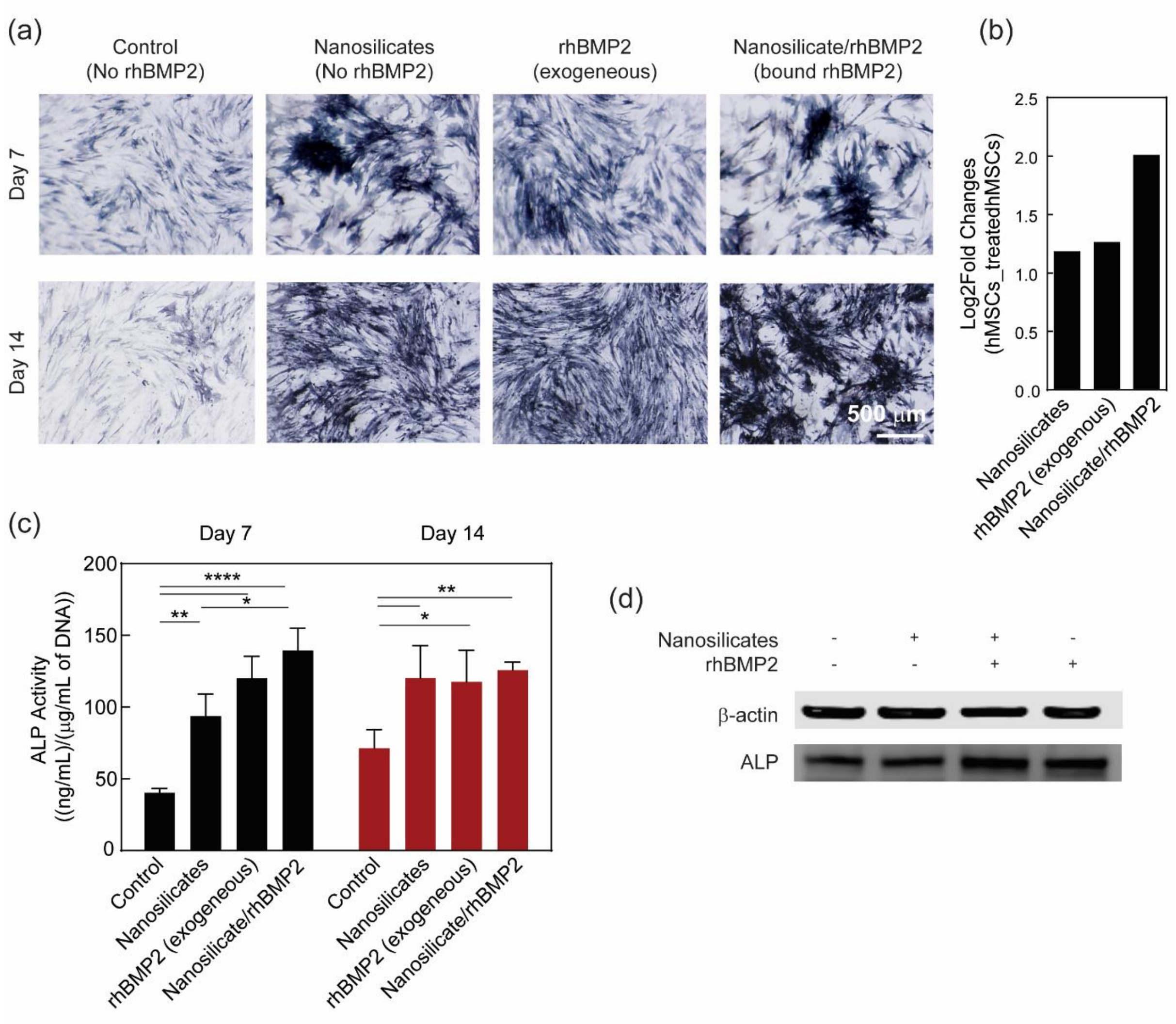

Figure 4-3 rhBMP2 bound to nanosilicates enhances alkaline phosphatase production. Nanosilicates and rhBMP2 bound to nanosilicates were delivered once while exogenous rhBMP2 was delivered every media change (every 3-4 days). (a) rhBMP2 bound to nanosilicates enhances alkaline phosphatase protein production compared to exogenous rhBMP2. (b) ALP activity after 7 and 14 days of culture. After 7 days, rhBMP2 delivery via nanosilicates increased production significantly (*P-value < 0.05, **P-value < 0.01, ****P-value < 0.0001. (c) Western blot of ALP after 14 days reveals an increase in protein production for groups treated with nanosilicate bound and exogenous rhBMP2.

In addition, the osteo-specific marker osteocalcin, one of the most abundant non-collagenous proteins in bone,(243) was evaluated *via* immunostaining and western blot analysis after 14 days of culture. Osteocalcin expression was greater in the hMSCs treated with nanosilicate/rhBMP2 compared to nanosilicates or rhBMP2 alone (Figure 4-4a,b). Further quantification of protein bands for osteocalcin revealed a significant increase in protein production for hMSCs treated with exogenous and nanosilicate/rhBMP2 compared to untreated control (Figure 4-4c). Osteopontin, which is important for biomineralization,(244) was expressed in all groups except the untreated control (Figure 4-4b). A distinct band for COL1A1 was observed in nanosilicate/rhBMP2 treated hMSCs (Figure 4-4d), compared to nanosilicate and exogenous rhBMP2 treated hMSCs. Further quantification of the band intensity supported the significant increase in COL1A1 production in the nanosilicate/rhBMP2 group compared to all other treatments. While previous studies have shown nanosilicates to increase COL1A1 production,(201) the significant increase in protein production with nanosilicate/rhBMP2 could have masked detection in the nanosilicate and exogenous rhBMP2 groups. Regardless, COL1A1 is very abundant in bone tissue so the increase in the protein production with treatment of both rhBMP2 and nanosilicates supports the synergistic contribution to enhance osteogenic differentiation of hMSCs.

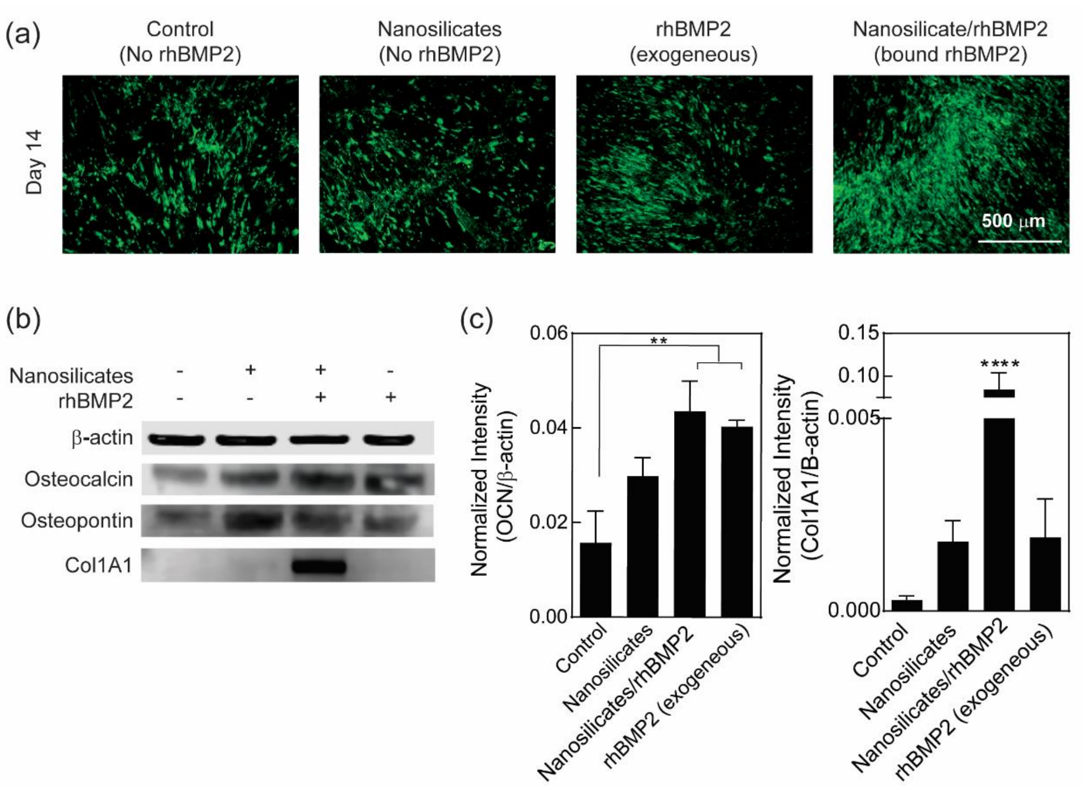

Figure 4-4 Sustained delivery of rhBMP2 promotes osteo-specific protein production. (a) Osteocalcin production enhanced by dual delivery of nanosilicates and growth factor after 14 days of culture. (b) Western blot of osteocalcin and osteopontin after 14 days revealed increase in protein production in all treatment groups compared to the control. In addition, collagen type I (Col1A1) production was increased in the nanosilicate/rhBMP2 treated hMSCs. (c) Quantification of osteocalcin showed a significant increase in exogenous and nanosilicate/rhBMP2 groups compared to the control (***P*-value < 0.01). In addition, quantification of intensity values for Col1A1 revealed a significant increase in protein production for nanosilicate/rhBMP2 (*****P*-value < 0.0001).

4.3.4 Nanosilicate-rhBMP2 Delivery Stimulates Mineralized ECM formation by hMSCs

Finally, the one-time delivery of nanosilicate/rhBMP2 significantly increased matrix mineralization or calcium deposit compared to multiple treatments of rhBMP2 alone. Alizarin Red staining revealed an increase in calcium deposit from 14 to 28 days (Figure 4-5a). After 14 days of culture, there was evidence of calcified matrix or bone nodules in the hMSC culture treated with nanosilicate/rhBMP2. Previous studies utilizing nanosilicates have also shown that these particles can facilitate nodule formation.(37) While increased staining for calcium deposit was observed in hMSCs treated with exogenous rhBMP2 at 21 and 28 days, these nodules were not present suggesting the dual delivery has a greater effect on osteogenic differentiation. Matrix mineralization at 14, 21, 28 days were quantified (Figure 4-5b). A significant increase in calcium production was observed in the nanosilicate/rhBMP2 groups across all days. At the later time points of 21 and 28 days, hMSCs treated with exogenous rhBMP2 also produced significant calcium deposit compared to control and nanosilicate treated groups.

The observed increase in osteo-specific markers and mineralized matrix production with the nanosilicate bound rhBMP2 not only supported retained rhBMP2 activity, but more importantly this dual delivery system induced synergistic and enhanced osteogenic differentiation. In addition, the dosage of rhBMP2 (10 ng/mL) delivered with the nanosilicates was significantly less than concentrations typically administered in *in vitro* studies; for example, previous studies have incorporated doses greater than 100 ng/mL.(220, 221, 232) While previous studies have utilized nanosilicates for delivery of growth factors, these studies have encapsulated growth factors within a nanosilicate gel or used the gel to sequester exogenous growth factor rather than binding them to the individual particles.(144, 232) Clay gels with encapsulated rhBMP2 displayed decreased bioactivity compared to groups with clay gels sequestering exogenous rhBMP2.(144, 232) In addition, the previous study merely seeded cells on top of fabricated gels, limiting cellular interactions with individual nanosilicates.(232) In the present study, nanosilicates with low dosage of rhBMP2 (10 ng/mL) were directly applied to hMSC culture; this allowed for hMSCs to interact with individual particles, and the delivery of rhBMP2 can be localized to the cell. Importantly, this dual delivery occurred only once during the study, as was only ~10% of the continual rhBMP2 treatment of the positive control. In reducing the concentration of rhBMP2, this dual delivery system provides an alternative and synergistic treatment for directing hMSC osteogenic differentiation and subsequently bone regeneration, minimizing both the cost and negative side effects associated with the typical high doses.

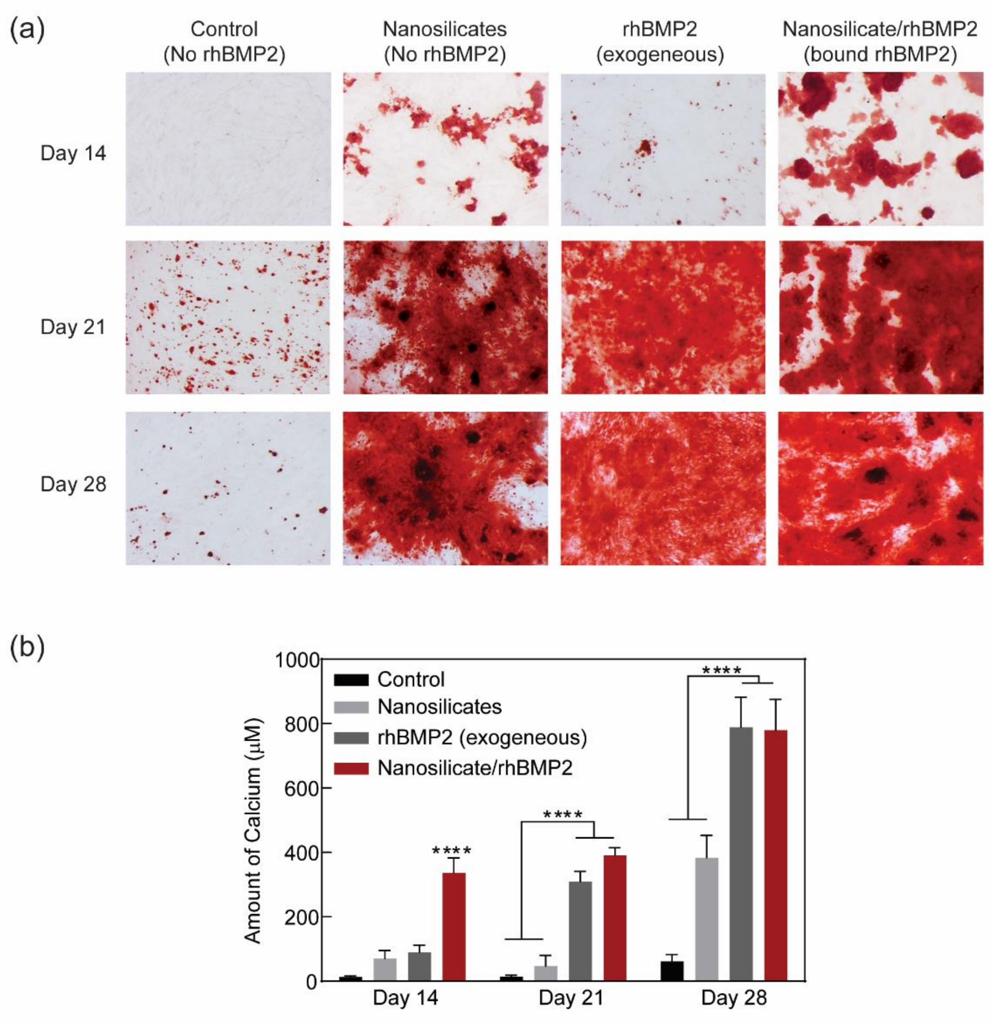

Figure 4-5 Sustained delivery of rhBMP2 from nanosilicates increases matrix mineralization. (a) Matrix mineralization or calcium deposit was significantly enhanced by dual delivery after 14 and 21 days compared to exogenous growth factor alone. Similarly, after 28 days, staining for mineralized matrix between exogenous rhBMP2 control and delivered rhBMP2 was comparable. (b) Quantification of calcium deposit after 14,21, and 28 days revealed a significant increase in deposit with the delivery of rhBMP2 via nanosilicates at all time points (*****P*-value < 0.0001).

4.3.5 Nanosilicates-TGF-β_3 Delivery Promotes Chondrogenic Differentiation of hMSCs

To investigate the ability of nanosilicates to deliver TGF-β_3 for chondrogenic differentiation of hMSCs, we modified the culture conditions of the hMSCs. Specifically, hMSCs were placed into three-dimensional (3D) spheroids to recapitulate the cell-cell interactions found in native cartilage (Figure 4-6a). Similar to the previous studies, cells were cultured in the absence of growth-factor unless specified otherwise. Over the course of one week, untreated hMSCs, hMSCs treated with nanosilicates, and hMSCs treated with exogenous TGF-β_3 displayed minimal differences regarding matrix synthesis with both sulfated glycosaminoglycans (GAGs, Alcian Blue) and collagens (Trichrome). Interestingly, the delivery of TGF-β_3 bound to nanosilicates appeared to improve chondrogenic behavior as early as seven days following spheroid formation. At later culture times (21 days), to indicate successful induction into a cartilage phenotype, histology was performed to monitor matrix component synthesis (Figure 4-6b,c). Alcian Blue stains indicated an increase in sulfated GAG production within the spheroid. Quantification of this staining through color thresholding in image software ImageJ revealed a significant increase in matrix production for spheroids with nanosilicate/TGF-β_3 delivery (Figure 4-6b). While continuous delivery of TGF-β_3 alone increased production of cartilage-specific matrix, the co-treatment of nanosilicates with TGF-β_3 provided the greatest stimulation towards the chondro phenotype at 10-fold lower concentration of TGF-β_3 (Figure 4-6c). This study support our previous work in which we demonstrated an increased cartilage-specific gene due to nanosilicate treatment alone.(201) From our previous work utilizing whole-transcriptome sequencing, we also observed that nanosilicates activated pathways related to TGF-β family proteins (e.g. response to transforming growth factor beta, GO:0071559), which further strengthen the current work.(201)

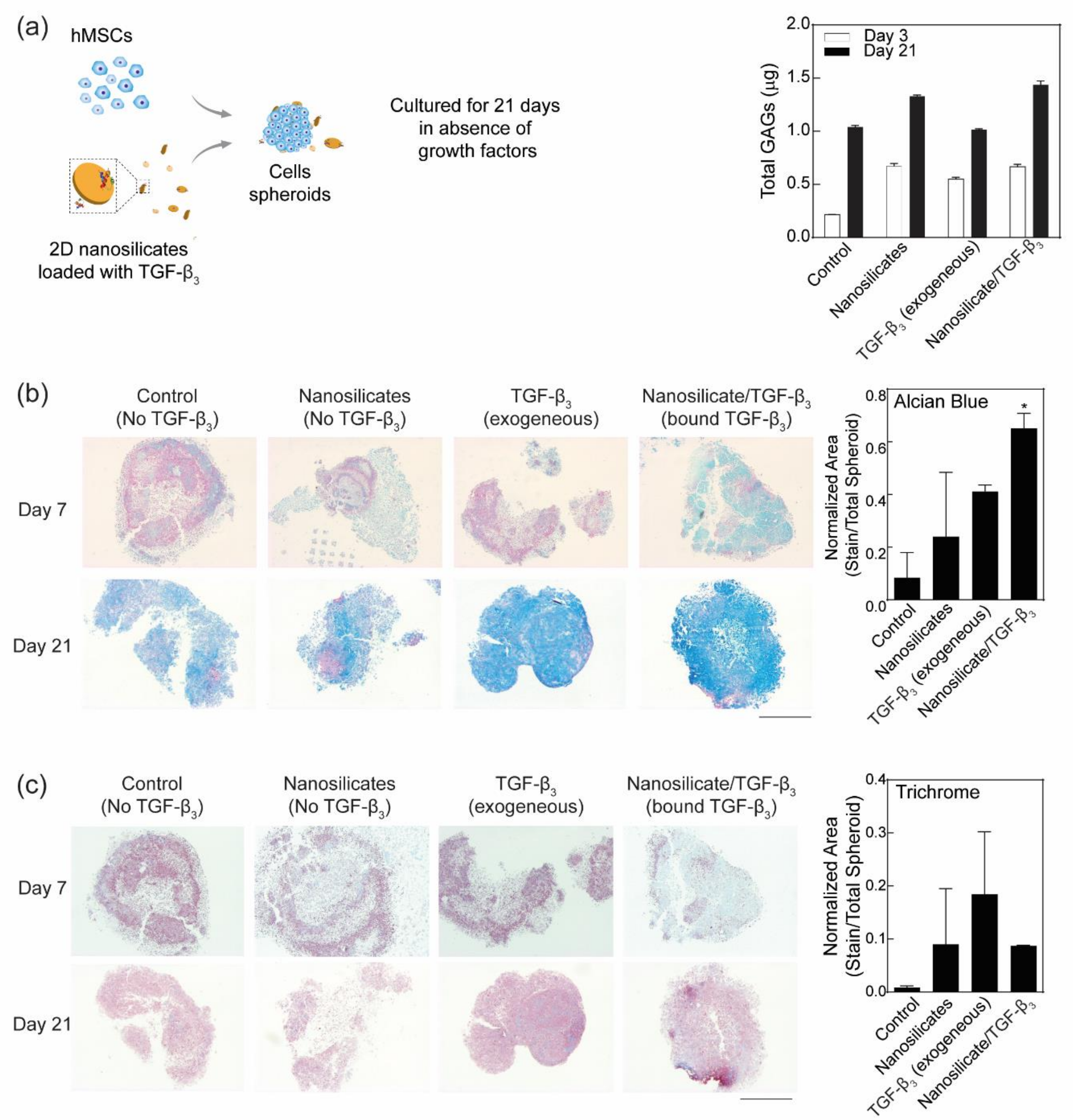

Figure 4- 6 Sustained delivery of TGF-β_3 from nanosilicates to hMSC spheroids. (a) Schematic of spheroid culture setup and delivery of TGF-β_3 via nanosilicates. Quantification of glycosaminoglycan production after 3 and 21 days. (b) Alcian blue staining after 7 and 21 days across treatment groups, an increase in staining or sulfated glycosaminoglycan production in samples treated with TGF-β_3 bound to nanosilicates (Scale bar 1 mm). (c) Trichrome stain for collagen after 7 and 21 days. (Scale bar 1mm).

Our nanosilicate/growth delivery system exhibits great promise for future orthopedic regeneration strategies. To assist in localization *in vitro*, the system could easily be incorporated into various tissue engineering constructs, including pre-fabricated scaffolds currently utilized to deliver therapeutics, like a collagen sponge or gel putty. Incorporation of nanosilicates with a collagen sponge of putty could prolong the delivery of entrapped growth factors and thus reduce the overall concentration. Moreover, nanosilicates can also be combined with a variety of natural and synthetic polymeric hydrogel systems including gelatin, kappa carrageenan, and poly(ethylene dioxide) for sustained and prolonged delivery of therapeutic proteins. These nanocomposite systems have been investigated for both injectable systems and 3D printed constructs.(41, 227, 245, 246) By localizing and patterning therapeutic protein, regionalized differentiation of stem cells on gradient scaffolds can be obtained to mimic the osteochondral interface.(246) Moreover, this technology can be extended to load-bearing applications by using in conjunction with an interbody fusion cage or by combining nanosilicates with biodegradable implants made from poly (propylene fumarate) or poly(L-lactic acid).

4.4 Conclusion

Our nanosilicate-based platform demonstrates the potential for superior orthopedic tissue engineering by reducing the required dose of growth factors. Due to the dual-charged and disc-shaped characteristics of nanosilicates, the particles can electrostatically bind and subsequently release therapeutic proteins such as rhBMP2 or TGF-β_3 over a prolonged duration. The nanosilicates also show high binding capabilities without altering the protein conformation. The released proteins were able to maintain high efficacy as demonstrated by *in vitro* experiments. Enhanced osteochondral differentiation in hMSCs at a lower concentration (10 ng/mL) was observed compared to exogenous control. Overall, this platform could be easily modified and applied to future biomedical applications requiring sustained therapeutic delivery for example orthopedic tissue engineering.

5. GRADIENT NANOCOMPOSITE HYDROGELS FOR INTERFACE TISSUE ENGINEERING[*]

5.1 Introduction

The bone-cartilage interface is composed of cartilage and subchondral bone, with a gradient in structural, physical and chemical properties.(247, 248) For diseases such as osteoarthritis, it is difficult to engineer these complex architectures using conventional fabrication technologies to facilitate regeneration of damaged tissues. The ability to mimic such interfaces, as well as to control the cell-matrix interactions at different locations, will be needed to develop new approaches. A range of designs such as layered or gradient structures are developed to mimic gradient in structure and mechanical properties.(21, 22) Additionally, the native tissue interface is composed of both micro- and nanostructures, making nanoengineered biomaterials an ideal scaffold material to mimic the native architecture.(249) A range of nanomaterials are incorporated within polymeric networks to improve the structural, mechanical, or biological properties of the scaffold. For example, spherical nanoparticles such as nanohydroxyapatite have been extensively investigated to mimic the bone-cartilage interface, as it enhances cell proliferation and scaffold mechanical properties.(33, 34, 79, 250)

---

[*] Reproduced with permission “Cross, L.M.; Shah K.; Palani S.; Peak, C.W.; Gaharwar A.K. Gradient Nanocomposites for Interface Tissue Engineering. *Nanomedicine:NBM*, DOI:10.1016/j.nano.2017.02.022” Copyright 2017 Elsevier.

Two dimensional (2D) nanomaterials have become a major focus in materials research in many applications, including biomedicine. Importantly, they possess the highest specific surface areas of all known materials, which is invaluable for applications requiring high levels of surface interactions on a small scale. Of these 2D nanomaterials, nanosilicates are uniquely suited for orthopedic tissue engineering due to their multiple functions such as ability to mechanically reinforce polymeric network, and potential to deliver therapeutic growth factors in a sustained manner.(41, 139, 251) Since nanosilicates are composed of complex polyions, they are able to interact within a hydrogel and form strong networks which in turn increase the mechanical properties.(41, 226, 252) In addition to enhanced mechanical properties, the structure of the nanosiliciates allow for increased shear-thinning and thixotropic properties when incorporated into polymer solutions.(253, 254) Specifically, nanosilicates independently form noncovalent bonds with multiple polymer strands, which can dynamically break and reform during loading, resulting in shear-thinning and thixotropic gels. (226, 254) The incorporation of these 2D nanoparticles could provide a facile approach in controlling physical and biological properties of the network.

As previously mentioned, most nanocomposite scaffolds for interface tissue are either layered or gradient designs.(21, 22) Layered or stratified scaffolds are the most commonly explored, as these designs often incorporate multiple materials and cell types to mimic the distinct tissue regions.(58) Although the layered scaffolds can account for the different layers of the tissue, i.e. the cartilage and subchondral bone, and possibly the interface region, they are susceptible to delamination because the layers are not necessarily connected. Alternatively, gradient scaffold designs can mimic the gradual change in the physical and mechanical properties that are present at the native tissue interface. In addition, these gradient scaffolds can offer a seamless transition between the two tissue regions and have the potential to mimic the natural structural and mechanical gradients.(249, 255)

Gradient scaffolds have been fabricated using a variety of materials such as hydrogels and nanofibers and fabrication methods including gradient makers, microfluidics, and electrospinning.(16) Electrospun, graded scaffolds have been investigated for the bone-cartilage interface; however, the fibrous structure does not ideally mimic the cartilage region.(46) Alternatively, hydrogel systems have been extensively studied for tissue regeneration due to their tunability and cell microenvironment mimicking capabilities and therefore are also ideal for gradient scaffolds.(256) Specifically for bone and cartilage tissues, previous studies have reported the use of natural material-based hydrogels to support regeneration. For example, gelatin methacrylamide (GelMA) has been investigated for bone regeneration, while methacrylated kappa carrageenan (MκCA) has been investigated for cartilage regeneration.(41, 250) Although microfluidic methods have been investigated for gradient formation with hydrogels, a simpler approach utilizing capillary flow was previously introduced which allowed for multi-layer gradient hydrogels to be fabricated.(257, 258)

Here, using 2D nanosilicates with two natural polymers, gelatin and kappa carrageenan (kCA), we developed a facile approach to fabricate a nanocomposite gradient hydrogel. Gradient hydrogels were fabricated using the natural material flow properties, which were enhanced by the addition of nanosilicates. A gradient in structure as well as mechanical properties was obtained. In addition, cell morphology was controlled along the scaffold. This simple and reproducible gradient hydrogel fabrication method could be applied to regeneration of tissue interfaces.

5.2 Methods

5.2.1 Polymer Solution Synthesis

Gelatin (type A, from porcine skin) and methacrylic anhydride (MA) were purchased from Sigma-Aldrich, USA. The synthetic nanosilicates (Laponite-XLG), were obtained from Southern Clay Product Inc, USA and the kappa-carrageenan was purchased from Tokyo Chemical Industry (TCI), USA. Gelatin methacrylamide (GelMA, 80% methacrylated) and methacrylated kappa-carrageenan (MκCA, 10% methacrylated) were synthesized using previously published methods.(41, 250, 251) Different prepolymer solutions were prepared in deionized water using GelMA (5 %wt/v) and MκCA (1 %wt/v) with varying concentrations of nanosilicates (0, 0.25, 0.5, 0.75 and 1.0 %wt/v). Photoinitiator (IRGACURE 2959, 0.25 %wt/v) was added to the prepolymer solutions. The pre-polymer solutions were prepared via vigorous agitation and heated at 37°C for 15 minutes and were fabricated via UV crosslinking (6.09 mW/cm^2, 60 seconds).

5.2.2 Rheology Testing

Rheological properties were characterized for gelation kinetics and shear stress sweeps using DHR-2 Rheometer (TA Instruments). Gelation kinetics of prepolymer solutions under UV irradiation was investigated using a 10 mm parallel plate geometry at a gap of 0.3mm. Oscillatory stress sweeps from 0.1 and 10 Pa at 1 Hz were carried out on all formed hydrogels. The change in viscosity of prepolymer solutions (5% wt/v GelMA and 1% wt/v MκCA, both with and without 0.5% wt/v nanosilicates) were investigated. Samples were pipetted onto a Peltier plate surface and allowed to rest before a 40 mm parallel plate geometry was used to vary the shear rate between 0.01-100 1/s.

5.2.3 Gradient Hydrogel Fabrication and Optimization

Gradient hydrogels were fabricated using machined Teflon molds (15.50 mm x 6.20 mm), containing three rectangular wells of dimensions 10x2x1 mm. Two different prepolymer solutions of equal volume were pipetted into the either side of the well simultaneously (Figure 5-1). Upon UV exposure (6.9 mW/cm^2, 60 secs), the prepolymer solutions were crosslinked to obtain a covalently crosslinked network. Prior to hydrogel formation, the prepolymer solutions were kept in the oven at 37°C. To form uniform gradients, the optimal volume of the prepolymer solutions, as well as the optimal time prior to crosslinking to allow for diffusion were determined. GelMA stained with Rhodamine B and MκCA prepolymers were used and the solutions remained at 37°C until pipetted into the well. For determining the optimal prepolymer volume, three different volumes were tested: 5μL, 10μL, and 15μL. Using the optimal volume, the optimal time prior to crosslinking was tested at 0, 5, and 10 minutes. At time 0, the solutions were added and the mold was immediately exposed to UV. For the other time points, the solutions were added and the mold was placed in the oven at 37°C for 5, or 10 minutes and then exposed to UV. Gradient uniformity was assessed using ImageJ Plot Profile.

5.2.4 Mechanical Testing

The compressive stress and modulus of the individual hydrogels were tested using MTESTQuattro (ADMENT, USA) with a 25 lb. transducer. The samples were placed in 1X PBS for 1 hour to swell prior to testing. Compression tests were performed and carried out to 50% strain. The compressive modulus was calculated based on the slope of the linear region from the stress-strain curve corresponding to 0-0.2 strain. For gradient hydrogels, compressive tests were performed using a 2 lb. transducer. To test different regions along the gel, an insert with a 1mm cone head was fabricated and prepolymer solutions of varying compositions were prepared (5% wt/v GelMA and 1% wt/v MκCA with and without nanosilicates). Six locations along the gradient were probed with the 1 mm tip geometry. A MATLAB program was developed to calculate the modulus. Statistical analysis was performed using GraphPad Prism.

5.3.5 SEM Characterization

To characterize the microstructure and porous nature of the gradient hydrogels, a scanning electron microscope (SEM) was used (JCM-5000: Benchtop SEM (Neoscope)). The gradient hydrogels were fabricated as previously described and then frozen using liquid nitrogen, freeze fractured, and lyophilized overnight. The dried samples were then mounted to expose their cross-section and sputter coated for 60 seconds at 20 mA with gold. The samples were then viewed with the SEM at an accelerating voltage of 10kV. Image analysis was done using ImageJ.

5.3.6 *In vitro* Cell Studies

Human mesenchymal stem cells (hMSCs) were cultured in normal growth media (AMEM, Hyclone), supplemented with 16.5% FBS (Atlanta Biologicals) and 1% penicillin/streptomycin (100U/100 µg/mL; Life Technologies, USA) at 37°C with 5% CO_2. Prior to cell encapsulation, four Teflon molds were sterilized with 70% ethanol for 15 minutes. Cells were trypsinized, neutralized with normal media, and then spun down at 1000 rpm for 5 minutes. Cell pellets were resuspended in 80µL of the four prepolymer solutions; there were approximately 100,000 cells in each solution. Prepolymer solutions were made in media rather than deionized water and stored at 37°C prior to cell resuspension. Prepolymer solutions containing resuspended cells were then pipetted into the Teflon molds and UV-crosslinked (6.9 mW/cm^2, 60 seconds). The molds were placed into a 24 well plate with normal media. For cell morphology studies at desired time points, the molds were washed twice with 1X PBS (Corning) and the samples were fixed using 500 µL of 2% glutaraldehyde (Sigma Aldrich) for 20 minutes. Samples were then washed with 1X PBS three times and 500 µL of 0.1% Triton X-100 in 1X PBS was added to permeabilize the cells for 5 minutes. Samples were washed with 1X PBS and gels were removed from Teflon molds for staining. 100 µL of phalloidin (1:100 dilution in 1%BSA/1XPBS) was added and samples were incubated at 37°C and protected from light for 1 hour. After 1 hour, the stain was removed and samples were washed three times with 1X PBS. 100 µL of Propidium Iodine/RNase solution (100 µg/mL RNASe and 500 nM-1.5 µM Propidium Iodine) was added, incubated at 37°C for 30 minutes, and then washed three times with 1X PBS. Cell images were taken using a confocal microscope (Leica TCS SP5) and images were analyzed with ImageJ.

5.2.7 Statistical Analysis

The data are plotted as mean and standard deviation. One-way analysis of variance (ANOVA) with Tukey’s post-hoc were performed using Graphpad Prism software. Statistical significance presented as * p-value<0.05, ** p-value< 0.01, *** p-value<0.001, ****p-value<0.0001.

5.3 Results

Here we have focused on designing a gradient scaffold for interface tissues as the interface contains a gradient in structural, mechanical, and biological properties. Although gradient scaffolds have been investigated previously(21, 22, 248, 249), the presented approach for gradient formation provides a simple and reproducible method that could easily be modified. Previous methods for osteochondral scaffolds have targeted properties such as graded pore size, chemical composition, stiffness, or growth factors.(34, 46, 259, 260) Despite the formation of a gradient to match the gradual change in native tissue, some of these methods can require intensive materials preparation or equipment and only provide a gradual change in one property. In addition, other gradient fabrication methods involve complex microfluidic strategies.(261, 262) The presented method is simple and with two natural polymers and the inclusion of nanosilicates in the hydrogel network, we are able to vary the structural, mechanical, and biological properties of the material.

5.3.1 Nanoengineered Gradient Hydrogels

Gelatin and κ-carrageenan were ideal polymers for the osteochondral scaffold because of the two have been investigated for bone and cartilage scaffolds individually.(41, 250) Gelatin contains RGD binding domains which allow for cells to adhere and spread typical of osteoblasts in bone; while, kappa carrageenan is a polysaccharide resembling native glycosaminoglycans with limited binding sites, and cells will exhibit a more rounded morphology indicative of chondrocytes in cartilage.(263, 264) In addition, previous studies have demonstrated the mixing capabilities of gelatin and κ-carrageenan in a solution, supporting the mixing of the two solutions in the present gradient hydrogel formation.(265) In the present study, these polymers were successfully modified with methacrylic anhydride to allow for uniform photopolymerization and hydrogel formation. Nanosilicates were incorporated in the two solutions, as previous studies(41, 250) have supported increased shear-thinning and therefore increased flow properties as well as their ability to enhance the structural properties of a material. Specifically for gelatin, as a polyampholytic natural polymer containing both negative and positive regions, it strongly interacts with the opposite charged surfaces of the nanosilicates.(266) In addition, previous gradient constructs, specifically for osteochondral regeneration, have not incorporated nanomaterials into both regions of the scaffold for increased mechanical stability. Finally, human mesenchymal stem cells (hMSCs) were encapsulated within the hydrogel matrix to demonstrate the ability to control cell morphology along the gradient (Figure 5-1). Here, gradient hydrogels were successfully fabricated using a facile and reproducible method of pipetting two prepolymer solutions into a Teflon mold at the same time and allowing capillary action to form uniform distributions. Although previous studies have demonstrated the ability to form multi-layer gradient hydrogels using capillary flow, here with simple modification, we produced a single but connected layer exhibiting a seamless transition from one material to the next. In addition, the Teflon mold allowed for three hydrogels to be prepared at once for easy replication and the mold fit within a 24-well plate for simple *in vitro* studies.

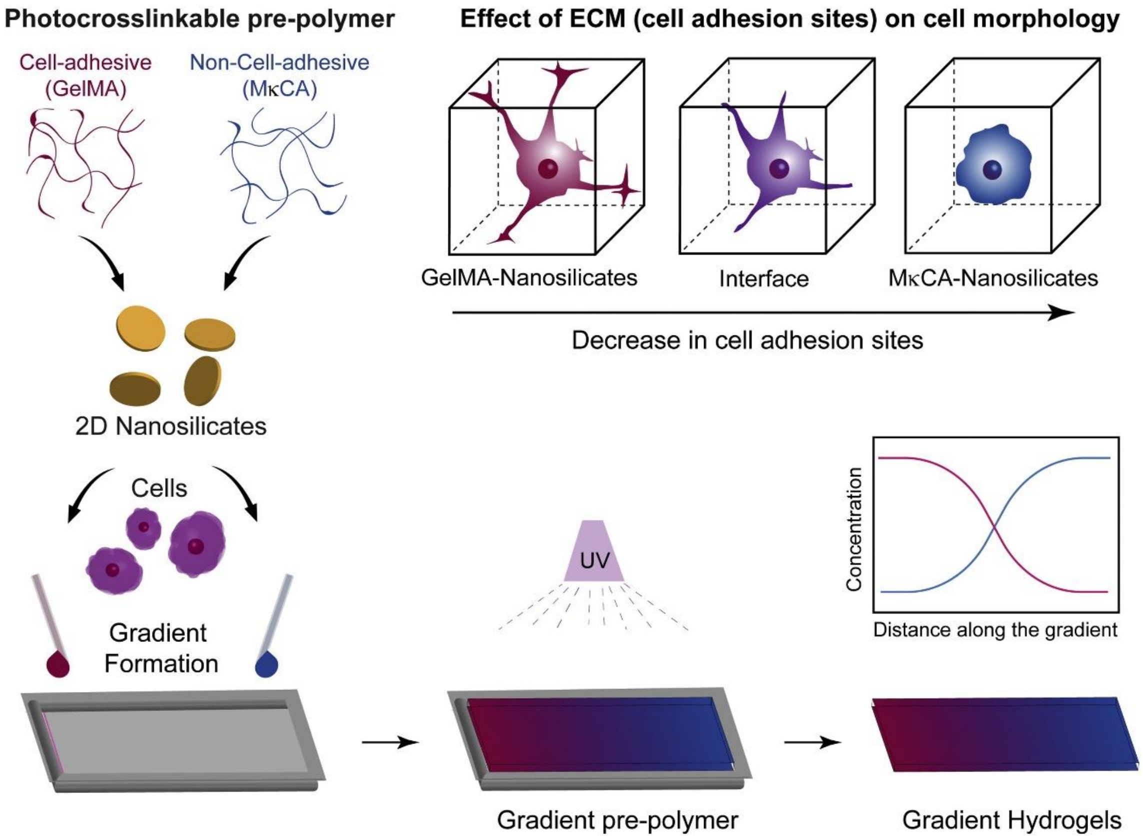

Figure 5-1 Nanoengineered gradient scaffolds loaded with 2D nanosilicates. Schematic showing formation of gradient hydrogel from GelMA and MκCA prepolymers reinforced with nanosilicates (nSi). Cells can be encapsulated during the formation of gradient scaffold. The gradient structure is subjected to UV light to obtain fully crosslinked scaffold. The GelMA contains cell binding sites which allow for cell spreading, whereas the MκCA does not and cells are expected to retain round morphology.

5.3.2 Nanosilicate Reinforces Polymeric Network

Prior to gradient hydrogel formation, the optimum concentration of nanosilicates within the 5.0% wt/v GelMA and 1.0% wt/v MκCA hydrogels for improved mechanical properties was determined through compressive mechanical tests (Figure 5-2). The concentrations of 5.0% wt/v GelMA and 1.0% wt/v MκCA were chosen based on previous studies.(41, 250) The addition of the nanosilicates significantly increased the compressive moduli and strength of the gelatin and κ-carrageenan based hydrogels (Figure 5-2a,b). At 50% compression, the strength of the GelMA hydrogels increased up to seven-fold with the addition of 1% wt/v nanosilicates, while the strength of the MκCA hydrogels increased nearly three-fold at the same concentration. Similarly, with 0.5% wt/v nanosilicates, the strength of GelMA hydrogels increased three-fold while MκCA hydrogels increased two-fold. It was determined that the addition of 0.5% wt/v nanosilicates was the optimal concentration since it provided a significant increase in the MκCA hydrogels' compressive moduli (2.4±0.3 kPa to 3.4±0.5 kPa) without increasing the mechanical properties so much that it would mimic the GelMA hydrogels' mechanical properties too closely (Figure 5-2b). In addition, rather than incorporating another variable to the study, 0.5%wt/v nanosilicates was chosen for the GelMA region as well. Although the addition of 0.5%wt/v nanosilicates was not statistically different from GelMA hydrogels without nanosilicates, the modulus was still increased two-fold (from 3.5±0.6 kPa to 5.9±1.8 kPa).

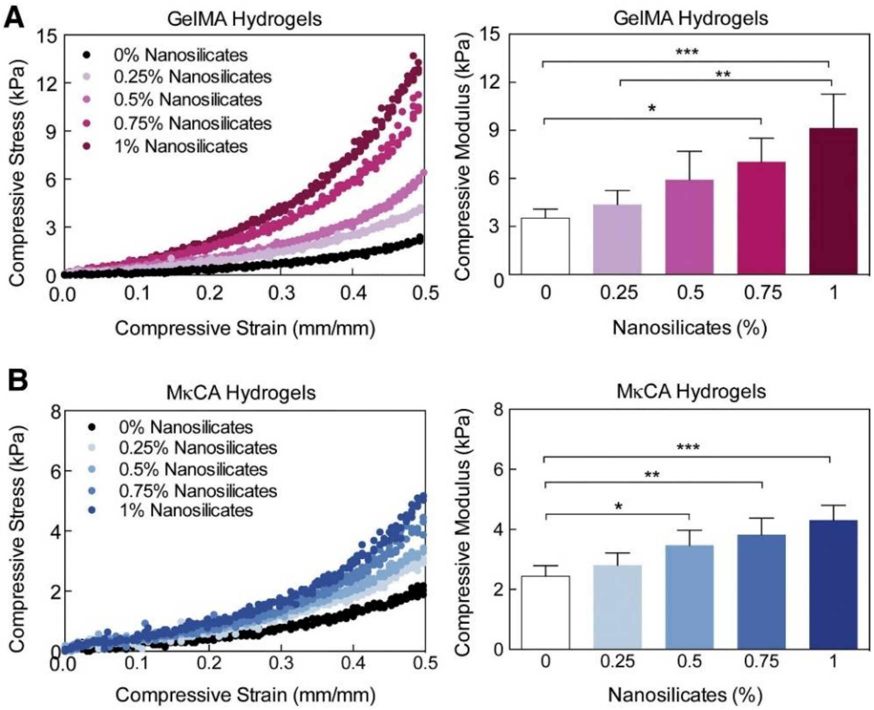

Figure 5-2 Nanosilicates reinforce the polymeric hydrogels. Uniaxial compression test shows that addition of nanosilicates to (A) GelMA and (B) MκCA hydrogel results in an increase in compressive modulus. (Statistical analysis: One-way ANOVA with Tukey’s post-hoc analysis, **P*-value < 0.05, ***P*-value < 0.01, ****P*-value < 0.001).

5.3.3 Nanosilicates Modulate Flow Properties and Rheological Characteristics

With these optimal concentrations, the flow properties of the prepolymer solutions were investigated to evaluate flow once pipetted into the molds. To investigate the effect of nanosilicates on the shear-thinning behavior of prepolymer solutions, the viscosity at different shear rates (0.01-100 1/s) was monitored (Figure 5-3a). The viscosity decreased with increasing shear rate for all prepolymer compositions suggesting shear-thinning behavior; however, depending on the backbone chemistry and the inclusion of nanosilicates, viscosity can be modulated. Addition of 0.5% wt/v nanosilicates generally causes a solution to have an increase in its shear-thinning ability due to the orientation of the nanoparticle under applied shear.(226, 254) Here, nanosilicates increased the shear-thinning behavior of the prepolymer solutions. Although MκCA nSi was observed to have the highest viscosity, the solution still flowed through the mold.

The gelation kinetics as well as the structural stability of hydrogels at these final concentrations were also investigated (Figure 5-3b). Methacrylate functional groups on both gelatin and kappa carrageenan permitted covalent crosslinking through UV-initiated free radical polymerization. The addition of nanosilicates did not affect the gelation time of either the GelMA or MκCA hydrogels as indicated by the similar plateaus of the storage modulus; however, the storage modulus was increased by nearly two-fold in the GelMA hydrogels with the addition of the nanosilicates, supporting the increase in mechanical properties seen in compression testing. The rheological data support the results observed in compressive tests, and indicate that only a small percentage of nanosilicates can be incorporated to significantly enhance the mechanical properties of the individual hydrogels.

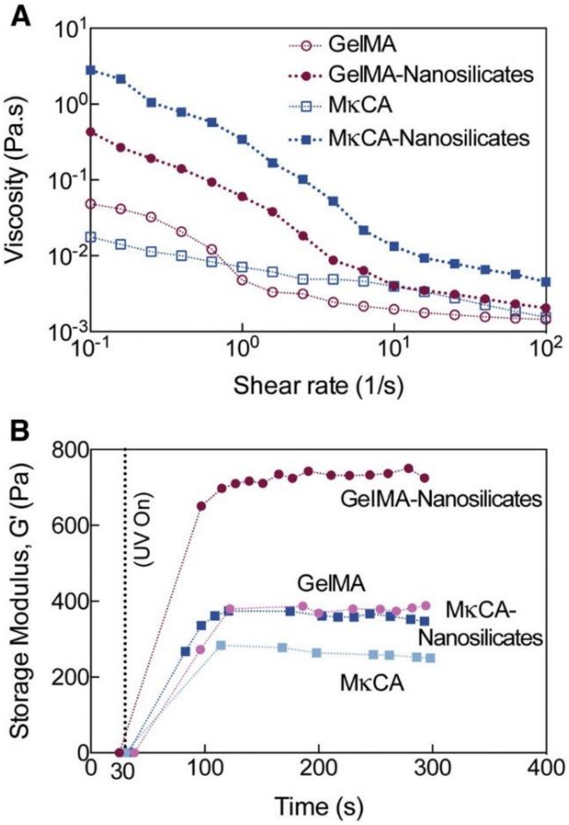

Figure 5-3 Nanosilicates modulate flow and rheological properties of prepolymer solution. (A) The addition of 0.5 % wt/v nSi allowed the GelMA and MκCA prepolymer solutions to exhibit shear-thinning behavior, a decrease in viscosity with increasing shear-rate. (B) UV gelation kinetics reveals an increase in storage modulus with no increase in gelation time with incorporation of 0.5% wt/v nSi in either GelMA or MκCA.

5.3.4 Optimizing Gradient Hydrogels

Once the flow properties were determined, the optimal volume to allow each solution to flow towards the middle of the channel as well as the optimal time to allow for uniform distribution of solutions were determined (Figure 5-4a). Of the three volumes tested, 10 µL of each solution enabled equal flow to the middle. In addition, 5 µL of each solution was too small of a volume to reach the center, while 15 µL nearly overflowed the channel. This even flow was confirmed with the ImageJ Plot Profile in which 10 µL had the most uniform distribution. The Plot Profile tool provided the pixel density along the distance of the gradient; with increasing distance the pixel intensity displayed a sigmoid curve. Using this optimal volume, the ideal time prior to crosslinking was observed to be 5 minutes, which allowed for uniform distribution of both solutions. Although immediate crosslinking after administration allowed for some flow between solutions, quantification with ImageJ revealed a more uniform distribution after 5 minutes (Figure 5-4b). With these optimal parameters, nanocomposite gradient hydrogels were successfully fabricated.

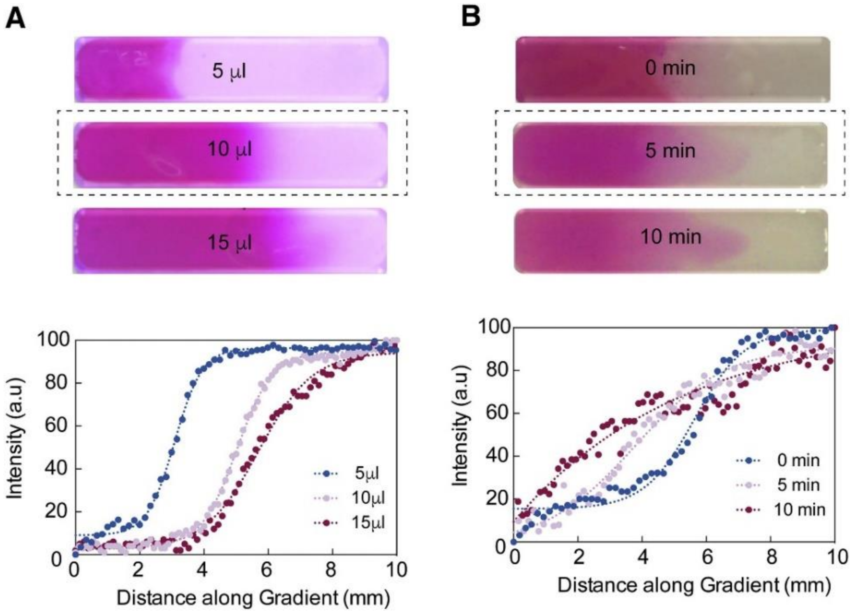

Figure 5-4 Fabrication of gradient hydrogels. (A) Optimization of solution volume to form uniform gradients revealed 10 µL of each solution allowed for immediate mixing (top). ImageJ quantification supported this observation (bottom). (B) Optimal time for uniform mixing of solutions once pipetted was observed to be 5 minutes (top). Similarly, quantification in ImageJ revealed the most uniform curve (bottom).

5.3.5 Gradient in Structural and Mechanical Properties of Hydrogels

Characterization of the structural and mechanical properties of the gradient hydrogels with and without nanosilicates was performed (Figure 5-5). The gradient microstructure was observed using

SEM and a distinct change in mesh area was noted when shifting from the GelMA region (4.0 ± 2.7 μm^2) to the interface region (16.9 ± 14.4 μm^2) and then to the MκCA region (75.3 ± 49.0 μm^2) of the scaffold (Figure 5-5a**)**. With the addition of nanosilicates, an increase in mesh area shifting from the GelMA-nSi region to the MκCA-nSi region was also observed (Figure 5-5b). Previous studies have reported an increase in mesh size in GelMA hydrogels due to interactions of the nanosilicates with the gelatin backbone, supporting the increase observed in this study.(41) Alternatively, mesh size was previously observed to decrease with the addition of nanosilicates in MκCA hydrogels.(250) This discrepancy could result from changes in MκCA and nanosilicate concentrations; the concentrations used in this study are smaller than those used in the previous study and therefore could affect the way the materials interact together. At the interface regions, a range of mesh sizes exists which leads to high standard deviations but demonstrates the integration of the two natural polymers.

To characterize the mechanical properties of gradient structures, compression tests were performed using a 1mm cone geometry that allowed for different regions along the scaffold to be probed (Figure 5-5a,b). For all hydrogels, a total of six regions along the gel were tested. For both gradients, a decrease in the compression modulus was observed when shifting from the GelMA regions to the MκCA regions, supporting previously observed compressive moduli values for individual hydrogels. Specifically, in the hydrogels without nanosilicates, the moduli shifted from 6.7±0.4 kPa in the GelMA region to 1.8±0.4 kPa in the MκCA region. When nanosilicates were incorporated, the moduli decreased from 7.5±1.7 kPa in the GelMA nSi region to 3.6±1.8 kPa in the MκCA nSi region. Prior to performing compression tests on the gradient scaffolds, the new

1mm cone geometry was validated by testing GelMA hydrogels and resulting moduli values were compared to published results.(41)

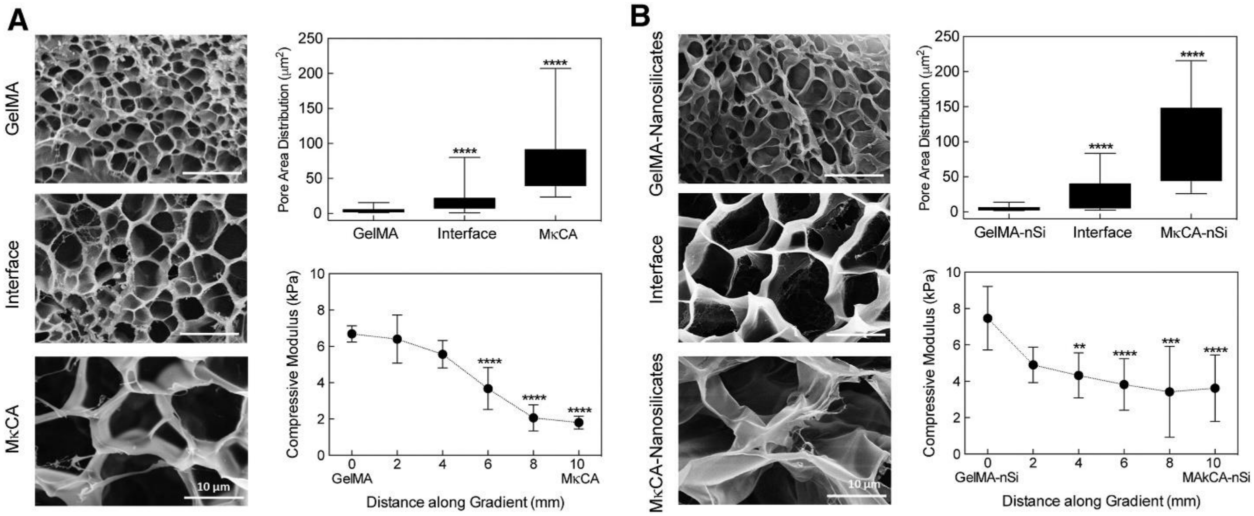

Figure 5-5 Gradient in microstructure and mechanical stiffness of scaffold. (A) Scanning electron micrographs of gradient hydrogels (GelMA- MκCA). A significant increase in mesh size was observed at the interface and MκCA regions, compared to the GelMA region. Compression testing of gradient hydrogels revealed a gradual decrease in compression moduli when shifting from GelMA region to MκCA region. (B) The addition of nanosilicates increased the overall gradient hydrogel mesh size with a significant increase in the interface and MκCA nSi regions compared to the GelMA nSi region. Similarly, mechanical testing revealed a gradual decrease in compressive moduli but the inclusion of nSi increased the overall compressive moduli two-fold (Statistical analysis: One-way ANOVA with Tukey's post-hoc analysis, $*P$-value < 0.05, $**P$-value < 0.01, $***P$-value < 0.001).

5.3.6 hMSC Encapsulation Exhibits Gradient in Cell Morphology

The cellular response at different regions of the gradient hydrogels was investigated through 3D encapsulation of human mesenchymal stem cells (hMSCs) (Figure 5-6a). hMSCs were successfully encapsulated within the hydrogel networks and imaged after one and three days. After one day, cells remained round in all regions of both gradient scaffolds. However, after three days of encapsulation, a distinct change in cell morphology was observed based on the location within the gradient. In the GelMA and GelMA-nSi regions, cells were spread out characteristic of osteoblasts in bone, while the MκCA and MκCA-nSi regions, cells exhibited a round morphology characteristic of chondrocytes in cartilage.(267) At the interface regions, both cell morphologies were present, indicating a smooth transition from one region to the next (Figure 5-6b). These results reinforce previous studies that suggest GelMA and MκCA to support bone and cartilage regeneration respectively.(41, 250)

Average cell circularity and cell area along the scaffold were calculated using ImageJ to quantify these changes in cell morphology (Figure 5-6c,d). Circularity (a.u) ranged from 0-1, in which 1 represented a perfect circle. In the GelMA region, the average cell circularity was found to be 0.4 ± 0.2 while in the MκCA region this increased significantly to 0.8 ± 0.1. At the interface, the average cell circularity was 0.5 ± 0.3, in between the average for the two extreme regions of the scaffold. With the addition of nanosilicates, the average cell circularity was not significantly affected; however, a similar trend in cell circularity was observed from the GelMA nSi region to the MκCA nSi region.

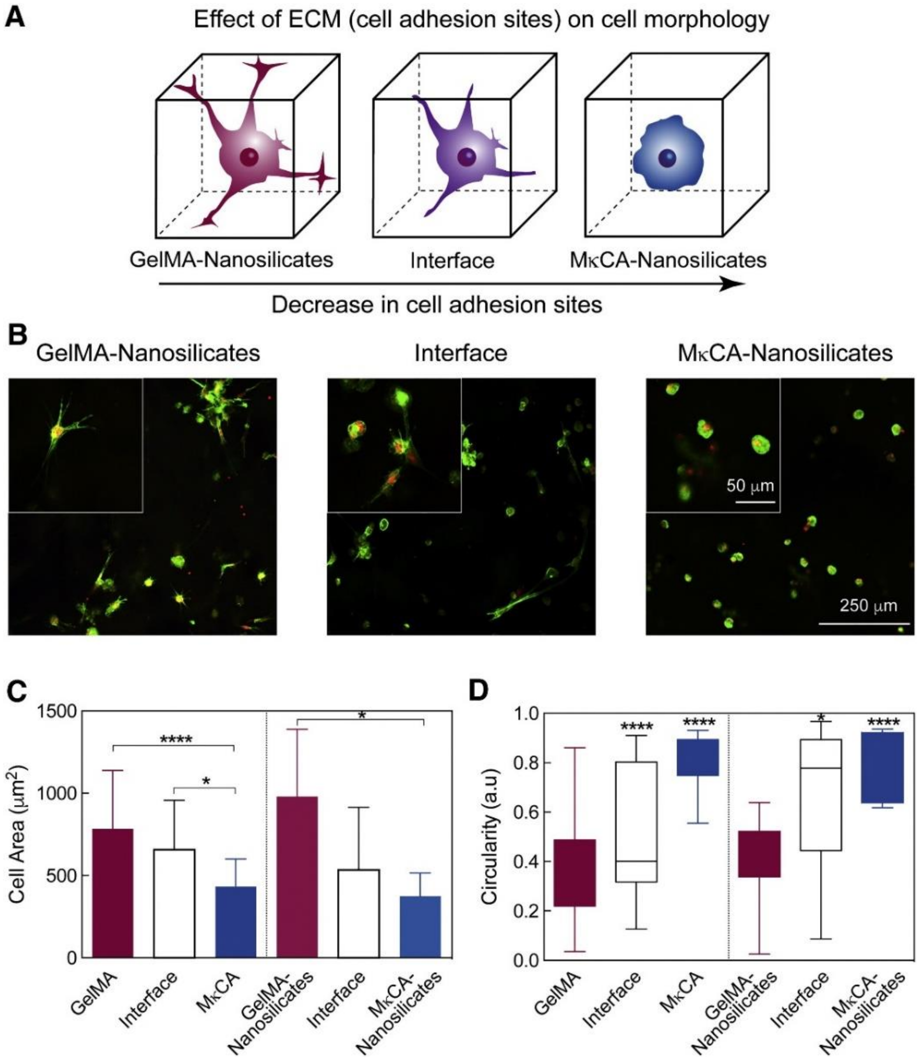

Figure 5-6 Gradient in cell adhesion and morphology. (A) Schematic demonstrating change in cell morphology along gradient hydrogel. As the cell adhesion sites decrease, the cell morphology becomes rounder. (B) Increased cell spreading was observed in the GelMA nSi region after three days of culture while in the MκCA nSi region, cell morphology remained significantly round. At the interface region, both cell morphologies were present. (C) Cell area decreased along the gradient scaffold from the GelMA to the MκCA region. The addition of nanosilicates increased the cell area in the GelMA region while its inclusion did not significantly affect the cell area in the MκCA or interface regions. (D) Similarly, cell circularity was much greater in the MκCA regions compared to the GelMA regions where cells were observed to be more spread out. (Statistical analysis: One-way ANOVA with Tukey's post-hoc analysis, **P*-value < 0.05, ***P*-value < 0.01, ****P*-value < 0.001, *****P*-value < 0.0001).

In addition to circularity, the average cell area along the gradient scaffolds was calculated. Average cell area decreased from the GelMA region (783.5 ± 354.7 μm^2) where cells were spread out, to the interface region (656.9 ± 300.1 μm^2) and to the MκCA region (431.3 ± 169.5 μm^2) where cells were more rounded (Figure 5-6c). When nanosilicates were incorporated into the scaffold, average cell area was not significantly affected but a similar trend existed.

5.4 Discussion

Gradient scaffolds were successfully fabricated utilizing gelatin, κ-carrageenan, and nanosilicates in a facile microfabrication process. Previously, gelatin and κ-carrageenan have shown to mix well in solution, supporting the ability to form a gradient.(265, 268) In addition, once in solution together, the polymers interact with one another via electrostatic interactions.(268) These initial interactions may allow for the solutions to be loosely bound prior to UV crosslinking and further enhance the connectivity of the scaffold. Additionally, incorporation of nanosilicates with these two natural materials have previously shown to enhance shear-thinning characteristics as well as structural and mechanical properties via electrostatic interactions.(41, 250) Structural, mechanical, and biological gradients were successfully generated in the micro-fabricated scaffolds utilizing these natural polymers and nanosilicates.

Investigating the microstructures of the gradient hydrogels via SEM revealed a gradient in the structure, specifically with the changes in mesh size. Mesh size is important for nutrient diffusion as well as cell infiltration in the scaffold.(269) For bone regeneration, some studies have reported optimal mesh sizes around 100 μm, while others have suggested lower pore size around 16 μm to support osteogenesis.(270, 271) In the present study, the mesh size of the GelMA regions of the scaffold fall within this smaller range; however, previous studies investigating GelMA for bone regeneration have demonstrated this mesh size to be sufficient.(41) Similarly for cartilage regeneration, a previous study suggested mesh size within the range of 50 to 500 μm to support chondrogenensis and as the mesh size increased, cartilage specific markers increased.(272) Here, the mesh size of MκCA fell within this range. Overall, the observed increase in mesh area across the hydrogels indicated the formation of a structural gradient in the two scaffolds. This gradient in mesh size could promote cell differentiation along the scaffold for bone-cartilage regeneration.

In addition, a gradient in mechanical properties was observed across the scaffold via compression tests. Although a gradual change in moduli was observed, high error was still present in some of the samples as a result of the small sample and sample geometry. In addition, achieving reproducibility in the six regions tested along the gradient hydrogel was difficult. Regardless of these difficulties, a distinct transition in the mechanical properties of both gradient hydrogels was observed indicating successful fabrication of a gradient in mechanical properties. As previously discussed, hydrogel stiffness can be influential in directing cell morphology and possibly cell differentiation.(273, 274) With the present gradient in the nanocomposite's mechanical properties, the scaffold holds the potential to further stimulate cell morphology and subsequently cell differentiation along the different regions.

Finally, encapsulated hMSCs demonstrated a gradient in the biological properties of the scaffold, specifically through observation of changes in cell morphology along the gradient. Although the standard deviation in average cell area was high in the GelMA and interface regions with and without nanosilicates, this is most likely a result of the projection of images required to obtain a clean image with encapsulated cells which then layered cells over one another making it difficult to distinguish individual cells. In addition, although the majority of the GelMA and GelMA nSi regions contained cells exhibiting spread morphologies, some round cells were still present, bringing down the average area and increasing the standard deviation. Unfortunately, the role of nanosilicates in directing cell morphology was not as pronounced at the low chosen concentration even though the addition significantly affected mechanical properties of the scaffold. These cell encapsulation studies indicated the ability to control cell morphology along a gradient scaffold. Although cell differentiation was not investigated in this study, this change in cell shape along the nanocomposite implies the potential for controlling cell fate. More importantly, cell morphology was controlled with just the material selection and incorporation of nanosilicates.

5.5 Conclusion

Overall, in this study we have introduced a simple and reproducible approach for fabricating nanocomposite gradient hydrogels. The inclusion of nanosilicates, a novel 2D nanomaterial, allowed for control over the structural, mechanical, and biological properties. Specifically, the structural and mechanical properties of the gradient hydrogel were characterized demonstrating the ability to vary these properties through material selection and generate a gradient in these physical properties. In addition, successful cell encapsulation and control over cell morphology demonstrates the potential to direct cell fate within the network and possibly direct cell differentiation without the use of growth factors. This simple approach could be applied to regeneration of the bone-cartilage interface where a natural gradient in the structural, mechanical, and biological properties exists as well as tailored to other tissue engineering applications.

6. FUTURE RECOMMENDATIONS

The preceding studies have demonstrated the versatility of nanosilicates in modulating differentiation of human mesenchymal stem cell towards osteogenic and chondrogenic lineages, delivering protein therapeutics for prolonged duration, and reinforcing tissue engineered constructs for tissue engineering. While the studies provide strong potential of nanosilicates for replacing standard bioactive cues, the present work also presents several future avenues for the field of orthopedic tissue regeneration.

Here we have shown that nanosilicates stimulate osteogenic and chondrogenic differentiation in hMSCs using whole-transcriptome sequencing (RNA-seq). Using a biology or bioinformatics perspective, we were able to utilize a technique that has had limited use in the field of biomedical engineering. Along the same lines, future work could incorporate other bioinformatics techniques including proteomics and metabolomics and integrate this data with transcriptomics. The incorporation and correlation of these datasets via multi-omics would provide a more complete understanding of phenotypic changes to hMSCs. While multi-omics approaches have been recently investigated for understanding different diseases including cancer,(275, 276) they have not yet been incorporated into tissue or regenerative engineering strategies. In particular, this integrative approach has the potential to help further predict cellular responses to nanomaterials via a system-wide overview of regulatory processes. By probing multiple levels of molecular mechanisms, we can better predict and narrow down specific genetic targets of nanosilicates or other nanomaterials. Specifically, with proteomics we could confirm and quantify protein production as mRNA found through transcriptomics is not always translated to protein.(277) In addition, metabolomics could provide more information on cellular physiology as metabolites are considered to be cellular processes end products.(278) The integration of these data sets could provide a more holistic view of cellular phenotype and function after treatment with nanoparticles such as nanosilicates and allow for predicting future alternatives to traditional bioactive cues in regenerative engineering.

In this work, we investigate the effect of nanosilicate dissolution products (Li^+, Mg^{2+}, $Si(OH)_4$) on hMSC osteogenic differentiation. Protein production and some gene expression data support the role of individual ions on osteogenic differentiation, however, future RNA-sequencing of individual ions will provide greater insight on specific genes affected. For example, previous studies have suggested lithium ions to upregulate Wnt responsive genes via elevating cytosolic β-catenin.(164, 203) Silicon and magnesium ions have also been reported to stimulate collagen I formation and enhance bone cell adhesion, respectively.(161, 204) In addition to stimulating osteogenesis or promoting bone formation, other ions including copper and silicon have shown to promote angiogenesis.(279, 280) Using RNA-seq to elucidate genetic changes to hMSCs after treatment with ions such as these will allow us to map specific pathways regulated by these ions. We expect to observe pathways such as Wnt, MAPK, VEGF and/or IGF signaling.(201, 281) Importantly, we can begin to create libraries of ions and genetic targets that will help design novel mineral-based nanoparticles for specific tissue regeneration strategies.

In addition, while our results support the ion dissolution products of nanosilicates help stimulate differentiation, the particle shape, size, and ion composition could also affect hMSC behavior.

Future studies could investigate this as the nanosilicates or nanoclays used in this work are also available in different sizes and with different ion compositions. The size of the particle could affect cellular uptake as it has been shown that certain endocytosis mechanisms are dependent on particle size.(239) In addition, the nanoparticle composition or ion makeup could affect the surface charge which dictates protein adsorption or protein corona formation and could subsequently affect surface receptors the nanoparticle binds to, affecting downstream signaling processes.(165, 237). Investigating different ion compositions could also result in different hMSC responses because nanoparticle dissociation or ion dissolution could stimulate different genes and pathways. It would be interesting to investigate the transcriptional changes to human mesenchymal stem cells with the addition of these different particle sizes, shapes, and compositions and compare the effects. Comparing genetic changes after treatment with different nanosilicates could provide greater insight on shape/size/composition effects on modulating hMSC behavior and differentiation. Genes differentially regulated across all nanosilicates tested could be identified and particles stimulating specific pathways such as differentiation could also be found, helping to narrow down which attributes of the particle are dictating certain processes. In addition, to investigate intracellular delivery of the ions that makeup the nanosilicates used in the previous studies, the ions could be encapsulated into a PLGA nanoparticles and delivered to hMSCs. This would allow for comparison of how much the physical characteristics of the particle dictate cellular responses compared to the chemical composition.

In addition, in this work, we demonstrate the ability of nanosilicates to act as a therapeutic delivery vehicle for osteogenic differentiation in hMSCs. These studies are very promising and present the potential to reduce growth factor incorporation in future regeneration strategies. Future studies could incorporate this system into an injectable hydrogel or even a pre-established material such as the collagen sponges used in Medronic's Infuse® Bone Graft. Rather than soaking the sponges in a solution of rhBMP2, the sponge could easily be soaked in a solution of nanosilicates with bound rhBMP2. Not only could the concentration of rhBMP2 be significantly reduced since the nanosilicates can sustain release, but also the innate osteoinductivity of nanosilicates could improve bone regeneration.

Along the same lines, future studies could incorporate low concentrations of growth factors into the gradient hydrogel presented in Chapter 5. Specifically, rhBMP2 could be bound to nanosilicates before incorporation into GelMA for the bone region and TGF-β could be bound to nanosilicates before incorporation into MκCA for the cartilage region. hMSC differentiation could then be monitored along the gradient. A potential problem with MκCA is that it has a high swelling degree which could lead to a burst release of the incorporated growth factor. However, incorporation of nanosilicates has shown to reduce swelling and binding of TGF-β to the nanosilicates prior to incorporation into MκCA should prolong release of the growth factor. In addition, the work presented here demonstrates that nanosilicates can induce both osteogenesis and chondrogenesis so incorporation of low dosages of growth factor for both bone and cartilage along with the nanosilicates should also enable hMSC differentiation. While the current system is a good platform to demonstrate the ability to form a gradient in structural and mechanical properties as well as cell morphology using these materials, this system is not necessarily translatable to implantation *in vivo*. Therefore, future studies could optimize this system to fabricate gradient hydrogels using either 3D bioprinting, microfluidics, or gradient makers. These techniques could also allow for greater mixing of materials and more precise control of gradient formation.

7. CONCLUSIONS

Through this work we have demonstrated the unique biomedical capabilities of nanosilicates (Laponite XLG), specifically for regeneration of orthopedic tissues such as bone and cartilage. In particular, we have developed a nanosilicate-based platform that can (a) stimulate hMSC osteogenic and chondrogenic differentiation without external growth factors, (b) act as a delivery vehicle for sustained and localized delivery of therapeutic growth factors as well as augment differentiation, and (c) be incorporated into a hydrogel composite to aid in bone-cartilage tissue regeneration.

In Study 1, "*Two-Dimensional Nanosilicates Stimulate and Modulate Human Mesenchymal Stem Cells*," Utilizing RNA-sequencing, hMSCs after treatment with nanosilicates were investigated at the whole-transcriptome level to gain a holistic understanding of nanosilicate-hMSC interactions. Nanosilicates significantly and differentially regulated over 4,000 genes compared to untreated hMSCs and activated key cellular pathways including MAPK signaling. Importantly, genes and pathways related to both osteogenic and chondrogenic differentiation were also significantly regulated, highlighting the potential for the use of this nanomaterial in regenerative engineering strategies. While researchers have used RNA-seq in other fields to investigate changes at the transcriptome level in cancer for example, this approach for predicting genetic targets of nanomaterials is novel in the field of tissue or regenerative engineering.

To further investigate mechanisms of nanosilicates innate bioactivity, in Study 2, "*Mineral Nanoparticle Dissociation Influences Human Mesenchymal Stem Cell Osteogenic Differentiation*," nanosilicate dissociation into their individual ions (Li^+, Mg^{2+}, and $Si(OH)_4$) at physiological pH was evaluated. Using ICP-MS, significant dissociation was observed at extracellular (~7.4) and intracellular (~5.5) pH. hMSC viability after treatment with various concentrations of ions was monitored and importantly the concentration of ions, even if 100% dissociation was achieved, fell within a safe and viable concentration range. hMSCs were treated with concentrations observed in dissociation and osteogenic differentiation was evaluated, revealing the role of these individual ions in differentiation. While an increase in osteo-specific proteins and genes were observed with the individual ions, the combination of all three ions revealed the most similar increase to nanosilicates, supporting the delivery within one particle. Investigating the individual minerals, however, did provide insight into pathways that are stimulated and provides valuable information for future studies to design specific mineral-based nanoparticles to direct hMSC differentiation. In addition, future whole transcriptome sequencing of hMSCs after individual ion treatment will uncover more specific genes and pathways.

In Study 3, "*Localized Therapeutic Delivery from 2D Nanosilicates Directs Differentiation of Human Mesenchymal Stem Cells*," nanosilicates were utilized as a delivery vehicle to localize rhBMP2 and TGF-β_3 to hMSCs. The unique physical properties of nanosilicates, namely their dual charge, allow for a variety of interactions with proteins and small molecules. Nanosilicate-protein interactions were evaluated and their ability to bind and release proteins overtime were demonstrated. Nanosilicates were used to deliver therapeutic and safe concentrations of bone morphogenetic protein (rhBMP2) and transforming growth factor beta (TGF-β_3) to hMSCs and osteogenic and chondrogenic differentiation were evaluated respectively and compared to hMSCs treated with exogenous growth factor. Importantly, hMSCs treated once with nanosilicate/growth factor expressed greater differentiation than hMSCs treated repeatedly with exogenous growth factor, demonstrating the ability of nanosilicates to sustain and localize therapeutic delivery. In addition, nanosilicates allowed for delivering significantly lower concentrations of growth factor compared to other studies. Nanosilicates can act as a delivery vehicle for future tissue engineering strategies to reduce the concentration of growth factors necessary for successful regeneration.

Finally, in Study 4, "*Gradient Nanocomposite Hydrogels for Interface Tissue Engineering*," nanosilicates were incorporated into natural materials (GelMA and MκCA) and a gradient hydrogel was fabricated for potential bone and cartilage interface tissue regeneration. Material selection and characterization was performed to optimize the concentration of materials in the final composite. In addition, optimization of gradient hydrogel formation was done to ensure sufficient mixing of the two materials. Successful fabrication of gradient hydrogels was completed and a gradient in structural and mechanical properties was demonstrated. hMSCs were encapsulated within the gradient hydrogels and cell morphology was assessed, revealing increased spreading in the GelMA regions whereas the MκCA region exhibited limited spreading due to lack of cell binding motifs. Importantly, this gradation in cell morphology mimics the native bone-cartilage interface where different cell morphologies are present; specifically, in native bone, cells are spread whereas in native cartilage, cells have a more rounded morphology. This facile fabrication method could be used in future studies for bone-cartilage regeneration or other tissue regeneration strategies.

These works demonstrate the capabilities of nanosilicates as an alternative bioactive nanomaterial that has great potential in the field of tissue or regenerative engineering. Utilizing the unique biochemical and biophysical properties of nanosilicates, a platform was designed. While in this work we mainly utilize this platform to investigate bone regeneration, RNA-sequencing uncovered other differentiation pathways including chondrogenesis and angiogenesis. As a result, nanosilicates could be utilized to deliver other growth factors including vascular endothelial growth factor (VEGF) for enhancing vascularization. In addition, nanosilicates can be incorporated into a variety of polymers or hydrogels for different tissue engineering applications.

In order to develop and test new bioactive materials for tissue engineering, we can borrow techniques from other science and engineering fields. Here we have leveraged RNA-sequencing to uncover genetic changes to hMSCs after treatment with one nanomaterial, nanosilicates. This technique holds great potential for future nanomaterials and can help predict the regenerative capabilities of novel nanomaterials to help replace traditional bioactive cues like growth factors.

REFERENCES

1. Romeyn RL, Jennings J, & Davies GJ (2008) Surgical Treatment and Rehabilitation of Combined Complex Ligament Injuries. *North American Journal of Sports Physical Therapy : NAJSPT* 3(4):212-225.
2. Indelicato PA, Hermansdorfer J, & Huegel M (1990) Nonoperative management of complete tears of the medial collateral ligament of the knee in intercollegiate football players. *Clinical orthopaedics and related research* (256):174-177.
3. Augat P & Schorlemmer S (2006) The role of cortical bone and its microstructure in bone strength. *Age and ageing* 35 Suppl 2:ii27-ii31.
4. Gibson LJ (1985) The mechanical behavior of cancellous bone. *J. Biomechanics* 18(5):317-328.
5. Kozielski M*, et al.* (2011) Determination of composition and structure of spongy bone tissue in human head of femur by Raman spectral mapping. *Journal of Materials Science. Materials in Medicine* 22(7):1653-1661.
6. Fung YC (1996) Bone and Cartilage. *Biomechanics: Mechanical Properties of Living Tissues*), pp 500-544.
7. Hsiao SF, Chou PH, Hsu HC, & Lue YJ (2014) Changes of muscle mechanics associated with anterior cruciate ligament deficiency and reconstruction. *Journal of strength and conditioning research / National Strength & Conditioning Association* 28(2):390-400.
8. Ma PX & Langer R (1999) Morphology and mechanical function of long-term in vitro engineered cartilage. *Journal of biomedical materials research* 44(2):217-221.

9. Butler DL, *et al.* (2008) Functional tissue engineering for tendon repair: A multidisciplinary strategy using mesenchymal stem cells, bioscaffolds, and mechanical stimulation. *Journal of orthopaedic research : official publication of the Orthopaedic Research Society* 26(1):1-9.

10. Moutos FT, Freed LE, & Guilak F (2007) A biomimetic three-dimensional woven composite scaffold for functional tissue engineering of cartilage. *Nat Mater* 6(2):162-167.

11. Sasisekharan V, Raman R, & Sasisekharan R (2005) Structural Insights into Biological Roles of Protein-Glycosaminoglycan Interactions. *Chemistry & biology* 12(3):267-277.

12. Wang X*, et al.* (2009) Growth Factor Gradients via Microsphere Delivery in Biopolymer Scaffolds for Osteochondral Tissue Engineering. *Journal of controlled release : official journal of the Controlled Release Society* 134(2):81-90.

13. Vincent JP*, et al.* (2012) The anterolateral ligament of the human knee: an anatomic and histologic study. *Knee surgery, sports traumatology, arthroscopy : official journal of the ESSKA* 20(1):147-152.

14. Gilmore RS & Palfrey AJ (1988) Chondrocyte distribution in the articular cartilage of human femoral condyles. *Journal of Anatomy* 157:23-31.

15. Yang PJ & Temenoff JS (2009) Engineering orthopedic tissue interfaces. *Tissue Engineering Part B: Reviews* 15(2):127-141.

16. Seidi A, Ramalingam M, Elloumi-Hannachi I, Ostrovidov S, & Khademhosseini A (2011) Gradient biomaterials for soft-to-hard interface tissue engineering. *Acta Biomaterialia* 7(4):1441-1451.

17. Lu HH, Subramony SD, Boushell MK, & Zhang X (2010) Tissue engineering strategies for the regeneration of orthopedic interfaces. *Annals of biomedical engineering* 38(6):2142-2154.

18. Moffat KL, Wang I-NE, Rodeo SA, & Lu HH (2009) Orthopedic interface tissue engineering for the biological fixation of soft tissue grafts. *Clinics in sports medicine* 28(1):157-176.

19. Dormer NH, Berkland CJ, & Detamore MS (2010) Emerging techniques in stratified designs and continuous gradients for tissue engineering of interfaces. *Annals of biomedical engineering* 38(6):2121-2141.

20. Castro NJ, Hacking SA, & Zhang LG (2012) Recent progress in interfacial tissue engineering approaches for osteochondral defects. *Annals of biomedical engineering* 40(8):1628-1640.

21. Singh M, Berkland C, & Detamore MS (2008) Strategies and applications for incorporating physical and chemical signal gradients in tissue engineering. *Tissue Engineering Part B: Reviews* 14(4):341-366.

22. Sant S, Hancock MJ, Donnelly JP, Iyer D, & Khademhosseini A (2010) Biomimetic gradient hydrogels for tissue engineering. *The Canadian journal of chemical engineering* 88(6):899-911.

23. Oh SH, Park IK, Kim JM, & Lee JH (2007) In vitro and in vivo characteristics of PCL scaffolds with pore size gradient fabricated by a centrifugation method. *Biomaterials* 28(9):1664-1671.

24. Park H, *et al.* (2007) Nanofabrication and microfabrication of functional materials for tissue engineering. *Tissue engineering* 13(8):1867-1877.

25. Gaharwar AK, Peppas NA, & Khademhosseini A (2014) Nanocomposite hydrogels for biomedical applications. *Biotechnol. Bioeng.* 111(3):441-453.

26. Carrow JK & Gaharwar AK (2015) Bioinspired Polymeric Nanocomposites for Regenerative Medicine. *Macromolecular Chemistry and Physics* 216(3):248−264.

27. Kerativitayanan P, Carrow JK, & Gaharwar AK (2015) Nanomaterials for Engineering Stem Cell Responses. *Advanced Healthcare Materials* 4(11):1600–1627.

28. Zhao C, Tan A, Pastorin G, & Ho HK (2013) Nanomaterial scaffolds for stem cell proliferation and differentiation in tissue engineering. *Biotechnology advances* 31(5):654-668.

29. Zhang L & Webster TJ (2009) Nanotechnology and nanomaterials: promises for improved tissue regeneration. *Nano Today* 4(1):66-80.

30. Tuzlakoglu K*, et al.* (2005) Nano-and micro-fiber combined scaffolds: a new architecture for bone tissue engineering. *Journal of Materials Science: Materials in Medicine* 16(12):1099-1104.

31. Gaharwar AK*, et al.* (2014) Amphiphilic beads as depots for sustained drug release integrated into fibrillar scaffolds. *Journal of Controlled Release* 187:66-73.

32. Gaharwar AK*, et al.* (2014) Nanoclay-enriched poly (ε-caprolactone) electrospun Scaffolds for osteogenic differentiation of human mesenchymal stem cells. *Tissue Engineering Part A* 20(15-16):2088-2101.

33. Xue D*, et al.* (2010) Osteochondral repair using porous poly(lactide-co-glycolide)/nano-hydroxyapatite hybrid scaffolds with undifferentiated mesenchymal stem cells in a rat model. *Journal of Biomedical Materials Research Part A* 94A(1):259-270.

34. Liu C, Han Z, & Czernuszka JT (2009) Gradient collagen/nanohydroxyapatite composite scaffold: Development and characterization. *Acta Biomaterialia* 5(2):661-669.

35. Ravichandran R, Venugopal JR, Sundarrajan S, Mukherjee S, & Ramakrishna S (2012) Precipitation of nanohydroxyapatite on PLLA/PBLG/Collagen nanofibrous structures for the differentiation of adipose derived stem cells to osteogenic lineage. *Biomaterials* 33(3):846-855.

36. Zandi M, *et al.* (2010) Biocompatibility evaluation of nano-rod hydroxyapatite/gelatin coated with nano-HAp as a novel scaffold using mesenchymal stem cells. *Journal of Biomedical Materials Research Part A* 92A(4):1244-1255.

37. Gaharwar AK, *et al.* (2013) Bioactive Silicate Nanoplatelets for Osteogenic Differentiation of Human Mesenchymal Stem Cells. *Adv Mater* 25(24):3329-3336.

38. Chimene D, Alge DL, & Gaharwar AK (2015) Two-Dimensional Nanomaterials for Biomedical Applications: Emerging Trends and Future Prospects. *Advanced Materials* 27(45):7261–7284.

39. Gaharwar AK, *et al.* (2012) Physically Crosslinked Nanocomposites from Silicate-Crosslinked PEO: Mechanical Properties and Osteogenic Differentiation of Human Mesenchymal Stem Cells. *Macromolecular Bioscience* 12(6):779-793.

40. Gaharwar AK, Schexnailder PJ, Kline BP, & Schmidt G (2011) Assessment of using Laponite® cross-linked poly(ethylene oxide) for controlled cell adhesion and mineralization. *Acta Biomaterialia* 7(2):568-577.

41. Xavier JR, *et al.* (2015) Bioactive Nanoengineered Hydrogels for Bone Tissue Engineering: A Growth-Factor-Free Approach. *ACS Nano* 9(3):3109-3118.

42. Goenka S, Sant V, & Sant S (2014) Graphene-based nanomaterials for drug delivery and tissue engineering. *Journal of Controlled Release* 173:75-88.

43. Nayak TR, *et al.* (2011) Graphene for Controlled and Accelerated Osteogenic Differentiation of Human Mesenchymal Stem Cells. *ACS Nano* 5(6):4670-4678.

44. Tatavarty R, Ding H, Lu G, Taylor RJ, & Bi X (2014) Synergistic acceleration in the osteogenesis of human mesenchymal stem cells by graphene oxide-calcium phosphate nanocomposites. *Chemical Communications* 50(62):8484-8487.

45. Liu M, *et al.* (2015) An anisotropic hydrogel with electrostatic repulsion between cofacially aligned nanosheets. *Nature* 517(7532):68-72.

46. Erisken C, Kalyon DM, & Wang H (2008) Functionally graded electrospun polycaprolactone and β-tricalcium phosphate nanocomposites for tissue engineering applications. *Biomaterials* 29(30):4065-4073.

47. Kolluru PV, *et al.* (2013) Strong and tough mineralized PLGA nanofibers for tendon-to-bone scaffolds. *Acta Biomaterialia* 9(12):9442-9450.

48. Moffat KL KA, Spalazzi JP, Doty SB, Levine WN, Lu HH (2008) Novel nanofiber-based scaffold for rotator cuff repair and augmentation. *Tissue Engineering Part A* 14:1-12.

49. Zhang YZ, Venugopal J, Huang ZM, Lim CT, & Ramakrishna S (2005) Characterization of the surface biocompatibility of the electrospun PCL-Collagen nanofibers using fibroblasts. *Biomacromolecules* 6(5):2583-2589.

50. Xie J, *et al.* (2010) "Aligned-to-random" nanofiber scaffolds for mimicking the structure of the tendon-to-bone insertion site. *Nanoscale* 2(6):923-926.

51. Sun W, Puzas JE, Sheu TJ, Liu X, & Fauchet PM (2007) Nano-to Microscale Porous Silicon as a Cell Interface for Bone-Tissue Engineering. *Advanced materials* 19(7):921-924.

52. Pek YS, Wan AC, & Ying JY (2010) The effect of matrix stiffness on mesenchymal stem cell differentiation in a 3D thixotropic gel. *Biomaterials* 31(3):385-391.

53. Gelinsky M, Eckert M, & Despang F (2007) Biphasic, but monolithic scaffolds for the therapy of osteochondral defects. *International Journal of Materials Research* 98(8):749-755.

54. Ghosh S, Viana JC, Reis RL, & Mano JF (2008) Bi-layered constructs based on poly(l-lactic acid) and starch for tissue engineering of osteochondral defects. *Materials Science and Engineering: C* 28(1):80-86.

55. Qu D*, et al.* (2011) Ectopic osteochondral formation of biomimetic porous PVA-n-HA/PA6 bilayered scaffold and BMSCs construct in rabbit. *Journal of Biomedical Materials Research Part B: Applied Biomaterials* 96B(1):9-15.

56. Yan L-P, *et al.* (2015) Bilayered silk/silk-nanoCaP scaffolds for osteochondral tissue engineering: In vitro and in vivo assessment of biological performance. *Acta Biomaterialia* 12:227-241.

57. Soo Kim B*, et al.* (2014) Human collagen-based multilayer scaffolds for tendon-to-bone interface tissue engineering. *Journal of Biomedical Materials Research Part A* 102(11):4044-4054.

58. Liverani L*, et al.* (2012) Simple fabrication technique for multilayered stratified composite scaffolds suitable for interface tissue engineering. *Materials Science and Engineering: A* 557(0):54-58.

59. He J, *et al.* (2015) Design and fabrication of biomimetic multiphased scaffolds for ligament-to-bone fixation. *Materials Science and Engineering: C* 50(0):12-18.

60. Sridharan B, Sharma BPD, & Detamore MS (2015) A Roadmap to Commercialization of Cartilage Therapy in the United States of America. *Tissue engineering. Part B, Reviews*.

61. Robinson DE, Winson IG, Harries WJ, & Kelly AJ (2003) Arthroscopic treatment of osteochondral lesions of the talus. *The Journal of bone and joint surgery. British volume* 85(7):989-993.

62. Marcacci M, *et al.* (2002) Arthroscopic autologous chondrocyte transplantation: technical note. *Knee surgery, sports traumatology, arthroscopy : official journal of the ESSKA* 10(3):154-159.

63. Ossendorf C, *et al.* (2007) Treatment of posttraumatic and focal osteoarthritic cartilage defects of the knee with autologous polymer-based three-dimensional chondrocyte grafts: 2-year clinical results. *Arthritis research & therapy* 9(2):R41.

64. Andereya S, *et al.* (2006) [First clinical experiences with a novel 3D-collagen gel (CaReS) for the treatment of focal cartilage defects in the knee]. *Zeitschrift fur Orthopadie und ihre Grenzgebiete* 144(3):272-280.

65. Adachi N, Ochi M, Deie M, Ishikawa M, & Ito Y (2007) Osteonecrosis of the knee treated with a tissue-engineered cartilage and bone implant. A case report. *The Journal of bone and joint surgery. American volume* 89(12):2752-2757.

66. Selmi TA, *et al.* (2008) Autologous chondrocyte implantation in a novel alginate-agarose hydrogel: outcome at two years. *The Journal of bone and joint surgery. British volume* 90(5):597-604.

67. Crawford DC, Heveran CM, Cannon WD, Jr., Foo LF, & Potter HG (2009) An autologous cartilage tissue implant NeoCart for treatment of grade III chondral injury to the distal femur: prospective clinical safety trial at 2 years. *The American journal of sports medicine* 37(7):1334-1343.

68. Choi NY*, et al.* (2010) Gel-type autologous chondrocyte (Chondron) implantation for treatment of articular cartilage defects of the knee. *BMC musculoskeletal disorders* 11:103.

69. Panagopoulos A, van Niekerk L, & Triantafillopoulos I (2012) Autologous chondrocyte implantation for knee cartilage injuries: moderate functional outcome and performance in patients with high-impact activities. *Orthopedics* 35(1):e6-14.

70. Scotti C*, et al.* (2010) Engineering human cell-based, functionally integrated osteochondral grafts by biological bonding of engineered cartilage tissues to bony scaffolds. *Biomaterials* 31(8):2252-2259.

71. Auyeung J, Patil S, & Gower A (2010) HOLY COW. BEWARE OF THE PERILS OF TUTOBONE IN HINDFOOT FUSION. *Journal of Bone & Joint Surgery, British Volume* 92-B(SUPP I):242.

72. Jeon JE, Vaquette C, Klein TJ, & Hutmacher DW (2014) Perspectives in multiphasic osteochondral tissue engineering. *The Anatomical Record* 297(1):26-35.

73. Nooeaid P, Roether JA, Weber E, Schubert DW, & Boccaccini AR (2014) Technologies for multilayered scaffolds suitable for interface tissue engineering. *Advanced Engineering Materials* 16(3):319-327.

74. Scotti C*, et al.* (2007) A tissue engineered osteochondral plug: an in vitro morphological evaluation. *Knee Surg Sports Traumatol Arthr* 15(11):1363-1369.

75. Ringe J & Sittinger M (2014) Regenerative medicine: Selecting the right biological scaffold for tissue engineering. *Nature Reviews Rheumatology* 10(7):388-389.

76. Hung CT, *et al.* (2003) Anatomically shaped osteochondral constructs for articular cartilage repair. *Journal of Biomechanics* 36(12):1853-1864.

77. Hadjipanayi E, Brown RA, & Mudera V (2009) Interface integration of layered collagen scaffolds with defined matrix stiffness: implications for sheet-based tissue engineering. *Journal of Tissue Engineering and Regenerative Medicine* 3(3):230-241.

78. Owen TA, *et al.* (1990) Progressive development of the rat osteoblast phenotype in vitro: reciprocal relationships in expression of genes associated with osteoblast proliferation and differentiation during formation of the bone extracellular matrix. *Journal of cellular physiology* 143(3):420-430.

79. Khanarian NT, Haney NM, Burga RA, & Lu HH (2012) A functional agarose-hydroxyapatite scaffold for osteochondral interface regeneration. *Biomaterials* 33(21):5247-5258.

80. Dua R, Centeno J, & Ramaswamy S (2014) Augmentation of engineered cartilage to bone integration using hydroxyapatite. *Journal of Biomedical Materials Research Part B: Applied Biomaterials* 102(5):922-932.

81. Yan L-P, *et al.* (2012) Bioactive macro/micro porous silk fibroin/nano-sized calcium phosphate scaffolds with potential for bone-tissue-engineering applications. *Nanomedicine* 8(3):359-378.

82. Yan L-P, Salgado AJ, Oliveira JM, Oliveira AL, & Reis RL (2013) De novo bone formation on macro/microporous silk and silk/nano-sized calcium phosphate scaffolds. *Journal of Bioactive and Compatible Polymers* 28(5):439-452.

83. Ding X, *et al.* (2014) Integrated Trilayered Silk Fibroin Scaffold for Osteochondral Differentiation of Adipose-Derived Stem Cells. *ACS Applied Materials & Interfaces* 6(19):16696-16705.

84. Ting Z, Jingjing W, Jiaoyan L, Ying L, & Ying W (2015) Fabrication and characterization of layered chitosan/silk fibroin/nano-hydroxyapatite scaffolds with designed composition and mechanical properties. *Biomedical Materials* 10(4):045013.

85. Zizak I, *et al.* (2003) Characteristics of mineral particles in the human bone/cartilage interface. *Journal of Structural Biology* 141(3):208-217.

86. Foss C, Merzari E, Migliaresi C, & Motta A (2013) Silk Fibroin/Hyaluronic Acid 3D Matrices for Cartilage Tissue Engineering. *Biomacromolecules* 14(1):38-47.

87. Liu H, *et al.* (2015) Composite scaffolds of nano-hydroxyapatite and silk fibroin enhance mesenchymal stem cell-based bone regeneration via the interleukin 1 alpha autocrine/paracrine signaling loop. *Biomaterials* 49:103-112.

88. Kundu B, Rajkhowa R, Kundu S, & Wang X (2013) Silk fibroin biomaterials for tissue regenerations. *Advanced drug delivery reviews* 65(4):457-470.

89. Vepari C & Kaplan D (2007) Silk as a biomaterial. *Progress in polymer science* 32(8-9):991-1007.

90. Christensen B, Foldager C, Jensen J, Jensen N, & Lind M (2015) Poor osteochondral repair by a biomimetic collagen scaffold: 1- to 3-year clinical and radiological follow-up. *Knee Surg Sports Traumatol Arthr*:1-8.

91. Filardo G, Di Martino A, Kon E, Delcogliano M, & Marcacci M (2012) Midterm results of a combined biological and mechanical approach for the treatment of a complex knee lesion. *Cartilage* 3(3):288-292.

92. Tampieri A, *et al.* (2008) Design of graded biomimetic osteochondral composite scaffolds. *Biomaterials* 29(26):3539-3546.

93. Delcogliano M, *et al.* (2014) Use of innovative biomimetic scaffold in the treatment for large osteochondral lesions of the knee. *Knee Surg Sports Traumatol Arthr* 22(6):1260-1269.

94. Sutherland AJ, *et al.* (2015) Decellularized cartilage may be a chondroinductive material for osteochondral tissue engineering. *PloS one* 10(5):e0121966.

95. Gaharwar AK, Arpanaei A, Andresen TL, & Dolatshahi-Pirouz A (2016) 3D Biomaterial Microarrays for Regenerative Medicine: Current State-of-the-Art, Emerging Directions and Future Trends. *Advanced Materials* 28(4):771–781.

96. Dolatshahi-Pirouz A, *et al.* (2014) A combinatorial cell-laden gel microarray for inducing osteogenic differentiation of human mesenchymal stem cells. *Scientific reports* 4.

97. Hickey DJ, Ercan B, Sun L, & Webster TJ (2015) Adding MgO nanoparticles to hydroxyapatite–PLLA nanocomposites for improved bone tissue engineering applications. *Acta Biomaterialia* 14:175-184.

98. Hickey DJ, *et al.* (2014) MgO nanocomposites as new antibacterial materials for orthopedic tissue engineering applications. *Bioengineering Conference (NEBEC), 2014 40th Annual Northeast*, pp 1-2.

99. Barry M, Pearce H, Cross L, Tatullo M, & Gaharwar AK (2016) Advances in Nanotechnology for the Treatment of Osteoporosis. *Current Osteoporosis Reports*:1-8.

100. Thakur T, *et al.* (2016) Photocrosslinkable and Elastomeric Hydrogels for Bone Regeneration. *Journal of Biomedical Materials Research Part A* 104(4):879–888.

101. Xavier JR, Desai P, Varanasi VG, Al-Hashimi I, & Gaharwar AK (2015) Advanced Nanomaterials: Promises for Improved Dental Tissue Regeneration. *Nanotechnology in Endodontics*, (Springer International Publishing), Vol 1, pp 5-22.

102. Melchels FP*, et al.* (2012) Additive manufacturing of tissues and organs. *Progress in Polymer Science* 37(8):1079-1104.

103. Mironov V*, et al.* (2009) Organ printing: tissue spheroids as building blocks. *Biomaterials* 30(12):2164-2174.

104. Murphy SV & Atala A (2014) 3D bioprinting of tissues and organs. *Nat Biotech* 32(8):773-785.

105. Stanton M, Samitier J, & Sánchez S (2015) Bioprinting of 3D hydrogels. *Lab on a Chip* 15(15):3111-3115.

106. Zhu W*, et al.* (2016) 3D printing of functional biomaterials for tissue engineering. *Current Opinion in Biotechnology* 40:103-112.

107. Wang MO*, et al.* (2015) Evaluating 3D-Printed Biomaterials as Scaffolds for Vascularized Bone Tissue Engineering. *Advanced Materials* 27(1):138-144.

108. Vallés G*, et al.* (2015) Topographical cues regulate the crosstalk between MSCs and macrophages. *Biomaterials* 37:124-133.

109. Kutikov AB, Gurijala A, & Song J (2015) Rapid prototyping amphiphilic polymer/hydroxyapatite composite scaffolds with hydration-induced self-fixation behavior. *Tissue engineering. Part C, Methods* 21(3):229-241.

110. Jiang C-P, Chen Y-Y, Hsieh M-F, & Lee H-M (2013) Solid freeform fabrication and in-vitro response of osteoblast cells of mPEG-PCL-mPEG bone scaffolds. *Biomed Microdevices* 15(2):369-379.

111. Liao HT, Chen YY, Lai YT, Hsieh MF, & Jiang CP (2014) The osteogenesis of bone marrow stem cells on mPEG-PCL-mPEG/hydroxyapatite composite scaffold via solid freeform fabrication. *BioMed research international* 2014:321549.

112. Dorj B, *et al.* (2013) Robocasting nanocomposite scaffolds of poly(caprolactone)/hydroxyapatite incorporating modified carbon nanotubes for hard tissue reconstruction. *Journal of biomedical materials research. Part A* 101(6):1670-1681.

113. Lee JH, *et al.* (2013) Tethering bi-functional protein onto mineralized polymer scaffolds to regulate mesenchymal stem cell behaviors for bone regeneration. *Journal of Materials Chemistry B* 1(21):2731-2741.

114. Dorj B, Park J-H, & Kim H-W (2012) Robocasting chitosan/nanobioactive glass dual-pore structured scaffolds for bone engineering. *Materials Letters* 73(0):119-122.

115. Chimene D, Kimberly LK, Kaunas RR, & Gaharwar AK (2016) Advanced Bioinks for 3D Printing: A Materials Science Perspective. *Annals of Biomedical Engineering*:DOI: 10.1007/s10439-10016-11638-y.

116. Xu T, *et al.* (2013) Complex heterogeneous tissue constructs containing multiple cell types prepared by inkjet printing technology. *Biomaterials* 34(1):130-139.

117. Pati F, Gantelius J, & Svahn HA (2016) 3D Bioprinting of Tissue/Organ Models. *Angewandte Chemie International Edition* 55(15):4650-4665.

118. Skardal A & Atala A (2015) Biomaterials for Integration with 3-D Bioprinting. *Annals of Biomedical Engineering* 43(3):730-746.

119. Bailey BM, Nail LN, & Grunlan MA (2013) Continuous gradient scaffolds for rapid screening of cell–material interactions and interfacial tissue regeneration. *Acta Biomaterialia* 9(9):8254-8261.

120. Beck EC*, et al.* (2015) Enabling Surgical Placement of Hydrogels Through Achieving Paste-Like Rheological Behavior in Hydrogel Precursor Solutions. *Ann Biomed Eng* 43(10):2569-2576.

121. Butler SZ*, et al.* (2013) Progress, challenges, and opportunities in two-dimensional materials beyond graphene. *ACS nano* 7(4):2898-2926.

122. Chen Y, Tan CL, Zhang H, & Wang LZ (2015) Two-dimensional graphene analogues for biomedical applications. *Chem Soc Rev* 44(9):2681-2701.

123. Jiang W, Kim BYS, Rutka JT, & Chan WCW (2008) Nanoparticle-mediated cellular response is size-dependent. *Nature Nanotechnology* 3(3):145-150.

124. Verano-Braga T*, et al.* (2014) Insights into the Cellular Response Triggered by Silver Nanoparticles Using Quantitative Proteomics. *Acs Nano* 8(3):2161-2175.

125. Ge Y, Bruno M, Wallace K, Winnik W, & Prasad RY (2011) Proteome profiling reveals potential toxicity and detoxification pathways following exposure of BEAS-2B cells to engineered nanoparticle titanium dioxide. *Proteomics* 11(12):2406-2422.

126. Simon DF*, et al.* (2013) Transcriptome sequencing (RNA-seq) analysis of the effects of metal nanoparticle exposure on the transcriptome of Chlamydomonas reinhardtii. *Appl Environ Microbiol* 79(16):4774-4785.

127. Lucafo M*, et al.* (2013) Profiling the molecular mechanism of fullerene cytotoxicity on tumor cells by RNA-seq. *Toxicology* 314(1):183-192.

128. Larguinho M & Baptista PV (2012) Gold and silver nanoparticles for clinical diagnostics—from genomics to proteomics. *Journal of proteomics* 75(10):2811-2823.

129. Shendure J (2008) The beginning of the end for microarrays? *Nat Methods* 5(7):585-587.

130. Cloonan N, *et al.* (2008) Stem cell transcriptome profiling via massive-scale mRNA sequencing. *Nat Methods* 5(7):613-619.

131. Mortazavi A, Williams BA, McCue K, Schaeffer L, & Wold B (2008) Mapping and quantifying mammalian transcriptomes by RNA-Seq. *Nat Methods* 5(7):621-628.

132. Dawson JI & Oreffo RO (2013) Clay: new opportunities for tissue regeneration and biomaterial design. *Advanced Materials* 25(30):4069-4086.

133. Ghadiri M, Chrzanowski W, & Rohanizadeh R (2015) Biomedical applications of cationic clay minerals. *RSC Advances* 5(37):29467-29481.

134. Viseras C, Cerezo P, Sanchez R, Salcedo I, & Aguzzi C (2010) Current challenges in clay minerals for drug delivery. *Applied Clay Science* 48(3):291-295.

135. Ruzicka B, *et al.* (2011) Observation of empty liquids and equilibrium gels in a colloidal clay. *Nature Materials* 10(1):56-60.

136. Thompson DW & Butterworth JT (1992) The nature of laponite and its aqueous dispersions. *Journal of Colloid and Interface Science* 151(1):236-243.

137. Tawari SL, Koch DL, & Cohen C (2001) Electrical double-layer effects on the Brownian diffusivity and aggregation rate of Laponite clay particles. *J Colloid Interf Sci* 240(1):54-66.

138. Gaharwar AK, *et al.* (2013) Bioactive silicate nanoplatelets for osteogenic differentiation of human mesenchymal stem cells. *Adv Mater* 25(24):3329-3336.

139. Mihaila SM, *et al.* (2014) The osteogenic differentiation of SSEA-4 sub-population of human adipose derived stem cells using silicate nanoplatelets. *Biomaterials* 35(33):9087-9099.

140. Akhavan O, Ghaderi E, & Akhavan A (2012) Size-dependent genotoxicity of graphene nanoplatelets in human stem cells. *Biomaterials* 33(32):8017-8025.

141. Xavier JR, *et al.* (2015) Bioactive nanoengineered hydrogels for bone tissue engineering: a growth-factor-free approach. *ACS Nano* 9(3):3109-3118.

142. Gaharwar AK, Schexnailder PJ, Kline BP, & Schmidt G (2011) Assessment of using Laponite® cross-linked poly (ethylene oxide) for controlled cell adhesion and mineralization. *Acta biomaterialia* 7(2):568-577.

143. Wilson SA, Cross LM, Peak CW, & Gaharwar AK (2017) Shear-Thinning and Thermo-Reversible Nanoengineered Inks for 3D Bioprinting. *ACS applied materials & interfaces* 9(50):43449-43458.

144. Dawson JI, Kanczler JM, Yang XB, Attard GS, & Oreffo RO (2011) Clay gels for the delivery of regenerative microenvironments. *Advanced Materials* 23(29):3304-3308.

145. AshaRani P, Low Kah Mun G, Hande MP, & Valiyaveettil S (2008) Cytotoxicity and genotoxicity of silver nanoparticles in human cells. *ACS nano* 3(2):279-290.

146. Figueroa JAL, Stiner CA, Radzyukevich TL, & Heiny JA (2016) Metal ion transport quantified by ICP-MS in intact cells. *Scientific reports* 6:20551.

147. Dobin A, *et al.* (2013) STAR: ultrafast universal RNA-seq aligner. *Bioinformatics* 29(1):15-21.

148. Lawrence M, *et al.* (2013) Software for computing and annotating genomic ranges. *PLoS computational biology* 9(8):e1003118.

149. Anders S & Huber W (2010) Differential expression analysis for sequence count data. *Genome biology* 11(10):R106.

150. Supek F, Bošnjak M, Škunca N, & Šmuc T (2011) REVIGO summarizes and visualizes long lists of gene ontology terms. *PloS one* 6(7):e21800.

151. Shannon P*, et al.* (2003) Cytoscape: a software environment for integrated models of biomolecular interaction networks. *Genome research* 13(11):2498-2504.

152. Montojo J*, et al.* (2010) GeneMANIA Cytoscape plugin: fast gene function predictions on the desktop. *Bioinformatics* 26(22):2927-2928.

153. Bindea G*, et al.* (2009) ClueGO: a Cytoscape plug-in to decipher functionally grouped gene ontology and pathway annotation networks. *Bioinformatics* 25(8):1091-1093.

154. Huang DW, Sherman BT, & Lempicki RA (2008) Systematic and integrative analysis of large gene lists using DAVID bioinformatics resources. *Nature protocols* 4(1):44.

155. Peirson SN, Butler JN, & Foster RG (2003) Experimental validation of novel and conventional approaches to quantitative real-time PCR data analysis. *Nucleic acids research* 31(14):e73-e73.

156. Gregory CA, Gunn WG, Peister A, & Prockop DJ (2004) An Alizarin red-based assay of mineralization by adherent cells in culture: comparison with cetylpyridinium chloride extraction. *Analytical biochemistry* 329(1):77-84.

157. Hühn J*, et al.* (2016) Selected standard protocols for the synthesis, phase transfer, and characterization of inorganic colloidal nanoparticles. *Chemistry of Materials* 29(1):399-461.

158. Pena MD*, et al.* (2016) Hyperspectral imaging of nanoparticles in biological samples: Simultaneous visualization and elemental identification. *Microsc Res Tech*.

159. Doyon JB, *et al.* (2011) Rapid and efficient clathrin-mediated endocytosis revealed in genome-edited mammalian cells. *Nat Cell Biol* 13(3):331-337.

160. Han P, Wu C, & Xiao Y (2013) The effect of silicate ions on proliferation, osteogenic differentiation and cell signalling pathways (WNT and SHH) of bone marrow stromal cells. *Biomaterials Science* 1(4):379-392.

161. Reffitt D, *et al.* (2003) Orthosilicic acid stimulates collagen type 1 synthesis and osteoblastic differentiation in human osteoblast-like cells in vitro. *Bone* 32(2):127-135.

162. Yoshizawa S, Brown A, Barchowsky A, & Sfeir C (2014) Role of magnesium ions on osteogenic response in bone marrow stromal cells. *Connective Tissue Research* 55(sup1):155-159.

163. Clement-Lacroix P, *et al.* (2005) Lrp5-independent activation of Wnt signaling by lithium chloride increases bone formation and bone mass in mice. *Proc Natl Acad Sci U S A* 102(48):17406-17411.

164. Zhang F, Phiel CJ, Spece L, Gurvich N, & Klein PS (2003) Inhibitory phosphorylation of glycogen synthase kinase-3 (GSK-3) in response to lithium. Evidence for autoregulation of GSK-3. *J Biol Chem* 278(35):33067-33077.

165. Nel AE, *et al.* (2009) Understanding biophysicochemical interactions at the nano-bio interface. *Nat Mater* 8(7):543-557.

166. Grzincic EM, Yang JA, Drnevich J, Falagan-Lotsch P, & Murphy CJ (2015) Global transcriptomic analysis of model human cell lines exposed to surface-modified gold nanoparticles: the effect of surface chemistry. *Nanoscale* 7(4):1349-1362.

167. Orecchioni M, *et al.* (2016) Molecular and Genomic Impact of Large and Small Lateral Dimension Graphene Oxide Sheets on Human Immune Cells from Healthy Donors. *Adv Healthc Mater* 5(2):276-287.

168. Huang da W, Sherman BT, & Lempicki RA (2009) Systematic and integrative analysis of large gene lists using DAVID bioinformatics resources. *Nat Protoc* 4(1):44-57.

169. Supek F, Bosnjak M, Skunca N, & Smuc T (2011) REVIGO summarizes and visualizes long lists of gene ontology terms. *PloS one* 6(7):e21800.

170. Shannon P, *et al.* (2003) Cytoscape: a software environment for integrated models of biomolecular interaction networks. *Genome Res* 13(11):2498-2504.

171. Albanese A, Tang PS, & Chan WC (2012) The effect of nanoparticle size, shape, and surface chemistry on biological systems. *Annu Rev Biomed Eng* 14:1-16.

172. Rauch J, Kolch W, Laurent S, & Mahmoudi M (2013) Big signals from small particles: regulation of cell signaling pathways by nanoparticles. *Chem Rev* 113(5):3391-3406.

173. Liu ZJ, Zhuge Y, & Velazquez OC (2009) Trafficking and Differentiation of Mesenchymal Stem Cells. *J Cell Biochem* 106(6):984-991.

174. Wennerberg K, Rossman KL, & Der CJ (2005) The Ras superfamily at a glance. *J Cell Sci* 118(5):843-846.

175. Hutchison M, Berman KS, & Cobb MH (1998) Isolation of TAO1, a protein kinase that activates MEKs in stress-activated protein kinase cascades. *J Biol Chem* 273(44):28625-28632.

176. Wang FS, *et al.* (2002) Superoxide mediates shock wave induction of ERK-dependent osteogenic transcription factor (CBFA1) and mesenchymal cell differentiation toward osteoprogenitors. *J Biol Chem* 277(13):10931-10937.

177. Cargnello M & Roux PP (2011) Activation and function of the MAPKs and their substrates, the MAPK-activated protein kinases. *Microbiol Mol Biol Rev* 75(1):50-83.

178. Song L, Webb NE, Song Y, & Tuan RS (2006) Identification and functional analysis of candidate genes regulating mesenchymal stem cell self-renewal and multipotency. *Stem Cells* 24(7):1707-1718.

179. Rawlings JS, Rosler KM, & Harrison DA (2004) The JAK/STAT signaling pathway. *J Cell Sci* 117(Pt 8):1281-1283.

180. Clevers H (2006) Wnt/β-Catenin Signaling in Development and Disease. *Cell* 127(3):469-480.

181. Cantley LC (2002) The Phosphoinositide 3-Kinase Pathway. *Science* 296(5573):1655-1657.

182. Hu X*, et al.* (2013) The role of ERK and JNK signaling in connective tissue growth factor induced extracellular matrix protein production and scar formation. *Arch Dermatol Res* 305(5):433-445.

183. Caro-Gonzalez HY*, et al.* (2012) Mitogen-activated protein kinase (MAPK/ERK) regulates adenomatous polyposis coli during growth-factor-induced cell extension. *J Cell Sci* 125(Pt 5):1247-1258.

184. Santos SD, Verveer PJ, & Bastiaens PI (2007) Growth factor-induced MAPK network topology shapes Erk response determining PC-12 cell fate. *Nat Cell Biol* 9(3):324-330.

185. Mansour SJ*, et al.* (1994) Transformation of mammalian cells by constitutively active MAP kinase kinase. *Science* 265(5174):966-970.

186. Yan L, Luo H, Gao X, Liu K, & Zhang Y (2012) Vascular endothelial growth factor-induced expression of its receptors and activation of the MAPK signaling pathway during ovine oocyte maturation in vitro. *Theriogenology* 78(6):1350-1360.

187. Costa PM & Fadeel B (2015) Emerging Systems Biology Approaches in Nanotoxicology: Towards a Mechanism-Based Understanding of Nanomaterial Hazard and Risk. *Toxicol Appl Pharmacol*.

188. Autefage H, *et al.* (2015) Sparse feature selection methods identify unexpected global cellular response to strontium-containing materials. *Proc Natl Acad Sci U S A* 112(14):4280-4285.

189. Smith BD & Grande DA (2015) The current state of scaffolds for musculoskeletal regenerative applications. *Nature Reviews Rheumatology* 11:213.

190. Place ES, Evans ND, & Stevens MM (2009) Complexity in biomaterials for tissue engineering. *Nature Materials* 8:457.

191. Wang Z, *et al.* (2017) Novel biomaterial strategies for controlled growth factor delivery for biomedical applications. *Npg Asia Materials* 9:e435.

192. Sprugel KH, McPherson JM, Clowes AW, & Ross R (1987) Effects of growth factors in vivo. I. Cell ingrowth into porous subcutaneous chambers. *The American Journal of Pathology* 129(3):601-613.

193. Carragee E, *et al.* (2013) Cancer risk after use of recombinant bone morphogenetic protein-2 for spinal arthrodesis. *Journal of Bone & Joint Surgery - American Volume* 95(17):1537-1545.

194. Carragee EJ, Hurwitz EL, & Weiner BK (2011) A critical review of recombinant human bone morphogenetic protein-2 trials in spinal surgery: emerging safety concerns and lessons learned. *The Spine Journal* 11(6):471-491.

195. Ong KL, *et al.* (2010) Off-label use of bone morphogenetic proteins in the United States using administrative data. *Spine* 35(19):1794-1800.

196. Lad SP, Nathan JK, & Boakye M (2011) Trends in the use of bone morphogenetic protein as a substitute to autologous iliac crest bone grafting for spinal fusion procedures in the United States. *Spine* 36(4):E274-281.

197. Hoppe A, Güldal NS, & Boccaccini AR (2011) A review of the biological response to ionic dissolution products from bioactive glasses and glass-ceramics. *Biomaterials* 32(11):2757-2774.

198. Paul A, *et al.* (2016) Nanoengineered biomimetic hydrogels for guiding human stem cell osteogenesis in three dimensional microenvironments. *Journal of Materials Chemistry B* 4(20):3544-3554.

199. Mousa M, Evans ND, Oreffo ROC, & Dawson JI (2018) Clay nanoparticles for regenerative medicine and biomaterial design: A review of clay bioactivity. *Biomaterials* 159:204-214.

200. Gaharwar AK, *et al.* (2013) Bioactive silicate nanoplatelets for osteogenic differentiation of human mesenchymal stem cells. *Adv. Mater.* 25(24):3329-3336.

201. Carrow JK, *et al.* (2018) Widespread changes in transcriptome profile of human mesenchymal stem cells induced by two-dimensional nanosilicates. *Proceedings of the National Academy of Sciences* 115(17):E3905-E3913.

202. Jatav S & Joshi YM (2014) Chemical stability of Laponite in aqueous media. *Applied Clay Science* 97–98:72-77.

203. Rattanawarawipa P, Pavasant P, Osathanon T, & Sukarawan W (2016) Effect of lithium chloride on cell proliferation and osteogenic differentiation in stem cells from human exfoliated deciduous teeth. *Tissue and Cell* 48(5):425-431.

204. Zreiqat H, *et al.* (2002) Mechanisms of magnesium-stimulated adhesion of osteoblastic cells to commonly used orthopaedic implants. *Journal of biomedical materials research* 62(2):175-184.

205. Damsky CH (1999) Extracellular matrix–integrin interactions in osteoblast function and tissue remodeling. *Bone* 25(1):95-96.

206. Marie PJ (2009) Bone cell–matrix protein interactions. *Osteoporosis International* 20(6):1037-1042.

207. Lanza R & Atala A (2013) *Essentials of Stem Cell Biology* (Elsevier Science).

208. Ronga M, *et al.* (2013) Clinical applications of growth factors in bone injuries: Experience with BMPs. *Injury* 44, Supplement 1:S34-S39.

209. Administration. FUSFaD (2002) InFUSE™ Bone Graft/LT-CAGE™ Lumbar Tapered Fusion Device.

210. Zhang Q, *et al.* (2012) Improvement in the delivery system of bone morphogenetic protein-2: a new approach to promote bone formation. *Biomedical materials (Bristol, England)* 7(4):045002.

211. Lee K, Silva EA, & Mooney DJ (2011) Growth factor delivery-based tissue engineering: general approaches and a review of recent developments. *J R Soc Interface* 8(55):153-170.

212. Prolo DJ & Rodrigo JJ (1985) Contemporary bone graft physiology and surgery. *Clinical orthopaedics and related research* 200(200):322-342.

213. Rios DL, Lopez C, Alvarez ME, Samudio IJ, & Carmona JU (2015) Effects over time of two platelet gel supernatants on growth factor, cytokine and hyaluronan concentrations in normal synovial membrane explants challenged with lipopolysaccharide. *BMC musculoskeletal disorders* 16:153.

214. Ong KL*, et al.* (2010) Off-label use of bone morphogenetic proteins in the United States using administrative data. *Spine* 35(19):1794-1800.

215. Carragee EJ, Hurwitz EL, & Weiner BK (2011) A critical review of recombinant human bone morphogenetic protein-2 trials in spinal surgery: emerging safety concerns and lessons learned. *Spine J* 11(6):471-491.

216. Lad SP, Nathan JK, & Boakye M (2011) Trends in the use of bone morphogenetic protein as a substitute to autologous iliac crest bone grafting for spinal fusion procedures in the United States. *Spine* 36(4):E274-E281.

217. Shields LB*, et al.* (2006) Adverse effects associated with high-dose recombinant human bone morphogenetic protein-2 use in anterior cervical spine fusion. *Spine* 31(5):542-547.

218. Winn SR, Uludag H, & Hollinger JO (1998) Sustained release emphasizing recombinant human bone morphogenetic protein-2. *Advanced drug delivery reviews* 31(3):303-318.

219. Quinlan E, Thompson EM, Matsiko A, O'Brien FJ, & Lopez-Noriega A (2015) Long-term controlled delivery of rhBMP-2 from collagen-hydroxyapatite scaffolds for superior bone tissue regeneration. *J Control Release* 207:112-119.

220. Samorezov JE, Headley EB, Everett CR, & Alsberg E (2016) Sustained presentation of BMP-2 enhances osteogenic differentiation of human adipose-derived stem cells in gelatin hydrogels. *Journal of biomedical materials research. Part A* 104(6):1387-1397.

221. Seo BB, Choi H, Koh JT, & Song SC (2015) Sustained BMP-2 delivery and injectable bone regeneration using thermosensitive polymeric nanoparticle hydrogel bearing dual interactions with BMP-2. *J Control Release* 209(Supplement C):67-76.

222. Bastami F*, et al.* (2017) Fabrication of a three-dimensional beta-tricalcium-phosphate/gelatin containing chitosan-based nanoparticles for sustained release of bone morphogenetic protein-2: Implication for bone tissue engineering. *Materials science & engineering. C, Materials for biological applications* 72:481-491.

223. Fraile JM*, et al.* (2016) Laponite as carrier for controlled in vitro delivery of dexamethasone in vitreous humor models. *Eur J Pharm Biopharm* 108:83-90.

224. Mousa M, Evans ND, Oreffo RO, & Dawson JI (2018) Clay nanoparticles for regenerative medicine and biomaterial design: a review of clay bioactivity. *Biomaterials*.

225. Henkel J*, et al.* (2013) Bone Regeneration Based on Tissue Engineering Conceptions — A 21st Century Perspective. *Bone Research* 1:216.

226. Ruzicka B & Zaccarelli E (2011) A fresh look at the Laponite phase diagram. *Soft Matter* 7(4):1268-1286.

227. Peak CW, Stein J, Gold KA, & Gaharwar AK (2018) Nanoengineered Colloidal Inks for 3D Bioprinting. *Langmuir* 34(3):917-925.

228. Wang S*, et al.* (2013) Laponite nanodisks as an efficient platform for Doxorubicin delivery to cancer cells. *Langmuir* 29(16):5030-5036.

229. Lokhande G, *et al.* (2018) Nanoengineered injectable hydrogels for wound healing application. *Acta biomaterialia*.

230. Li K, *et al.* (2014) Enhanced in vivo antitumor efficacy of doxorubicin encapsulated within laponite nanodisks. *ACS Appl Mater Interfaces* 6(15):12328-12334.

231. Wang S, *et al.* (2013) Laponite Nanodisks as an Efficient Platform for Doxorubicin Delivery to Cancer Cells. *Langmuir* 29(16):5030-5036.

232. Gibbs DM, *et al.* (2016) Bone induction at physiological doses of BMP through localization by clay nanoparticle gels. *Biomaterials* 99:16-23.

233. Dawson JI, Kanczler JM, Yang XB, Attard GS, & Oreffo RO (2011) Clay gels for the delivery of regenerative microenvironments. *Adv Mater* 23(29):3304-3308.

234. Sikkink LA & Ramirez-Alvarado M (2008) Biochemical and aggregation analysis of Bence Jones proteins from different light chain diseases. *Amyloid* 15(1):29-39.

235. Skelton S, *et al.* (2013) Biomimetic adhesive containing nanocomposite hydrogel with enhanced materials properties. *Soft Matter* 9(14):3825-3833.

236. Ghadiri M, Hau H, Chrzanowski W, Agus H, & Rohanizadeh R (2013) Laponite clay as a carrier for in situ delivery of tetracycline. *RSC Advances* 3(43):20193-20201.

237. Fleischer CC & Payne CK (2014) Nanoparticle-cell interactions: molecular structure of the protein corona and cellular outcomes. *Accounts of chemical research* 47(8):2651-2659.

238. Lynch I & Dawson KA (2008) Protein-nanoparticle interactions. *Nano Today* 3(1–2):40-47.

239. Saikia J, Yazdimamaghani M, Hadipour Moghaddam SP, & Ghandehari H (2016) Differential Protein Adsorption and Cellular Uptake of Silica Nanoparticles Based on Size and Porosity. *ACS Appl Mater Interfaces* 8(50):34820-34832.

240. Takahashi T, Yamada Y, Kataoka K, & Nagasaki Y (2005) Preparation of a novel PEG-clay hybrid as a DDS material: dispersion stability and sustained release profiles. *J Control Release* 107(3):408-416.

241. Hawe A, Sutter M, & Jiskoot W (2008) Extrinsic fluorescent dyes as tools for protein characterization. *Pharm Res-Dordr* 25(7):1487-1499.

242. Stryer L (1965) The interaction of a naphthalene dye with apomyoglobin and apohemoglobin. A fluorescent probe of non-polar binding sites. *J Mol Biol* 13(2):482-495.

243. Hauschka PV, Lian JB, Cole DE, & Gundberg CM (1989) Osteocalcin and matrix Gla protein: vitamin K-dependent proteins in bone. *Physiol Rev* 69(3):990-1047.

244. Denhardt DT & Noda M (1998) Osteopontin expression and function: role in bone remodeling. *J Cell Biochem Suppl* 30-31:92-102.

245. Chimene D*, et al.* (2018) Nanoengineered Ionic–Covalent Entanglement (NICE) Bioinks for 3D Bioprinting. *ACS Applied Materials & Interfaces* 10(12):9957-9968.

246. Cross LM, Shah K, Palani S, Peak CW, & Gaharwar AK (2017) Gradient nanocomposite hydrogels for interface tissue engineering. *Nanomedicine*.

247. Hoemann CD, Lafantaisie-Favreau CH, Lascau-Coman V, Chen G, & Guzman-Morales J (2012) The cartilage-bone interface. *The journal of knee surgery* 25(2):85-97.

248. Nukavarapu SP & Dorcemus DL (2013) Osteochondral tissue engineering: Current strategies and challenges. *Biotechnology Advances* 31(5):706-721.

249. Cross LM, Thakur A, Jalili NA, Detamore M, & Gaharwar AK (2016) Nanoengineered biomaterials for repair and regeneration of orthopedic tissue interfaces. *Acta Biomater* 42:2-17.

250. Thakur A, *et al.* (2016) Injectable shear-thinning nanoengineered hydrogels for stem cell delivery. *Nanoscale* 8(24):12362-12372.

251. Mihaila SM*, et al.* (2013) Photocrosslinkable kappa-carrageenan hydrogels for tissue engineering applications. *Adv Healthc Mater* 2(6):895-907.

252. Gaharwar AK, Rivera CP, Wu C-J, & Schmidt G (2011) Transparent, elastomeric and tough hydrogels from poly(ethylene glycol) and silicate nanoparticles. *Acta Biomaterialia* 7(12):4139-4148.

253. Peak CW, Carrow JK, Thakur A, Singh A, & Gaharwar AK (2015) Elastomeric Cell-Laden Nanocomposite Microfibers for Engineering Complex Tissues. *Cell Mol Bioeng* 8(3):404-415.

254. Gaharwar AK*, et al.* (2014) Shear-Thinning Nanocomposite Hydrogels for the Treatment of Hemorrhage. *ACS Nano* 8(10):9833-9842.

255. Lu HH & Thomopoulos S (2013) Functional Attachment of Soft Tissues to Bone: Development, Healing, and Tissue Engineering. *Annual review of biomedical engineering* 15:201-226.

256. Slaughter BV, Khurshid SS, Fisher OZ, Khademhosseini A, & Peppas NA (2009) Hydrogels in Regenerative Medicine. *Advanced Materials* 21(32-33):3307-3329.

257. Hancock MJ, He JK, Mano JF, & Khademhosseini A (2011) Surface-Tension-Driven Gradient Generation in a Fluid Stripe for Bench-Top and Microwell Applications. *Small* 7(7):892-901.

258. Piraino F, Camci-Unal G, Hancock MJ, Rasponi M, & Khademhosseini A (2012) Multi-gradient hydrogels produced layer by layer with capillary flow and crosslinking in open microchannels. *Lab on a Chip* 12(3):659-661.

259. Tang G*, et al.* (2012) Preparation of PLGA scaffolds with graded pores by using a gelatin-microsphere template as porogen. *Journal of biomaterials science. Polymer edition* 23(17):2241-2257.

260. Mohan N*, et al.* (2011) Continuous gradients of material composition and growth factors for effective regeneration of the osteochondral interface. *Tissue engineering. Part A* 17(21-22):2845-2855.

261. Pedron S, Peinado C, Bosch P, Benton JA, & Anseth KS (2011) Microfluidic approaches for the fabrication of gradient crosslinked networks based on poly(ethylene glycol) and hyperbranched polymers for manipulation of cell interactions. *Journal of Biomedical Materials Research Part A* 96A(1):196-203.

262. Mahadik BP, Wheeler TD, Skertich LJ, Kenis PJA, & Harley BAC (2014) Microfluidic Generation of Gradient Hydrogels to Modulate Hematopoietic Stem Cell Culture Environment. *Advanced Healthcare Materials* 3(3):449-458.

263. Campo VL, Kawano DF, Silva Jr DBd, & Carvalho I (2009) Carrageenans: Biological properties, chemical modifications and structural analysis – A review. *Carbohydrate Polymers* 77(2):167-180.

264. Nichol JW*, et al.* (2010) Cell-laden microengineered gelatin methacrylate hydrogels. *Biomaterials* 31(21):5536-5544.

265. Fang Y, Li L, Inoue C, Lundin L, & Appelqvist I (2006) Associative and Segregative Phase Separations of Gelatin/κ-Carrageenan Aqueous Mixtures. *Langmuir* 22(23):9532-9537.

266. Pawar N & Bohidar HB (2009) Surface selective binding of nanoclay particles to polyampholyte protein chains. *The Journal of Chemical Physics* 131(4):045103.

267. Fuß M, Ehlers EM, Russlies M, Rohwedel J, & Behrens P (2000) Characteristics of human chondrocytes, osteoblasts and fibroblasts seeded onto a type I/III collagen sponge under different culture conditions. *Annals of Anatomy - Anatomischer Anzeiger* 182(4):303-310.

268. Antonov YA & Gonçalves MP (1999) Phase separation in aqueous gelatin–κ-carrageenan systems. *Food Hydrocolloids* 13(6):517-524.

269. Annabi N, *et al.* (2010) Controlling the Porosity and Microarchitecture of Hydrogels for Tissue Engineering. *Tissue Engineering Part B: Reviews* 16(4):371-383.

270. Kim HJ, Kim UJ, Vunjak-Novakovic G, Min BH, & Kaplan DL (2005) Influence of macroporous protein scaffolds on bone tissue engineering from bone marrow stem cells. *Biomaterials* 26(21):4442-4452.

271. Whang K, *et al.* (1999) Engineering bone regeneration with bioabsorbable scaffolds with novel microarchitecture. *Tissue Engineering* 5(1):35-51.

272. Lien S-M, Ko L-Y, & Huang T-J (2009) Effect of pore size on ECM secretion and cell growth in gelatin scaffold for articular cartilage tissue engineering. *Acta Biomaterialia* 5(2):670-679.

273. Subramony S, *et al.* (2013) The guidance of stem cell differentiation by substrate alignment and mechanical stimulation. *Biomaterials* 34(8):1942-1953.

274. Tse JR & Engler AJ (2011) Stiffness Gradients Mimicking In Vivo Tissue Variation Regulate Mesenchymal Stem Cell Fate. *PloS one* 6(1):e15978.

275. Hasin Y, Seldin M, & Lusis A (2017) Multi-omics approaches to disease. *Genome Biology* 18:83.

276. Karczewski KJ & Snyder MP (2018) Integrative omics for health and disease. *Nature Reviews Genetics* 19:299.

277. Rogers S*, et al.* (2008) Investigating the correspondence between transcriptomic and proteomic expression profiles using coupled cluster models. *Bioinformatics* 24(24):2894-2900.

278. Hollywood K, Brison DR, & Goodacre R (2006) Metabolomics: current technologies and future trends. *Proteomics* 6(17):4716-4723.

279. Gérard C, Bordeleau L-J, Barralet J, & Doillon CJ (2010) The stimulation of angiogenesis and collagen deposition by copper. *Biomaterials* 31(5):824-831.

280. Zhai W*, et al.* (2012) Silicate bioceramics induce angiogenesis during bone regeneration. *Acta Biomaterialia* 8(1):341-349.

281. Yoshizawa S, Brown A, Barchowsky A, & Sfeir C (2014) Magnesium ion stimulation of bone marrow stromal cells enhances osteogenic activity, simulating the effect of magnesium alloy degradation. *Acta Biomaterialia* 10(6):2834-2842.

APPENDIX A

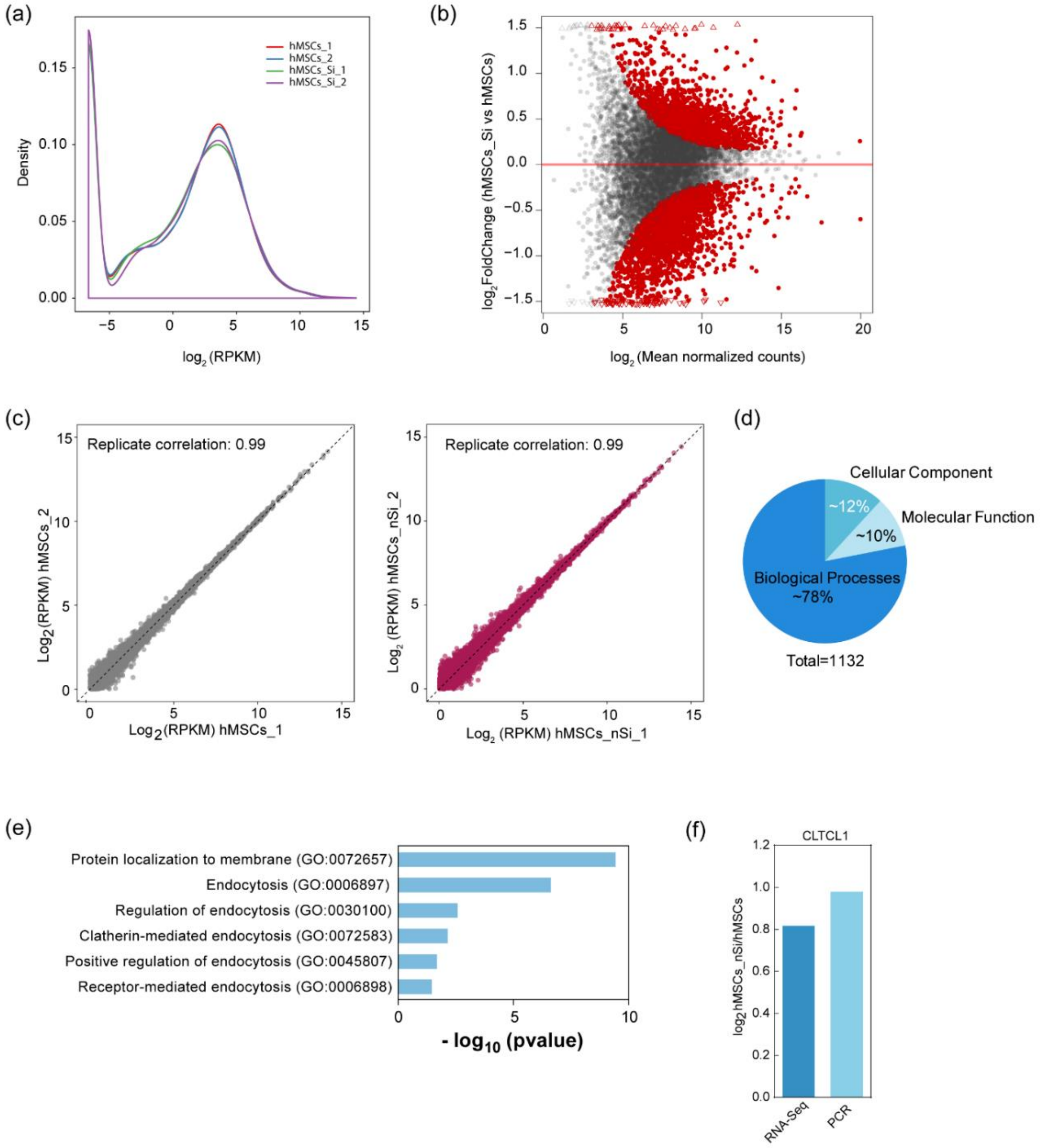

Figure A-1 RNA-seq data analysis. (A) Distribution of log2(RPKM + 0.01) of all genes. (B) MA plot (Bland-Altman plat) for all genes that are tested by the RPKM > 1 cutoff. (C) Replicate variation of RNA-Seq samples. Correlation for replicates among untreated and treated populations, respectively, indicate high degrees of reliability and consistency between tested samples. (D) Broad grouping of GO terms into three main groups: biological processes, cellular component, and molecular function. (E) GO terms specific to endocytosis process. (F) PCR validation of RNA-seq specific to gene controlling clathrin machinery [clathrin heavy chain like 1 (*CLTCL1*)].

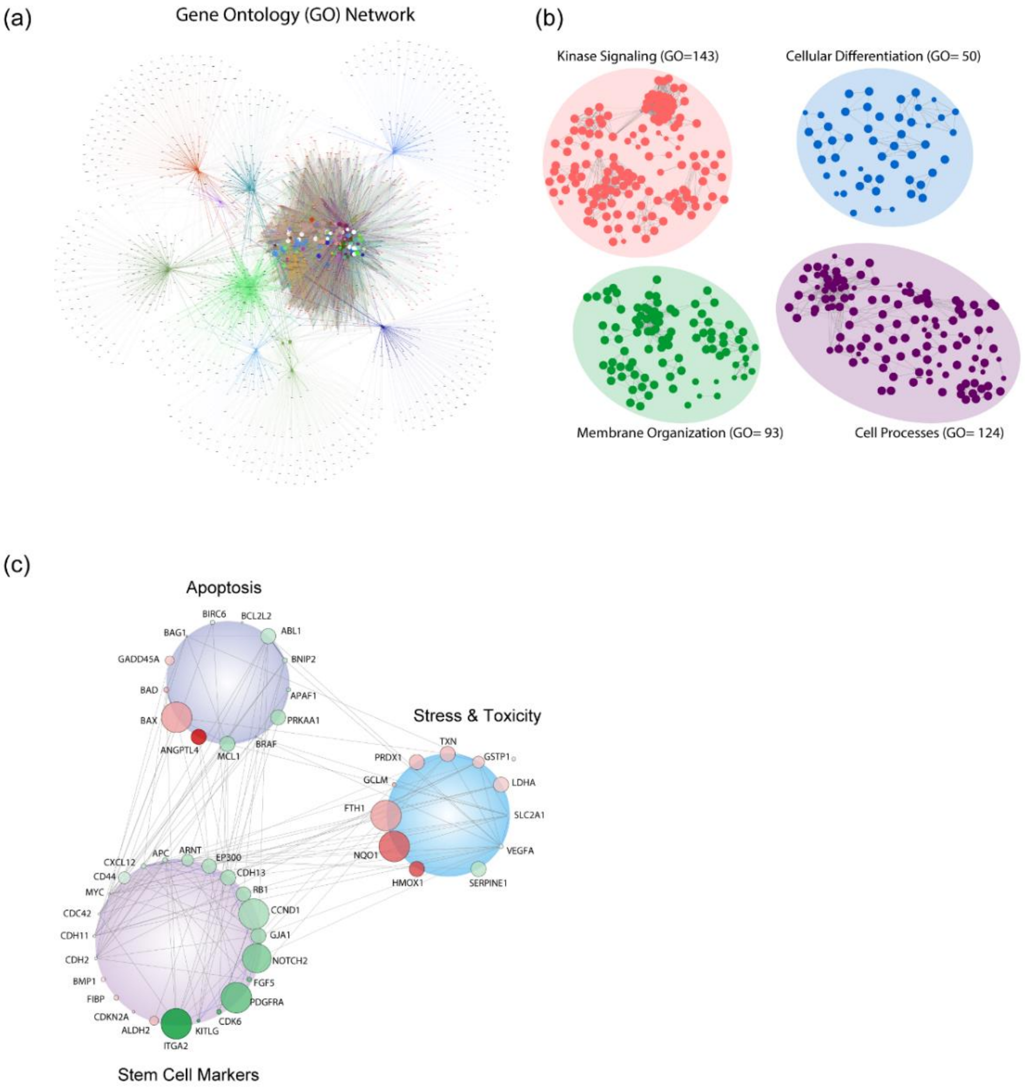

Figure A-2 (A) Network of GO terms and expressed gene clusters around each respective correlating term illustrating highly interconnected stimulation with nanosilicates. (B) GO terms could be subsequently divided into four primary cellular systems including basic processes, membrane organization, kinase signaling, and differentiation responses. (C) Gene network displaying interconnected genetic targets after nanosilicate treatment with high degrees of expression and statistical significance (red, up-regulated; green, down-regulated; size increases with significance).

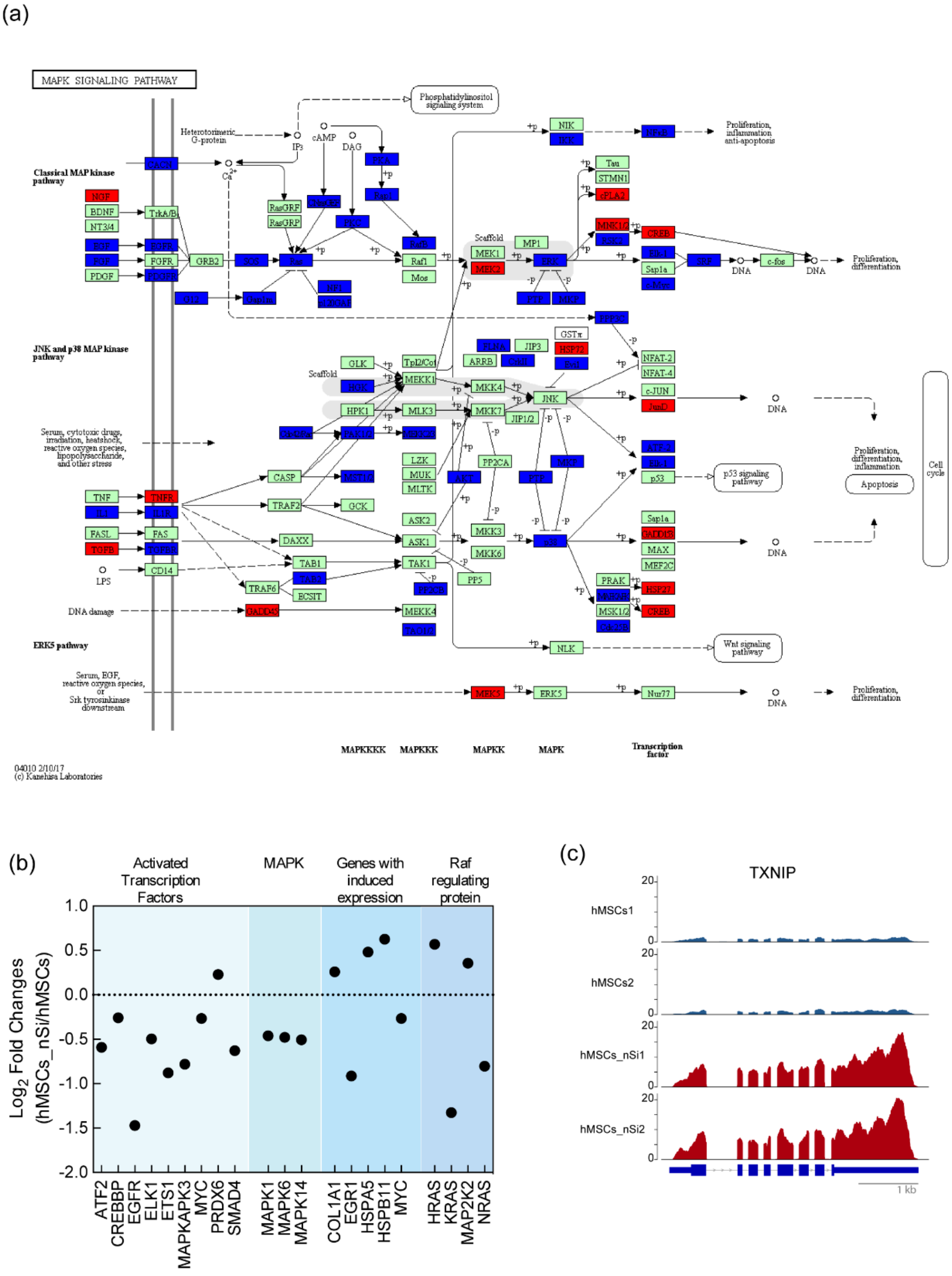

Figure A-3 (A) Kegg pathway specific to MAPK signaling with differentially expressed genes form RNA-seq (red, up-regulated; blue, down-regulated). (B) Organization of gene expression throughout MAPK signaling pathways. (C) Expression tracks of *TXNIP* in hMSCs and nanosilicate-treated hMSCs.

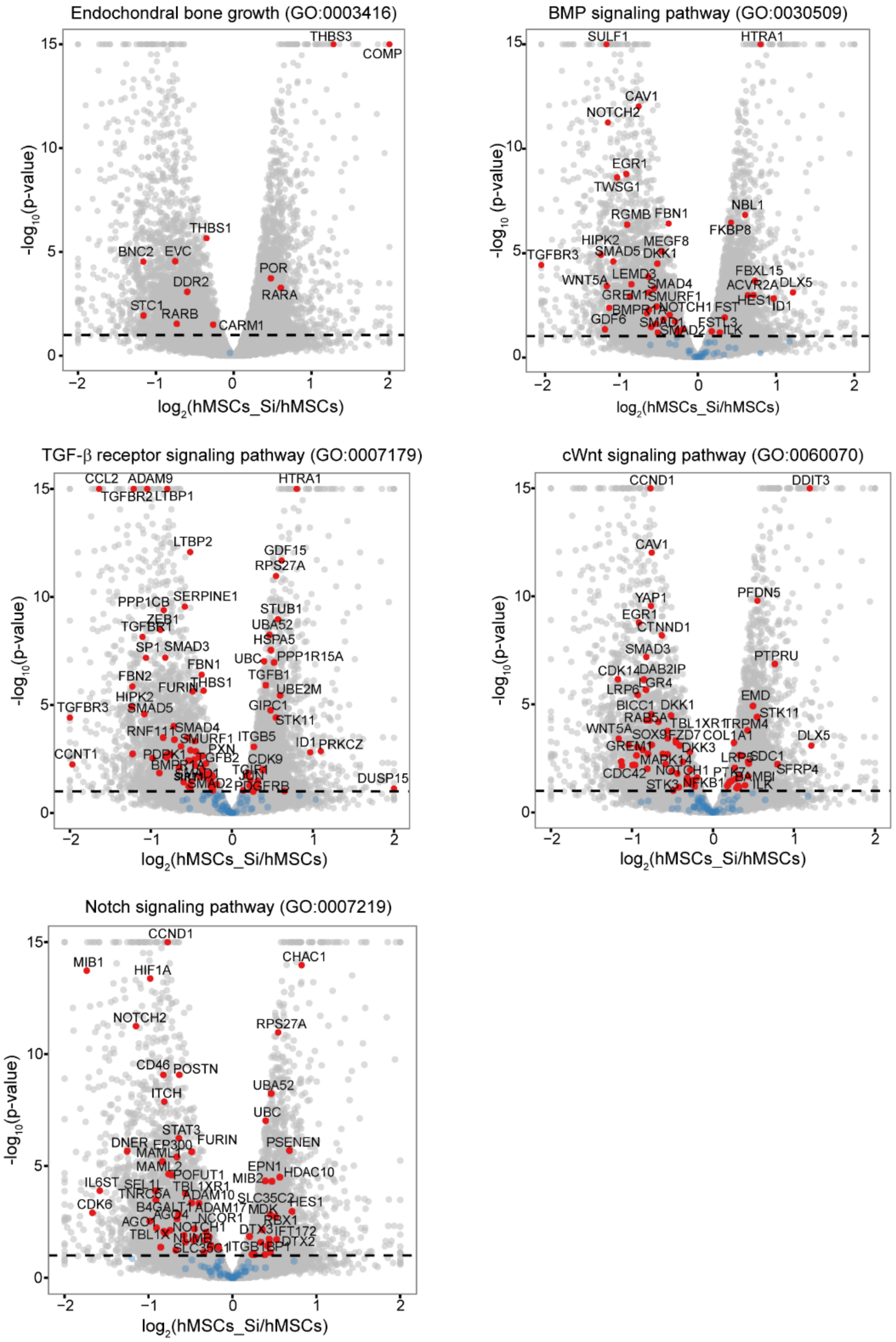

Figure A-4 Volcano plots showing key genes differentially regulated for key GO terms.

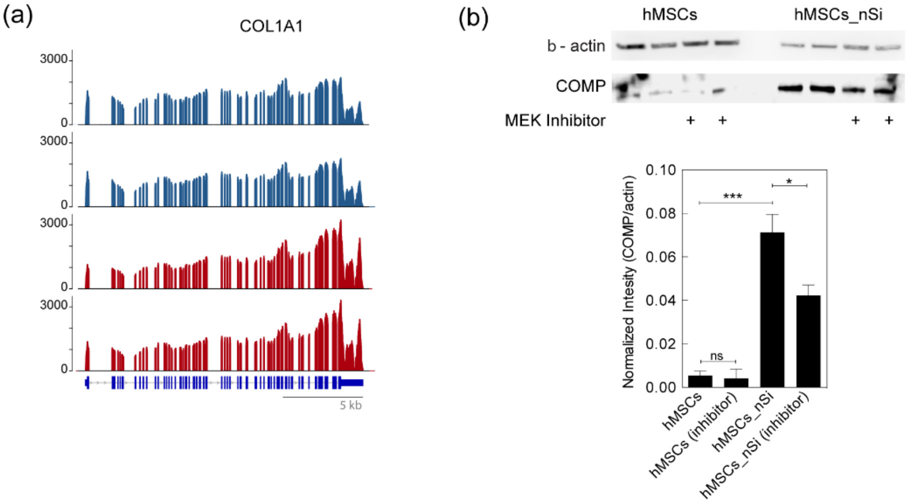

Figure A-5 (A) Expression tracks for collagen type I (*COL1A1*) for control (blue) and treated (red) populations. (B) Western blot for differentiation-specific proteins, COMP, for control and nanosilicate-treated samples. Addition of MEK inhibitor reduced protein synthesis of both targets. $*P < 0.05$; $***P < 0.001$. ns, not significant.